Mechanics of crypt folding, tissue compartmentalization and collective cell migration in intestinal organoids

Gerardo Ceada Torres

Aquesta tesi doctoral està subjecta a la llicència ***Reconeixement- NoComercial – SenseObraDerivada 4.0. Espanya de Creative Commons.***

Esta tesis doctoral está sujeta a la licencia ***Reconocimiento - NoComercial – SinObraDerivada 4.0. España de Creative Commons.***

This doctoral thesis is licensed under the ***Creative Commons Attribution-NonCommercial-NoDerivs 4.0. Spain License.***

UNIVERSITAT DE BARCELONA

IBEC
Institute for Bioengineering of Catalonia

Mechanics of crypt folding, tissue compartmentalization and collective cell migration in intestinal organoids

Memòria per optar al grau de Doctor en el
Programa de Doctorat en Biomedicina de la
Universitat de Barcelona

Presentada per:

Gerardo Ceada Torres

Dirigida per:

Dr. Xavier Trepat Guixer

Dr. Carlos Pérez González

A mis abuelas y abuelos

La ciencia nos enseña, en efecto, a someter nuestra razón a la verdad y a conocer y juzgar las cosas tal como son, es decir, como ellas mismas eligen ser y no como quisiéramos que fueran.

Miguel de Unamuno

Acknowledgements

Parece mentira que hayan pasado ya 5 años desde que llegué al laboratorio y que me vea escribiendo estas palabras… Cruzo los dedos por no dejarme a nadie atrás entre estas líneas, y si es así, os pido perdón por adelantado. Todos aquellos que me habéis rodeado sabéis lo mucho que os aprecio y esta tesis no habría sido posible sin vosotros.

Me gustaría comenzar agradeciendo a mis dos directores de tesis, Xavi y Carlos, por el papel crucial que han tenido en este viaje. Xavi, encara recordo arribar al teu laboratori per primera vegada just en acabar el grau. Jo em creia ja tot un científic (que ingenu), però quan em vas començar a ensenyar dades que si de pollastres, que si de peixos, que si d'organoides… em vaig adonar de tot el que em quedava encara per aprendre. En aquell moment vas apostar per mi, i te n'estaré sempre agraït. Admiro la teva capacitat per connectar idees i mirar les coses amb diferents ulls, espero haver-ne après ni que sigui una mica. T'agraeixo també que hagis sabut posar-me de la mà de la millor persona de la qual aprendre, en Carlos. Carlos, te agradezco haber sido mi referente tanto en lo profesional como en lo personal. Me has dado unas lecciones de vida brutales y creo que no sólo a mí, sino a todo el que te conoce. Gracias por transmitirme tu pasión por la ciencia con la alegría y paz que desprendes. Recordaré con cariño aquellas noches de microscopio, las risas en cultivos y las llamadas para un ratito que se acaban convirtiendo en horas (estas espero que sigan siendo así). Para mí ha sido todo un placer trabajar contigo, me lo he pasado genial y he aprendido riendo. Estoy seguro de que crearás toda una escuela de pensamiento y saber hacer, y no sabes cuánto me alegra haber sido su primer fruto.

I would also like to thank my thesis follow-up committee Pere Roca-Cusachs and Danijela Matic Vignjevic for their insightful comments and feedback throughout the project. I enjoyed a lot discussing with both of you and, for sure, this thesis is much better thanks to you. I am also very thankful to Elena Martínez, Jordi Guiu, Zev Gartner, Jordi Comelles and Alejandro Torres for taking the time to read and evaluate this thesis.

Enormous thanks to the rest of the “Organoiders” Team. Manu, mil gracias por tu trabajo con las tracciones, y por estar siempre dispuesto a enseñarme con tanto cariño. Eres, sin duda, uno de los pilares fundamentales del lab. Marija, thank you so much for all the work you have done on the segmentation and for all the feedback that you give in all the meetings. I don’t know how you do it, but you are always on point. Clément, merci beaucoup pour tout ce que tu as fait pendant ces mois, on a avancé beaucoup ensemble et je suis très heureux que tu continues avec le projet. Je suis sûr que tu iras bien loin. Meng, thank you for being always there to help us anytime we have needed it, I appreciate it a lot.

Thank you so much Francesco, Sohan and Marino for all the work you have done on the vertex model and the monolayer stress microscopy. Also, many thanks to Venkata, Denis, Andrew and Jorge and the rest of the Vignjevic’s lab for helping us during the reviews.

Muchas gracias al cuerpo técnico pasado y presente del laboratorio – Natalia, Oriol, Anghara, Susana, Mònica. Especialmente me gustaría agradecer a Natalia y a Anghara por todo la ayuda que nos han ofrecido durante el proyecto. Natalia, eres un terremoto y tienes una valía impresionante. Me alegra verte feliz y estoy seguro de que conseguirás siempre lo que te propongas. Anghara, mil gracias por tu implicación constante. Eres una persona genial y una tremenda profesional. Me da la risa cada vez que recuerdo las caras de esfuerzo que se nos ponía al agitar los tejidos. Fuiste uno de mis mejores apoyos en los momentos de mayor estrés. Gracias por transmitirme siempre tu optimismo. Gracias también a Susana, por toda la ayuda que nos has dado, siempre con una sonrisa. Te lo agradezco de todo corazón. De verdad, gracias por todo, por ser compañeras y amigas.

Ignasi, crec que en l’única cosa on estarem d’acord és que ens ho passem molt bé estant en desacord. Gràcies per estar sempre disposat a ajudar amb el que sigui i per seguir les meves absurditats, m’ho passo sempre genial al teu costat. Espero i n’estic segur que seguirem tenint aquestes converses acalorades sobre qualsevol tema.

Marc, juntos, cual zipi y zape hemos llegado hasta aquí, y no sabes cuánto me alegro de que lo hayamos conseguido. Gracias por todos los momentos que hemos compartido dentro y fuera del laboratorio. Me fascina tu capacidad de afrontar los problemas y me alegra verte tan motivado, te lo mereces.

Juanfra, molas una “jartá”. Irradias alegría y créeme que nos hace muy feliz tenerte a nuestro lado. Tu resiliencia es digna de admirar. Me alegro de que hayas podido parir por fin el artículo y de que puedas volver a tu circadianidad tan deseada.

Miguel, ¡eres pura cosecha propia! Gracias por encajar mis bromas con tanta paciencia. Sacarte una sonrisa me alegra el día. Por cierto, no sé si te lo había dicho, pero qué cascos más guapos.

Ona, tens un caràcter i una personalitat que ja en voldrien molts. Aina, tens un do especial per explicar, fas que el difícil sembli superfàcil. Gràcies a les dos per tots els riures a la pecera, sou unes companyes genials.

Alice, it has been a pleasure to share this time with you. We had so much fun. Who is going to scare you now in the microscope? I should find someone who does it for me.

Sefora, ya no te cuelo ni una (o sí ¿?). Thank you for being always so smiley, I always get happy when encountering you.

Thomas, thanks for helping always with English wording and for taking - without cancelling - all my jokes, I enjoyed a lot having you in la pecera.

Leone, you know about everything, and you are a master of languages! Thanks for teaching me the few things I can say in Italian and for all the discussions we had.

Nimesh, thanks for being the master of ceremonies in all the events. Also, thanks for your contagious and joyful laugh, it is impossible to hear it and not to smile.

Isabela, thanks for all the discussions, about anything, anytime. We had so much fun with our “salseos and bombazos”. I am sure that you have a bright future ahead, you deserve it.

Zarina, thanks for being always so nice with me and with everyone. You are so strong.

Miquel, gràcies per organitzar totes les sortides de senderisme i els bons esmorzars a la bodega Montferry. Ens has fet descobrir molts de llocs i experiències noves.

Eleni, thank you for your Greek lessons and for all the scientific and non-scientific discussions. You have always been so helpful with me and everybody in the lab. The lab is a better place with you.

Víctor, gracias por seguir siempre apuntándote a todo, me lo paso genial contigo. Me encanta tu franqueza.

Ariadna, fuiste de las primeras personas que conocí al llegar al lab. Tienes una gran personalidad y has sido una compañera genial. Me alegro de que hayas encontrado tu vocación y de que lo estés disfrutando.

Macià, gràcies per les teves cançons al microscopi 3, som tots els teus groupies. Gràcies també per les discussions que ens hem marcat a cultius.

Xarxa, muchas gracias por ser tan buena compañera. Seguro que tus alumnos se lo pasarán super bien contigo, como lo hemos hecho nosotros.

Laura, merci pour tous tes commentaires et pour me faire pratiquer mon français.

Thanks to all the people from Trepat’s and Roca-Cusachs labs, it has been such an amazing experience for me and this is because of you. Thanks for all the feedback that you provided and for the good environment that you all create, it has been a pleasure to share these years with you. Thanks to all of you, Amy, Jenny, Ion, Ernest, Malèke, Raimon, Dobryna, Anabel-lise, Natxo, Mamatha, Sri, Tom, Jorge, Steffen, Pau, Özge, Guillermo, Irina, Kandela, Arnau, Benet, Eva, Cristina, Marina, Joan, kenta, Ali, Marilena, Aurora, Anna.

Thanks Clément, Eleni, Ona, Laura and Ignasi for reviewing the thesis and making so insightful comments.

També vull donar les gràcies a n'Arnau Rovira i en Guillermo Prado. Vaig gaudir i aprendre molt de l'experiència de tenir-vos com a estudiants de pràctiques. Gracias también Gonzalo Herranz por tu compañía durante tu estancia en el lab.

M'agradaria donar les gràcies a tota la gent del grup de càncer colorectal de l'IRB. Gràcies Carme per supervisar-me durant la meva estada al màster i per tota l'ajuda que sempre em dones, valoro moltíssim tot el que vaig aprendre de tu. Gràcies de tot cor, Sergio, per tota la feina que has fet amb els ratolins, has fet un esforç titànic. Gracias Marta por enseñarme a hacer immunos y por recibirme siempre con una sonrisa cuando vengo a pedir cosas. Gracias Xavi por sacar tiempo para enseñarme en el estabulario, aprendí muchísimo de ti y nos lo pasamos genial. Eres un profesor nato, te encanta lo que haces y así lo transmites. Gracias Adrián, por ayudarme con los organoides, eres un maestro del shacking. Gràcies Eduard, Elena, Adrià, Clara, Jelena, Maria, Felipe i tots els integrants del grup, per acollir-me sempre amb els braços oberts, sou genials.

Thanks to la Caixa foundation for supporting me with a fellowship. Also, thanks to Marina, Alejandra, Ana S., Ana P., Arce, Fernando, Guille, Javi, Víctor R., Víctor B., Jose, Raúl, Gabriel, Diego, Marta and the rest of the fellows, I enjoyed so much the trainings and time out with you.

Gracias Aina, Marco, Andrés, Gaia, Marta, Albert, por las conversaciones y los ratos que hemos pasado.

Gracias también a todo el personal de core facilities, limpieza, recepción, y seguridad del PCB. Hacéis una labor muy importante y pocas veces reconocida.

I would also like to thank all the other supervisors that I had during my scientific career - Martín Villalba, Dang Vo, Marc Ribó, Jessica Castro, Michele de Palma, Chiara Cianciaruso, Tim Beltraminelli, Florent Duval and all the people from their labs. You all contributed to sculpt the scientist that I am know.

Gracias a mis amigos de Gibraleón. En especial a Pili, Alberto, Pablo H., Pablo B., Chema y Carlos, porque hacéis que por nosotros no pase el tiempo y que cada vez que nos encontremos parezca que nos hayamos despedido el día anterior.

Gracias a mi amiga Bea, la Greca, por tantos momentos vividos. Quién te iba a decir que sería tan difícil deshacerte de mí cuando nos encontramos por primera vez en el Erasmus, ¡eh!

Ricard, moltes gràcies per ser el meu germà català, em fa molt feliç que continuïs al meu costat.

Gracias a mis compis de piso, en especial a Joan y Álvaro por los momentos vividos durante la cuarentena, aquí podéis ver el resultado de esos días pegado al ordenador. También a David, que siempre se apunta a todo.

Gràcies a tots els amics de la UdG. En especial gràcies Nora, Dami, Carles, Sergi, Irene, Laia, María, Txell, Sergio, Marta, Pau, per tots els moments que hem passat. Les nostres quedades em fan desconnectar completament i em donen vida.

Gracias a todos los compañeros del máster, me alegra ver cómo cada uno ha ido encontrado su camino.

Gracias a mi familia, a todos, sin condición. Por haber sido siempre mis mayores fans y también los más críticos. No me da tiempo a avisar de que voy a bajar a casa que ya habéis organizado una barbacoa para que nos reunamos todos, no sabéis el bien que esto me hace.

Mamá, Papá, Lulu, lo malo no sé de dónde lo habré sacado, pero lo bueno estoy seguro de que viene de vosotros, sois los mejores. Gracias por apoyarme en todas mis decisiones, siempre y sin reproches. Abuela, me hace muchísima ilusión que vengas a la defensa de mi tesis, eres un ejemplo para todos nosotros y pagaría lo que fuera por la cara de felicidad que pondrás al leer esto.

A Marengo, Milo y Bruno, les agradezco su amor incondicional. Parece mentira que unas cosillas tan pequeñas puedan alegrarte tanto. Han sido, y son, mi mejor medicina para un día malo.

María, qué decirte, creo que estas líneas serán las que más me cuesten, pues ponga lo que ponga no hará juicio a todo lo que siento. Eres mi compañera favorita de batallas y aventuras y, sobre todo, eres casa. Gracias por disfrutar como la que más cuando he logrado algo y sacarme una sonrisa cuando las cosas no han ido tan bien. Gracias por soportarme día a día y por ser la víctima preferida de mis bromitas. Gracias por todos los momentos que hemos pasado (y los que están por venir) y por las lecciones que hemos aprendido juntos. Me alegra verte tan feliz con tu doctorado, eres una científica de 10 y te lo mereces. Aquí estaré siempre para apoyarte.

Preface

"Imagine that you knew everything about how a single fish works, all the biology, all the physics, everything. This, alone, will not let you predict how a school of a million fish will behave". Xavier Trepat postulated this idea in a conference - that I fortuitously watched – where he explained the concept of emergent phenomena and collective behaviors. I had never thought about such a fundamental problem, but I found it so interesting. This was how I came to know Trepat's work, and I consider this moment as the beginning of the journey that led to the thesis that you are now reading.

Some months later, I started working as a master student in Trepat's lab, under the supervision of Carlos Pérez - at the time a last year PhD student and now my thesis co-director. Carlos had already started doing some tests to culture intestinal organoids over hydrogels, to develop a system compatible with force measurements on the intestinal epithelium. From there, we continued working hand in hand in a project that composes a major part of this thesis and that we published as co-first authors in 2021[1]. In that project, we were able to quantitatively map the forces that intestinal organoids exert to fold into crypts and to allow migration from the crypt to the villus. After that, I started a new project, centered on the role of Eph/Ephrin signaling in the mechanics of crypt-villus compartmentalization. Overall, the work presented in this thesis involved extensive collaboration with colleagues from our lab and from the lab of Dr. Marino Arroyo, Dr. Danijela Matic Vignjevic and Dr. Eduard Batlle. The specific contributions of each collaborator to this project are listed at the end the thesis (section "Contributions to the data presented in this thesis").

This thesis focusses on the mechanics of three fundamental processes of the intestinal epithelium – crypt folding, tissue compartmentalization and collective cell migration. The thesis starts with an introduction, that can be divided in three parts. First, an introduction to general epithelial mechanics including how cells can generate, withstand, and sense mechanical forces as well as how these forces can orchestrate tissue folding and collective cell migration. Second, an introduction to the intestine, the intestinal epithelium and the intestinal organoid systems. Finally, an introduction to the current understanding of the mechanics of the intestinal epithelium.

Then, the aims and the methodology are presented, followed by the experimental results. These results include quantitative measurements of the forces that intestinal epithelial cells exert on the substrate and on their neighbors, and how these forces induce crypt folding, compartmentalize the tissue into crypt and villus domains and allow for constant flow of cells from crypt to villus.

The results are then discussed, by setting them in the context of existing literature and by generating new hypothesis. Finally, several conclusions are drawn from the presented data.

I hope you will enjoy reading it.

Funding

The project that gave rise to these results received the support of a fellowship from ”la Caixa” Foundation (ID 100010434). The fellowship code is LCF/BQ/DR19/11740013.

Table of contents

1 Introduction 1
  1.1 Epithelial mechanics 3
    1.1.1 The cellular machinery that exerts, withstands and senses mechanical forces 4
    1.1.2 Mechanosensing and mechanotransduction 9
    1.1.3 Epithelial forces and tissue folding 11
    1.1.4 Epithelial forces and collective cell migration 16
  1.2 The intestinal epithelium and its experimental models 19
    1.2.1 Anatomy of the mammalian intestine 19
    1.2.2 The intestinal epithelium: cell types and dynamics 21
    1.2.3 Intestinal organoids 25
  1.3 Mechanobiology of the intestinal epithelium 31
    1.3.1 Intestinal morphogenesis 31
    1.3.2 Proliferation and cell fate 41
    1.3.3 Migration along the crypt-villus axis 44
    1.3.4 Cell extrusion 45
2 Aims 49
  2.1 General aim 51
  2.2 Specific aims 51
3 Materials and methods 53
  3.1 Mice 55
  3.2 Intestinal organoid culture 55
  3.3 Polyacrylamide gel fabrication 58
  3.4 Polyacrylamide gel functionalization and ECM micropatterning 58
  3.5 Organoid seeding on PAA substrates 59
  3.6 Immunostaining 60
  3.7 Antibodies 62
  3.8 Image acquisition 63
  3.9 Three-dimensional traction microscopy 64
  3.10 Cell velocities 64
  3.11 Radial averaging and kymographs 65
  3.12 Averaging of crypt radial profiles 65
  3.13 Blebbistatin treatment 66
  3.14 F-actin and myosin quantification 66

3.15 EphB2 receptor quantification 67
3.16 Quantification of cell tilt *in vivo* 67
3.17 De novo crypt formation 68
3.18 Quantification of the area of the stem cell niche, and number of stem and Paneth cells 69
3.19 Laser cuts 70
3.20 Single-cell shape analysis 70
3.21 Quantification of the cell division rate 72
3.22 Quantification of Paneth cell clustering and density 72
3.23 Quantification of Ki67 area 73
3.24 Statistics and reproducibility 73
4 Results 75
4.1 Open-lumen intestinal organoids show functional crypt-like and villus-like domains 77
4.2 Intestinal organoids are mechanically compartmentalized into functional domains 81
4.3 Crypt size and folding depend on substrate stiffness 83
4.4 The crypt folds through apical constriction 86
4.5 The actomyosin cortex determines cell shape and traction 93
4.6 Cell fate and mechanics co-evolve during crypt formation 98
4.7 Comparison with the intestinal epithelium *in vivo* 102
4.8 Eph/Ephrin signaling regulates crypt-villus boundary formation in open-lumen intestinal organoids 104
4.9 Cells are dragged out of the crypt 108
5 Discussion 113
6 Conclusions 125
Contributions to the data presented in this thesis 129
7 Appendix 131
Appendix 1: Computational vertex model. 133
Appendix 2: Axisymmetric Monolayer Stress Microscopy 141
8 References 145

1 Introduction

1.1 Epithelial mechanics

Epithelia are apico-basally polarized cell layers that cover all the internal and external surfaces of the animal body. They play crucial roles in physiology by protecting against external hazards (e.g. the skin), secreting hormones (e.g. insulin in the pancreas), absorbing nutrients (e.g. the intestine), exchanging gasses (e.g. the respiratory tract) or excreting toxins (e.g. the kidney). Attending to the number of cellular layers, epithelia can be simple (a single cell layer), pseudostratified (a single, very packed, cell layer with cell nuclei positioned at different heights) or stratified (more than one cell layer). Attending to the differences between the apical, basal and lateral surface area of the cells, epithelia are also classified in squamous, cuboidal or columnar (Figure 1). Squamous cells show a smaller lateral area compared to the apical and basal area. Cuboidal cells show a similar lateral, basal and apical area. Finally, columnar cells show an increased lateral area compared to the apical and basal area.

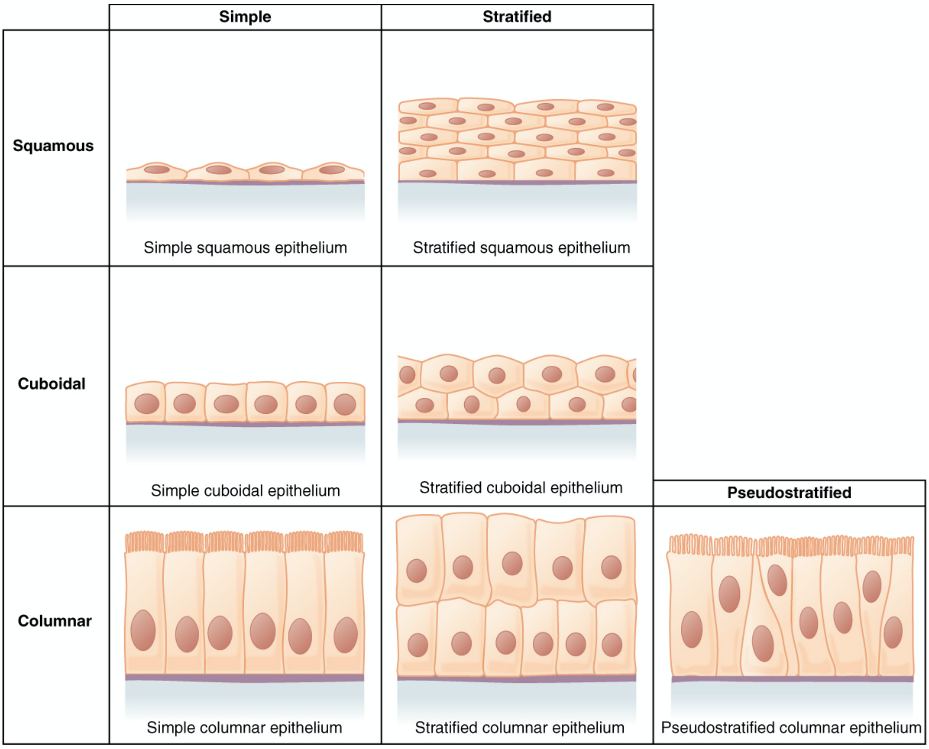
Simple
Stratified
Squamous
Simple squamous epithelium
Stratified squamous epithelium
Cuboidal
Simple cuboidal epithelium
Stratified cuboidal epithelium
Pseudostratified
Columnar
Simple columnar epithelium
Stratified columnar epithelium
Pseudostratified columnar epithelium

Figure 1. Classification of epithelia. Adapted from reference [2].

Epithelia are continuously exposed to physical forces. For instance, peristaltic contractions of muscle cells compress the intestine to induce water and food flow through the tube. At the same time, food contents generate an outward expansion of the intestinal tube and the epithelium gets stretched. A similar tissue expansion happens at the lungs, where the epithelium is stretched during air inspiration. Epithelial cells also exert forces on their surrounding environment. For example, they generate propelling forces to migrate in a certain direction during wound healing[3] or embryo gastrulation[4]. Cells integrate all these mechanical inputs into biological responses through different biochemical cascades, known as mechanotransduction.

In this section, I will briefly introduce how epithelial cells generate, endure and respond to mechanical forces, as well as the role of these forces during epithelial migration and tissue morphogenesis.

1.1.1 The cellular machinery that exerts, withstands and senses mechanical forces

In order to generate, integrate and resist mechanical forces, epithelia exploit three main cellular structures that are interconnected: The cell cytoskeleton, cell-cell adhesions and cell-ECM (extracellular matrix) adhesions.

The cell cytoskeleton

The cell cytoskeleton is a complex intracellular network, composed of three types of protein filaments: microtubules, intermediate filaments and actin filaments (Figure 2). This network is under constant remodeling thanks to specific enzymes that polymerize and depolymerize the protein filaments.

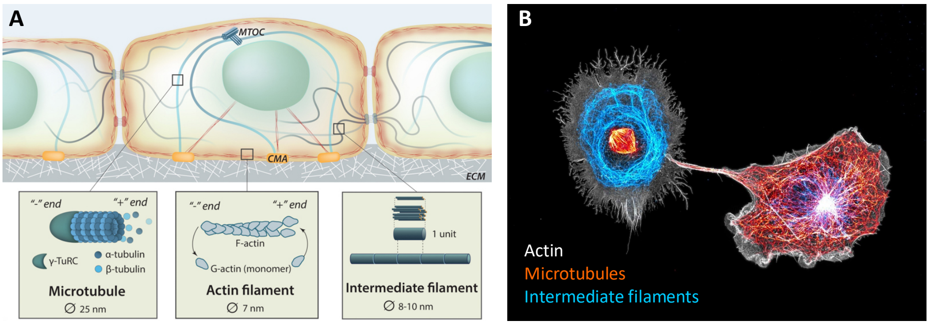

Figure 2. The cell cytoskeleton. **A**) Schematic depicting the structure of different cytoskeletal filaments (microtubules, actin filaments and intermediate filaments). Adapted from reference[5]. **B**) Cultured green monkey cells stained for actin (gray), microtubules (orange) and intermediate filaments (cyan). Image courtesy of Dr. Christophe Leterrier, NeuroCyto, INP, CNRS Aix-Marseille Université.

Microtubules are hollow filaments made of tubulin monomers that typically extend from the microtubule-organizing center (MTOC, centrosome in animal cells) towards the cell periphery. Compared to actin and intermediate filaments, microtubules are the most rigid components of the cytoskeleton[6]. They create a network that sustain cell shape, separate chromosomes during mitosis, form cilia and flagella, and act as scaffolds for motor proteins involved in intracellular transport[7].

Intermediate filaments are a large family of protein filaments, including keratins, desmin, vimentin, neurofilaments, nestins and lamins, among others[8,9]. Intermediate filaments are the most flexible component of the cytoskeleton[6]. They withstand very large strains - they can be stretched over 2 times their initial length without rupture[10] – thus acting as a mechanical buffer that protects cell integrity upon extreme cellular deformations[11–13].

Actin filaments (F-actin) are polymer chains, formed by polymerization of globular actin (G-actin) monomers. Similar to microtubules, protein motors can bind to actin filaments. Non-muscle myosins bind actin filaments and pull on them, generating a contractile force[14]. Within cells, actin filaments organize into two types of higher assemblies: actin bundles and actin networks (Figure 3)[15]. Actin bundles are fibers of parallelly-oriented actin filaments that generate a high contractile force. They are found at the cytokinetic ring (a contractile ring that splits the cell cytoplasm during mitosis)[16], at stress fibers (thick contractile bundles involved in cell-substrate adhesion, migration and mechanosensing)[17,18], at the adhesion belt (apical ring at epithelial cell-cell contacts that links the cytoskeleton of adjacent cells)[19,20], at microvilli (apical protrusions of the cell membrane)[21] or at filopodia (protrusions of migratory cells that sense the environment and provide guidance cues)[22,23]. On the other hand, actin networks are 3D meshes of branched actin filaments. As opposed to the typical contractile forces generated by actin bundles, the polymerization of actin networks can generate protrusive forces. Examples of actin networks are the cell cortex (a thin layer of actin filaments that tether the cytoskeleton to the plasma membrane)[24] or the lamellipodium (a migratory protrusion of the cell membrane induced by actin polymerization)[25,26].

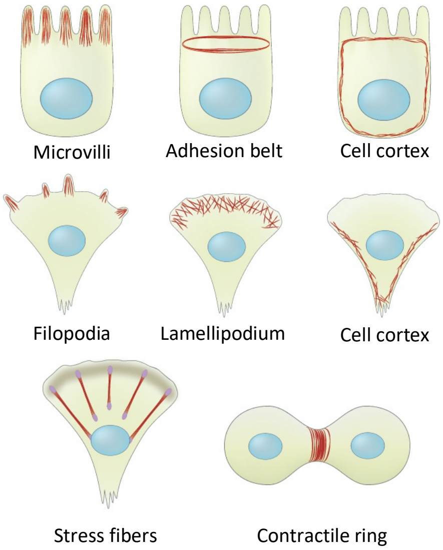

Figure 3. Different types of actin structures within the cell. Actin filaments assemble into bundles (microvilli, adhesion belt, filopodia, stress fibers, cytokinetic ring) or networks (cell cortex, lamellipodia). Adapted from reference [27].

To properly generate and transmit forces to the substrate and to neighbor cells, cytoskeletal filaments are anchored at the cell periphery to cell-cell and cell-ECM adhesion complexes (Figure 4). These connections not only favor efficient cell force generation and cell stability upon force load, but they also allow for the coordination within neighbors and collective force generation. For instance, the alignment of actin fibers within neighbor cells into supracellular actin cables enables collective contraction during wound healing[3] or the establishment of boundaries between cell populations[28,29].

Cell-Cell adhesions

Epithelial cells are rarely found as single cells. Instead, they generally form connections with other cells, assembling into tissues or cell clusters. In fact, the loss of cell-cell connections at epithelial cells is often associated with malignant processes such as cancer metastasis[30].

Epithelial cells form different types of cell-cell adhesions: tight junctions, adherens junctions, desmosomes and gap junctions (Figure 4). Tight junctions, adherens junctions and desmosomes are connected to the cell cytoskeleton, thus mechanically coupling neighboring cells. Tight junctions are strong apical cell-cell adhesions that seal the epithelium, avoiding leakage of molecules through it. They are formed by proteins including occludins and claudins (among others) and bind to the actin cytoskeleton through adaptor proteins such as ZO-1, ZO-2 and ZO-3[31]. Adherens junctions are highly dynamic lateral junctions connected intracellularly to actin filaments[32] and formed by proteins of the cadherin family. A prototypical and well characterized cadherin protein in epithelial adherens junctions is E-cadherin. E-cadherin binds intracellularly to p120-catenin, β-catenin and α-catenin, which are then linked to the actin cytoskeleton[33,34]. Adherens junctions sustain and generate mechanical stress and allow for mechanical coordination between neighbors though the adhesion belt[34–36]. Similar to adherens junctions, desmosomes are also very dynamic lateral junctions formed by proteins of the cadherin family, but they are connected intracellularly to intermediate filaments. Thus, desmosomes help protecting the cells' integrity upon large deformations[37,38]. Finally, gap junctions are basolateral channels connecting the cytoplasm of neighboring cells, allowing intercellular transport of molecules[39].

Cell-ECM adhesions

Epithelia typically sit on top of a thin ECM layer (several hundred nanometer thickness) named basement membrane, composed of laminin, collagen IV, nidogen, perlecan and other constituents[40–42]. Epithelial cells are anchored to this basement membrane through two types of adhesions: Focal adhesions and hemidesmosomes (Figure 4). Both focal adhesions and hemidesmosomes are formed by alpha- and beta-subunits of integrin proteins. However, focal adhesions are connected intracellularly to the actin cytoskeleton while hemidesmosomes are connected to intermediate filaments[43]. In focal adhesions, integrins bind actin filaments via adaptor proteins such as talin, focal adhesion kinase, vinculin or paxillin[44]. In hemidesmosomes, integrins generally bind intermediate filaments via plectin adaptor protein[45,46]. Cell-ECM adhesions are anchoring points that allow the transmission of forces from the cell cytoskeleton to the underlying substrate. These forces are crucial, for instance, to propel the cell during migration.

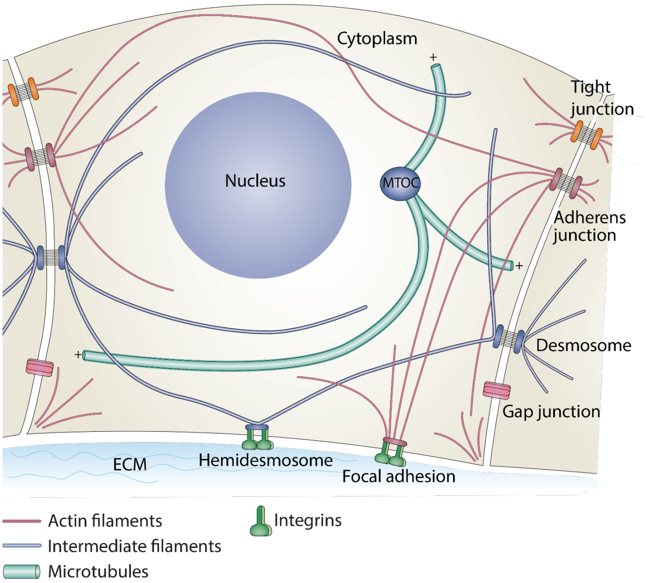
Cytoplasm
+
Tight junction
Nucleus
MTOC
Adherens junction
+
Desmosome
+
Gap junction
ECM
Hemidesmosome
Focal adhesion
Actin filaments
Integrins
Intermediate filaments
Microtubules

Figure 4. The anchoring points of the cytoskeleton: cell-cell and cell-ECM contacts. The cell cytoskeleton is anchored to the cell periphery at cell-cell and cell-ECM adhesions. Cell-cell adhesions include tight junctions, adherens junctions, desmosomes and gap junctions. Cell-ECM adhesions include hemidesmosomes and focal adhesions. Actin filaments are connected to tight junctions, adherens junctions and focal adhesions while intermediate filaments are connected to desmosomes and hemidesmosomes. Modified from reference [47], with permission from Springer Nature.

1.1.2 Mechanosensing and mechanotransduction

Epithelial cells not only generate and endure physical forces, but they also sense them and react to them through specific biological responses. Cells sense mechanical inputs through different mechanosensors. Following mechanosensing, a signal is transduced and induces a specific biological response (e.g. changes in gene expression or remodeling of the cytoskeleton).

Mechanosensing happens at different structures within the cell. Adhesion sites are well known mechanosensors. In focal adhesions and adherens junctions, pulling forces from the actomyosin cytoskeleton induce the unfolding of talin[48,49] and α-catenin[50,51], respectively, exposing their vinculin binding sites. Vinculin then binds talin or α-catenin and anchors actin fibers to the cell-ECM[52] or to the cell-cell[53] adhesion site. This leads to adhesion reinforcement, by recruitment of more adhesion molecules and by stabilization of the adhesion-cytoskeleton bond. This ultimately results in higher force generation, both because of an increase in contractility and because the reinforced adhesion is able to sustain higher load before disengaging[54–56].

Mechanosensing at cell-cell or cell-ECM adhesion can then activate a mechanotransduction pathway and induce changes in gene expression[57]. For instance, on stiff substrates where cells develop strong focal adhesions, the actomyosin contraction deforms the nucleus[58,59]. Nuclear deformation induces the opening of nuclear pores, enabling nuclear translocation of transcription factors such as YAP (Yes-associated protein) / TAZ (Transcriptional coactivator with PDZ-binding motif) (Figure 5)[59]. Alternatively, the increase in cortex tension could trigger the activation of signaling cascades[60–62] or induce the sequestering of YAP/TAZ inhibitors to the adhesion site[63,64], resulting as well in nuclear translocation of YAP/TAZ.

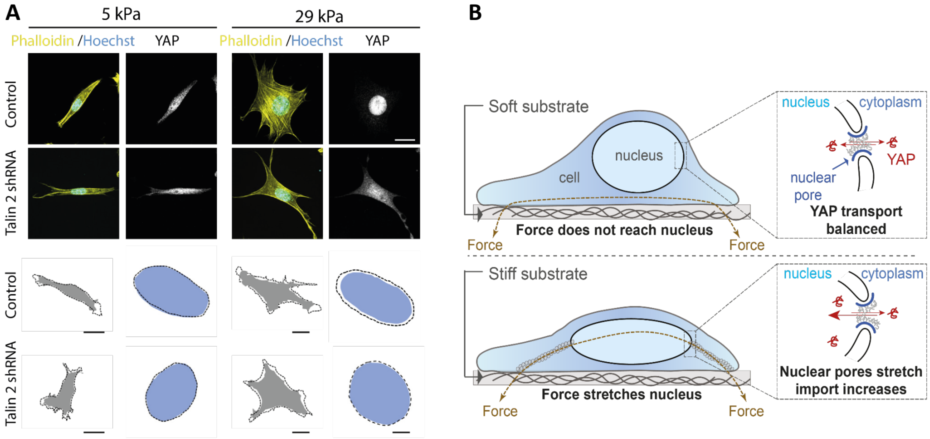
A
5 kPa
29 kPa
Phalloidin /Hoechst
YAP
Phalloidin /Hoechst
YAP
Control
Talin 2 shRNA
Control
Talin 2 shRNA
B
Soft substrate
nucleus
cell
Force does not reach nucleus
Force
Force
nucleus
cytoplasm
YAP
nuclear pore
YAP transport balanced
Stiff substrate
Force stretches nucleus
Force
Force
nucleus
cytoplasm
Nuclear pores stretch import increases

Figure 5. Cell-adhesion mechanosensing. **A) Top:** Immunostainings of F-actin (phalloidin), nucleus and YAP/TAZ. Cells seeded on stiff substrates (29 kPa) show nuclear translocation of the transcription factor YAP/TAZ (control row). Perturbation of focal adhesions abrogates nuclear translocation of YAP/TAZ (Talin 2 shRNA row). **Bottom:** Stretch experiments. In control cells on stiff substrates, the initial area of both the cell (gray) and the nucleus (blue) enlarges (dashed line) upon stretching, as tension is transmitted through the cytoskeleton and reaches the nucleus. In cells with perturbed focal adhesions (Talin 2 shRNA row), the nuclear area does not increase upon stretch, indicating that tension does not reach the nucleus. Scale bars, 20 µm. **B)** Scheme depicting the mechanism of YAP/TAZ nuclear translocation. On stiff substrates, the cytoskeletal tension reaches the nucleus and deforms it. This leads to nuclear pores opening, enhancing the nuclear translocation of YAP/TAZ. Adapted from reference [59], with permission from Elsevier.

The nuclear membrane can also act as a mechanosensor. A clear example is the response of cells to squeezing, such as immune cells when they migrate in confined environments. Squeezing of the cell induce the unruffling of the nuclear membrane and the binding of the enzyme cytosolic phospholipase A2 (cPLA$_2$) to the inner nuclear membrane. cPLA$_2$ releases arachidonic fatty acid (AA) from the nuclear membrane to the cytoplasm, where it triggers the activation of cortical myosin motors (Figure 6)[65,66].

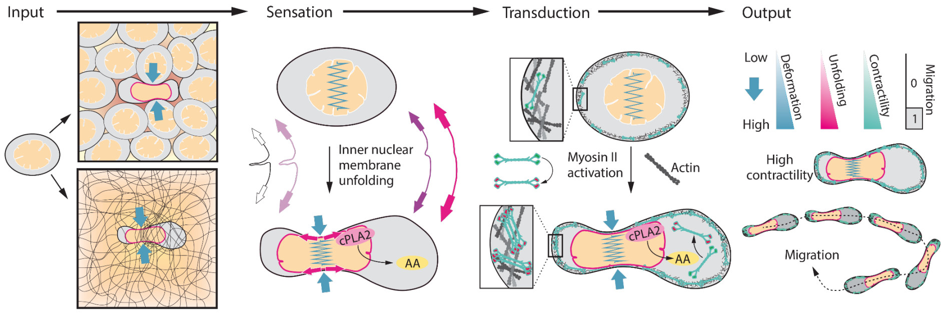
Input
Sensation
Transduction
Output
Inner nuclear membrane unfolding
cPLA2
AA
Myosin II activation
Actin
cPLA2
AA
Low
High
Deformation
Unfolding
Contractility
Migration
0
1
High contractility
Migration

Figure 6. Nuclear mechanosensing. On crowed or confined environments, the cell nucleus can get squeezed, inducing the unfolding of the nuclear membrane. Arachidonic acid is then released from the nuclear membrane to the cytoplasm where it activates myosin, enhancing contractility and cell motion. Adapted from reference[65], with permission from AAAS.

The cell membrane is also a hub for mechanosensation. In epithelial cells, different mechanoreceptors are present at the cell membrane. An example is Piezo1, a mechanosensitive calcium channel that opens under mechanical load. Calcium influx upon Piezo1 activation results in a variety of cell responses, including stimulation of cell extrusion upon compression[67,68] or division upon stretch[69].

1.1.3 Epithelial forces and tissue folding

Cellular forces sculpt the shape of epithelial tissues by folding them through different mechanisms. Folding can be generated by stresses of different sign. For instance, compressive stresses are typically associated to buckling instabilities, while differentials in tensional stresses along the apico-basal axis typically induce bending of the tissue. Attending to the source of the mechanical force, folding mechanisms could be classified in local (involving the cells at the very fold), or global (involving the neighboring cells or the whole tissue). In many cases, however, folding is not induced by a single mechanism, but it results from the coordination of local, neighboring and global forces[70].

A well characterized and extensively studied folding mechanism is apical constriction (Figure 7). During apical constriction, the actomyosin machinery is recruited to the apical side of some cells within a region of the monolayer. The coordinated actomyosin contraction induces a shrinkage of the apical cell surface, which translates into the invagination of the tissue[71,72]. Classical examples of epithelial folding mediated by apical constriction include the Drosophila gastrulation[73–77], the vertebrate neural tube formation[78–81], or the eye lens placode invagination[82–85].

Of note, apical constriction is often accompanied by basal relaxation[86]. For instance, during Drosophila ventral furrow invagination, apical constriction first induces an elongation of the cells due to volume conservation. After that, a decrease in basal myosin contractility induces basal relaxation and allows for tissue invagination[86].

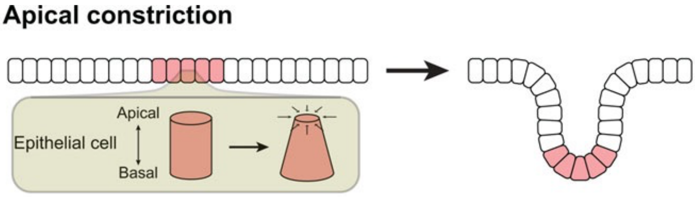

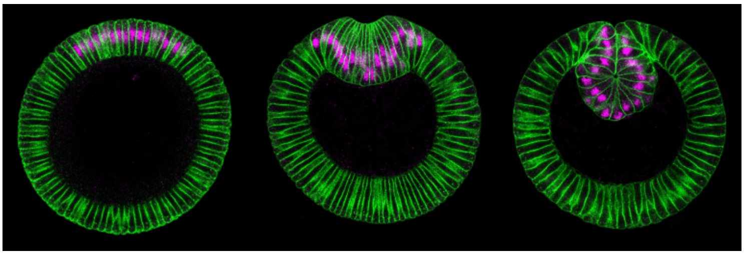

Figure 7. Tissue folding: Apical constriction. **Top:** scheme depicting the process of apical constriction. In a region of the tissue, cells reduce their apical size by actomyosin-driven constriction, leading to the folding of the monolayer. Adapted from reference[87], with permission from The Company of Biologists Ltd. **Bottom:** Apical constriction during Drosophila embryo gastrulation (ventral furrow formation). Note the decrease in the apical area of the cells at the invagination region (center image). Green: membrane, Magenta: Snail. Image courtesy of the He lab (Dartmouth College, U.S.).

An interesting example of apical constriction is the leg imaginal disc invagination in Drosophila. In this case, basally extruding cells increase and stabilize apical actomyosin in the neighbors. The coordination of extrusions at a localized region generates a local apical tension that results in the invagination of the tissue[88,89].

Lateral shift of apical junctions can also induce folding[70,90,91]. During the formation of dorsal folds in Drosophila embryos, some cells move their apical junctions along the apico-basal axis to a lower position. This repositioning of the apical junctions generates deformation of the apical surface of their neighbors, which is then relieved by bending of the epithelium[70,91] . Of note, this mechanism is independent of actomyosin asymmetric distribution[70,91].

Although less common than apical constriction, basal constriction also generates tissue folding. During optic cup morphogenesis[92–95] or during the formation of the midbrain-hindbrain boundary[96,97] neuroepithelial cells fold the tissue by basally constricting. Importantly, basal constriction requires integrin-mediated adhesion to the ECM, which allow the transmission of tension along the tissue to coordinate the folding[93–97].

In many instances, the folding of the tissue is not only mediated by the cells in the fold but forces from cells at the vicinity of the fold strongly contribute to the folding process. A clear example is the Drosophila salivary gland invagination. In this case, local apical constriction of the cells at the fold acts in conjunction with a compressive supracellular actomyosin ring at the neighbors that induces buckling of the tissue (Figure 8A). Folding in this tissue can happen in the absence of apical constriction, although the final tissue shape is abnormal, indicating a tightly regulated coordination between bending by local apical constriction and buckling by neighbor compression[98].

Cells at adjacent tissues can also contribute to epithelial folding. During ventral furrow formation in Drosophila gastrulation, mesoderm invagination is mediated by apical constriction but the late steps in the process depend on buckling instabilities induced by lateral compression from the ectoderm[99]. During lung branching morphogenesis, the bifurcation of epithelial buds is mediated by the presence of smooth muscle cells that physically wrap the bud (Figure 8B)[100]. Another example is the emergence of villi in the mammalian intestine. In this case, the compaction of the ECM by mesenchymal cells below the intestinal epithelium generate an initial folded dome that later further develops into a villus[101–104].

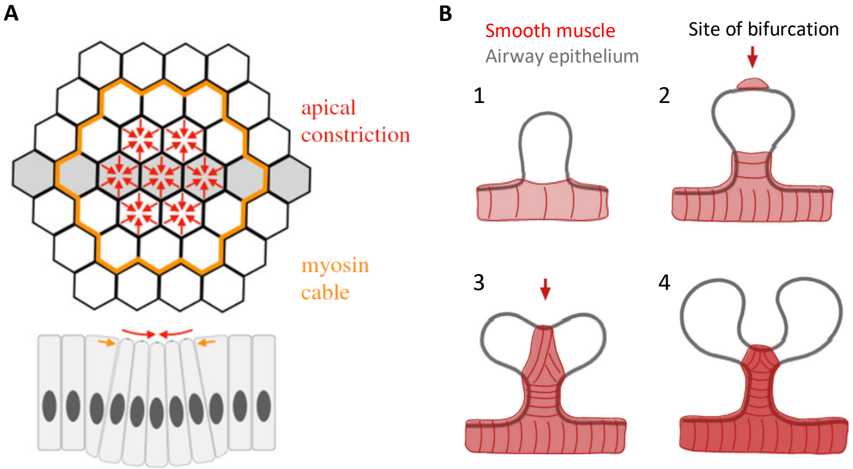

Figure 8. Tissue folding: coordination between local and adjacent forces. **A)** Scheme of the Drosophila salivary placode folding mechanism. An apical constriction from the cells at the fold is combined with a contractile actomyosin ring by the neighbors. Adapted from reference[70], with permission from The Royal Society (U.K.) **B)** Scheme of the airway epithelium branching during lung development. At the site of bifurcation, muscle cells wrap the tissue to constrict and fold the epithelia into shape. Adapted from reference[100], with permission from Elsevier.

A more complex interplay between epithelial and adjacent tissue forces takes place during the invagination of the hair follicle placode[105]. In a first step, the apical tension of the epithelial tissue is combined with the compression of a basal actomyosin ring around the placode formed by fibroblasts beneath, triggering the elongation of the epithelium along the apico-basal axis and some degree of invagination. In a second step, softening of the ECM by metalloproteinases leads to the release of epithelial compression, inducing epithelial cell divisions and further invagination. This mechanism is reminiscent of the salivary gland placode invagination (Figure 8A). However, the apical tension during hair follicle placode invagination does not seem to be restricted to the folding area[105].

Mechanical instabilities at the tissue scale can also generate folding. Growth under confinement or differential growth in the tissue plane or between two tissues can induce in-plane compressive forces in the epithelium that result in tissue buckling (Figure 9A)[106,107]. For instance, epithelial monolayers growing inside alginate drops experience buckling when the maximum available area is filled (Figure 9B)[108]. Another example is the intestinal looping during development, where the intestinal tube buckles due to its faster growth compared to the adjacent mesenchyme. In the chicken, the growth of the intestinal epithelium under the confinement imposed by the adjacent muscular layers induces its buckling into villi[109,110]. A similar growth-induced folding has been proposed for the folding of the cerebral cortex[111–115] and the dental epithelium during tooth germ development[116].

Buckling can be also induced by exogenous application of a compressive force. When suspended epithelial monolayers are compressed, they undergo buckling (Figure 9C)[117]. Interestingly, these experiments showed that the pre-tensional state of the cell layers due to the actomyosin cortex can buffer up to ~35% compressive strain. Compressive strains above this threshold induce the formation of stable buckles[117].

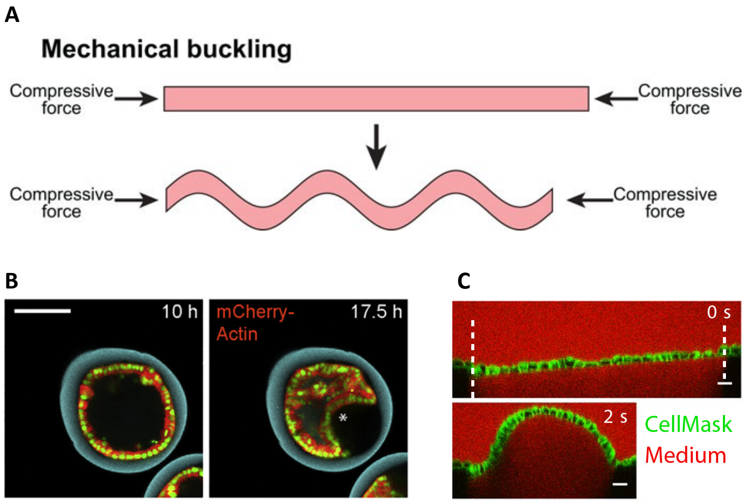

Figure 9. Tissue folding: buckling. **A)** Scheme of the mechanism of buckling-mediated folding. Confined tissue growth or lateral application of force to a tissue generates a compressive stress that ultimately leads to folding. Adapted from reference [87], with permission from The Company of Biologists Ltd. **B)** MDCK monolayers grown under confinement inside alginate drops. Over time, the compression induced by the growth induces buckling of the tissue (17.5h, asterisk). Nuclei are labelled in green. Scale bar, 100 µm. Adapted from reference [108]. **C)** Suspended MDCK monolayers exposed to compressive force undergo buckling. Scale bars, 20 µm. Adapted from reference [117], with permission from Springer Nature.

1.1.4 Epithelial forces and collective cell migration

Fundamental processes such as embryogenesis or tissue regeneration require collective motion of multicellular entities. To collectively migrate, epithelial cells coordinate as clusters (e.g. the neural crest) or sheets (e.g. the skin).

Within advancing epithelial sheets, a front-rear ("leader" - "follower") polarization of the multicellular system typically takes place[118–120]. At the front of the epithelial monolayer, "leader" cells extend protrusive lamellipodia via actin polymerization[121]. At the lamellipodial protrusions, new focal adhesions are formed and anchor cytoskeletal actomyosin fibers that contract to propel the cell forward[34,119]. Because "leader" cells are connected to "follower" cells through cell-cell adhesions, propelling of the leader cells generates a pulling force that drags follower cells in the direction of motion[34,119].

Nevertheless, pulling forces from cells at the leading edge are not sufficient to drive the motion of the epithelial sheet. Force measurements on expanding epithelial monolayers showed that, although cells at the leading edge exert higher traction forces on the substrate[35,122], cells far away from the edge still generate active tractions (Figure 10A)[35]. To generate these tractions, follower cells extend basal protrusions (cryptic lamellipodia) under the cells located at their front[35,123] (Figure 10B).

Thus, cells at the leading edge and cells rows behind are mechanically coordinated to migrate as a collective. This coordination is, in part, achieved by force transmission through cell-cell junctions. As cell tractions are not balanced at the single cell level, gradients of tension emerge from the leading edge to the core of the monolayer, where cell-cell tension is maximal (Figure 10A, C)[35,36]. Interestingly, cell-cell tension is a mechanical cue that gives directionality to the collective migration. Cells align and migrate parallel to the direction of maximum principal stress, a phenomenon known as plithotaxis[36].

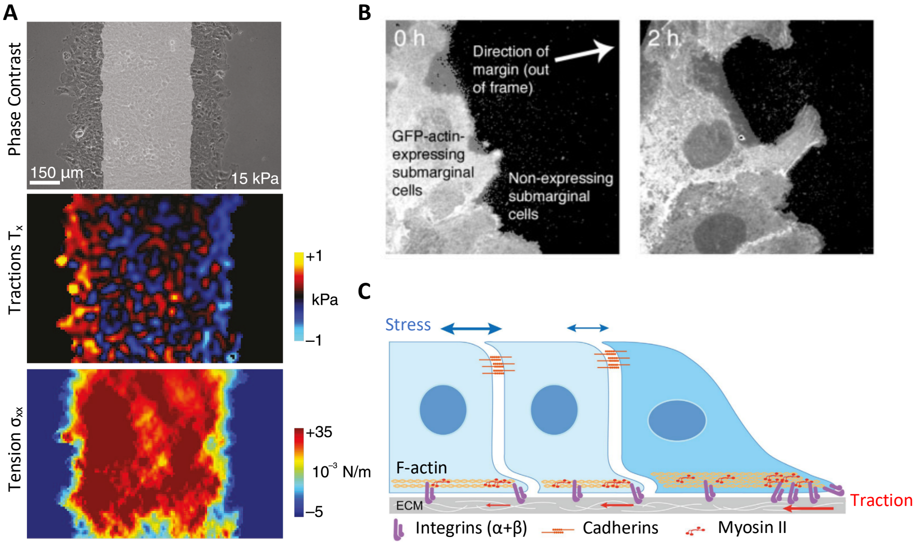
A
Phase Contrast
150 µm
15 kPa
Tractions T_x
+1
kPa
–1
Tension σ_{xx}
+35
10^{-3} N/m
–5
B
0 h
Direction of margin (out of frame)
GFP-actin-expressing submarginal cells
Non-expressing submarginal cells
2 h
C
Stress
F-actin
ECM
Traction
Integrins (α+β)
Cadherins
Myosin II

Figure 10. Collective cell migration: Leader-follower coordination. **A)** Phase contrast (top panel), cell-ECM tractions (T_x, middle panel) and cell-cell Tension (σ_{xx}, bottom panel) of an expanding monolayer of MCF-10A epithelial cells. Note that, although at both free edges of the monolayer cells exert high tractions, cells at rows behind the leading edge still exert significant forces. Cell-cell tension is minimal at the edge of the expanding monolayer and increases towards its center. Adapted from reference[124], with permission from AAAS. **B)** Snapshots of GFP-expressing MDCK follower cells during a wound healing experiment. Note the protrusion of cryptic lamellipodia underneath their neighbors at the front (The black areas correspond to non-transfected cells closer to the free edge of the monolayer). Adapted from reference[123], with permission from The Company of Biologists Ltd. **C)** Mechanical coordination between leaders and followers during collective cell migration. Cells at the leading edge (leaders) exert higher traction via lamellipodia extension, focal adhesion formation and actomyosin contraction. Follower cells also extend cryptic lamellipodia and exert tractions in a similar fashion. Leaders and followers are mechanically coupled by cell-cell adhesions. This creates a gradient of increasing tension from the edge to the center of the monolayer. Adapted from reference[125], with permission from the American Society for Cell Biology.

Epithelial cells are exposed to other biochemical and mechanical cues that guide the directionality of the collective motion. Epithelial collectives follow gradients of substrate stiffness (durotaxis)[124,126,127], chemoatractant gradients (chemotaxis)[128,129] or extracellular matrix gradients (haptotaxis)[130,131].

Of note, not all epithelial systems show a clear leader-follower behavior. For instance, during neural crest migration in Xenopus, contraction of cells at the rear of the cell cluster propels it forward[128] (Figure 11). A similar mechanism has been recently proposed for lateral line primordium migration in zebrafish, where higher stresses exerted by rear cells propel the cluster forward[132]. Moreover, in the absence of a free edge in the epithelial monolayer, cells can migrate behaving as single cells (their traction forces are balanced at the single cell level) but coordinate with neighbors for the motion of the whole cellular sheet[133].

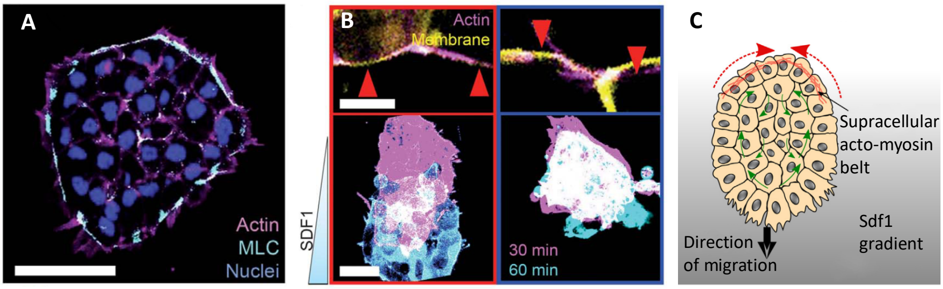

Figure 11. Collective cell migration: rear propulsion. **A)** During Xenopus neural-crest migration, an actin cable forms at the periphery of the cluster (MLC, myosin light chain). Scalebar, 50 µm **B)** Laser ablation of the actomyosin ring at the rear of the cluster (right panel) but not at the front (left panel) abrogate cluster migration along the SDF1 gradient. Arrowheads indicate the points of ablation. Scalebars, 10 µm (top) and 50 µm (bottom). A) and B) are adapted from reference [128], with permission from AAAS. **C)** Scheme of the process. Adapted from reference[134], with permission from Elsevier.

In summary, collective epithelial migration is an emergent phenomenon, whereby the mechanical coordination of individual cells into a supracellular entity allows collective motion.

1.2 The intestinal epithelium and its experimental models

1.2.1 Anatomy of the mammalian intestine

The adult mammalian intestine is a hollow tube that extends from the end of the stomach to the anus (Figure 12A). This tube is composed of different concentric cell layers. From the outer-most to the inner-most, these layers include a connective tissue layer (serosa), a longitudinal muscle layer, a circular muscle layer, a connective tissue layer (submucosa), another longitudinal muscle layer (muscularis mucosa), a connective tissue layer (lamina propria) and the epithelium (Figure 12B)[135,136].

The intestinal tube - although it is physically a continuum - can be functionally and morphologically divided in different segments along the rostro-caudal axis (Figure 12A). The small intestine extends from the end of the stomach to the cecum and is subdivided in duodenum, jejunum and ileum, from rostral to caudal. The large intestine comprises the rest of the tube and it is subdivided in cecum, proximal colon, mid colon, distal colon, rectum and anus, from rostral to caudal[135].

The intestinal epithelium constitutes the inner-most cell layer of the gut, directly facing the intestinal lumen (Figure 12B). It is composed of columnar epithelial cells that are attached to a basement membrane rich in Collagen IV and Laminin[137,138]. The intestinal epithelium acts as a physical barrier that protects against pathogens and other external agents, but at the same time, it absorbs nutrients from food digestion and secretes molecules such as antimicrobials or hormones. The structure of the intestinal epithelium largely varies along the different segments of the intestinal tube (Figure 12C). At the small intestine, the intestinal epithelium is folded into finger-like protrusions towards the lumen called villi and invaginations into the stroma called crypts (Figure 12C). The length of villi decreases from duodenum to ileum and villi are completely absent in the large intestine (Figure 12C). The length of the villi is optimal for the specific function of each intestinal segment. At the proximal small intestine (duodenum and jejunum) long villi considerably enlarge the absorptive surface area of the epithelium. Thus, most of the nutrient absorption takes place in these segments.

At the ileum, cells specialize in the absorption of bile acids and vitamin B12. At the large intestine, devoid of villi, nutrient absorption is virtually absent and cells specialize in water absorption[139].

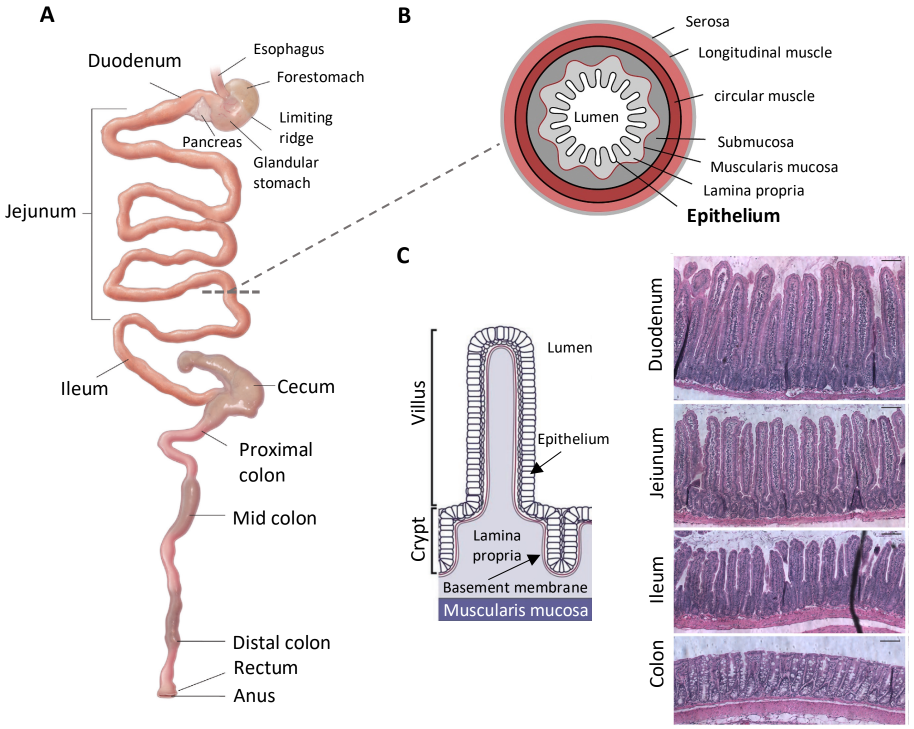
A
Duodenum
Esophagus
Forestomach
Limiting ridge
Pancreas
Glandular stomach
Jejunum
Ileum
Cecum
Proximal colon
Mid colon
Distal colon
Rectum
Anus
B
Serosa
Longitudinal muscle
circular muscle
Lumen
Submucosa
Muscularis mucosa
Lamina propria
Epithelium
C
Villus
Crypt
Lumen
Epithelium
Lamina propria
Basement membrane
Muscularis mucosa
Duodenum
Jejunum
Ileum
Colon

Figure 12. Anatomical features of the intestine. **A)** Structure of the gastrointestinal tube. The intestine is divided along the rostro-caudal axis in small intestine (duodenum, jejunum and ileum) and large intestine (cecum, proximal colon, mid colon, distal colon, rectum and anus). Adapted from reference[135], with permission from Elsevier. **B)** Scheme of a transversal view of the intestinal tube. The different concentric tissue layers are indicated. Adapted from reference[136]. The publisher for this copyrighted material is MaryAnn Liebert, Inc. publishers. **C) Left:** Structure of the intestinal epithelium. Note the finger-like protrusions towards the lumen (villi) and the invaginations into the stroma (crypts) [140], with permission from Springer Nature. **Right:** Hematoxylin/eosin staining of intestinal cuts at the indicated segments. Note the decrease of villus size from the duodenum to the ileum and the absence of villi in the colon. Scale bar, 100 µm. Adapted from reference[141].

1.2.2 The intestinal epithelium: cell types and dynamics

The folded shape of the epithelium of the small intestine establishes two functional domains – the crypt and the villus. At the villus, differentiated cells absorb nutrients and secrete hormones and other molecules and eventually die at the tip. At the crypt, cells proliferate to constantly repopulate the villus (with a turnover rate of about 3-5 days[142]). For that, intestinal stem cells (ISCs) located at the bottom of the crypts divide and give rise to progenitor cells, which further proliferate at the transit amplifying region and differentiate into the other intestinal epithelial cell types (i.e. Goblet cells, Enterocytes, Tuft cells, Enteroendocrine cells, M cells, Paneth cells). Differentiated cells migrate up the villus (or the surface epithelium in the colon) and finally extrude and die at the tip (Figure 13)[143–147]. Paneth cells are an exception, as they migrate down the crypt to support stem cells[148,149].

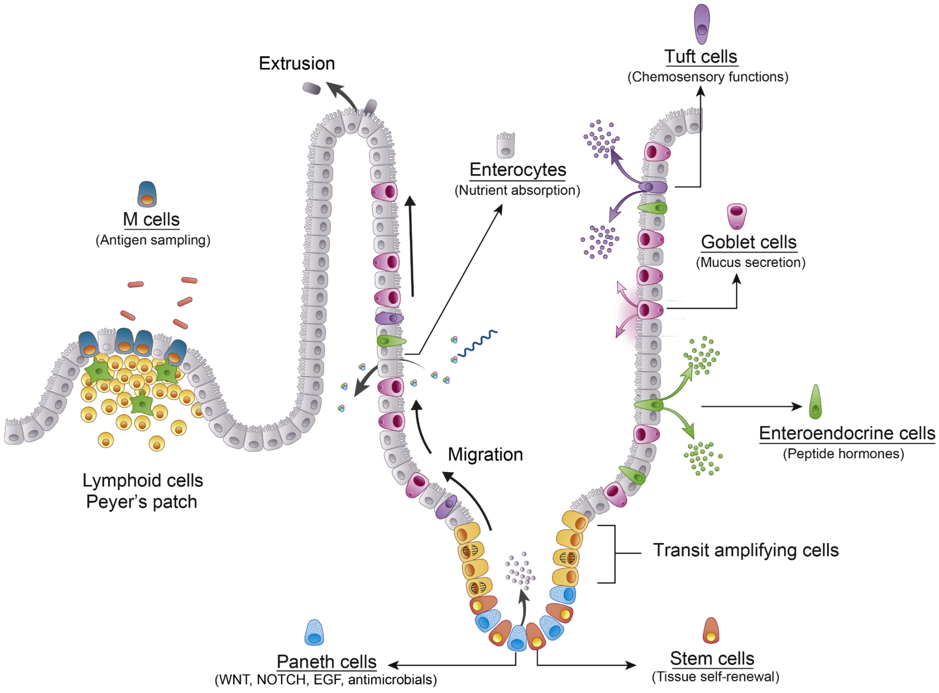
Extrusion
Tuft cells
(Chemosensory functions)
Enterocytes
(Nutrient absorption)
M cells
(Antigen sampling)
Goblet cells
(Mucus secretion)
Enteroendocrine cells
(Peptide hormones)
Lymphoid cells
Peyer's patch
Migration
Transit amplifying cells
Paneth cells
(WNT, NOTCH, EGF, antimicrobials)
Stem cells
(Tissue self-renewal)

Figure 13. The mammalian small intestinal epithelium. Structure of the small intestinal epithelium. The different cell types (Stem cells, Paneth cells, Goblet cells, Enterocytes, Enteroendocrine cells, Tuft cells and M cells) as well as their main functions are indicated. Stem cells divide at the bottom of the crypt. Some daughter cells enter the transit amplifying region, where they start differentiating into

the absorptive or secretory lineage by lateral inhibition. After some rounds of divisions, cells exit the transit amplifying region and migrate to the top of the villus, where they are extruded at the tip. Adapted from reference[150], with permission from Elsevier.

Intestinal Stem Cells

ISCs were first described in the 70s by Cheng and Leblond as very thin cells intermingled with Paneth cells at the crypt base. They were called crypt base columnar (CBC) cells[151]. Cheng and Leblond performed rudimentary but powerful tracing experiments showing that the differentiated cells originated from these CBC cells. By injecting ^{3}H-thymidine to the mice, some of the CBC cells died and were phagocytosed by surviving CBC cells, forming radioactive phagosomes in their cytoplasm that were traceable. Over time, these phagosomes were found in differentiated cells, indicating that these differentiated cells are descendants of a CBC cell[152]. It was in 2007 when leucine-rich repeat-containing G protein-coupled receptor 5 (LGR5) was described as the first bona fide marker of ISCs[153]. Since then, other markers have been described, including Achaete scute-like 2 (ASCL2)[154] , Olfactomedin-4 (OLFM4)[155,156] or SPARC-related modular calcium-binding protein 2 (SMOC2)[157], among others. Interestingly, the mouse adult stem cell pool does not arise exclusively from LGR5+ fetal cells. Instead, the whole fetal epithelium - including villus cells – contribute to the formation of the adult stem cell pool[158].

ISCs divide symmetrically (both daughter cells have the same probability to stay as stem cell) every 24h[159,160]. Interestingly, lineage tracing experiments have shown that the pool of adult intestinal stem cells is monoclonal [159,161]. This means that at any given point, all the stem cells of a crypt share a common ancestor. This monoclonality is achieved through neutral competition for the space. In this model, when a stem cell is stochastically lost (e.g. if the two daughter cells differentiate) it gets replaced by a neighbor stem cell resulting from a symmetric division[159].

At the bottom of the crypts (stem cell niche), stemness is sustained by different biochemical signals, including Epidermal growth factor (EGF), Wingless/Integrated (Wnt) and Notch. These signals are provided by sub-epithelial mesenchymal cells and Paneth cells[143–145].

After division, the progeny of the stem cell enters the transit amplifying region (TA) and differentiates. Differentiation at the TA is known to be dependent on Delta-Notch lateral inhibition. Notch receptor activation by Delta ligands induces the expression of HES1 transcription factor, which is a repressor of *Atoh1* gene. When *Atoh1* is repressed, cells differentiate towards the absorptive lineage (Enterocytes, M cells). In the absence of Notch signaling, ATOH1 is expressed (not inhibited by HES1) and cells differentiate towards the secretory lineage (Goblet, Paneth, Enteroendocrine, Tuft)[144,160]. At the crypt, Paneth cells express Delta ligands (DLL1 and DLL4), while stem cells express the receptors (Notch1 and Notch2). At the border of the stem cell niche, stem cell progeny loses the contact with a Paneth cell. *Atoh1* starts being expressed in these cells as Notch signaling shuts down. Some of these cells start differentiating towards the secretory lineage and start expressing Delta ligands. These Delta ligands activate Notch receptors in the neighbor cells that did not enter yet differentiation[144]. The Notch active cells then undergo ~4-6 round of divisions and differentiate into the absorptive lineage. On the contrary, secretory progenitors are proposed to divide slower [162,163].

Paneth cells

Paneth cells were described before ISCs by Gustav Schwalbe and Joseph Paneth[164,165]. Paneth cells reside at the bottom of the crypts, intermingled with ISCs, and are characterized by a cytoplasm full of secretory granules. As opposed to the relatively short life of differentiated cells, Paneth cells reside at the bottom of the crypt for 3-4 weeks before they die[166,167]. As commented, Paneth cells provide Wnt, Notch and EGF signals to sustain stem cell fate[144,168]. *In vivo*, however, Paneth cell depletion has no impact on stem cell behavior, indicating that the presence of similar signals from the stroma or other epithelial cells are sufficient to maintain stem cell function[169–171]. Paneth cells also secrete a plethora of other molecules, including antimicrobial enzymes such as alpha-defensins (cryptdins in mice) or lysozyme[164]. Paneth cells are more abundant at the ileum[172] and virtually absent in the colon[173–175], where most of their stem cell supportive functions are taken over by Reg4+ deep secretory cells[176].

Paneth cell differentiation requires Wnt activation and Notch inactivation[144]. Interestingly, in opposition to the upward migration of the other differentiated cells, differentiating Paneth cells migrate towards the bottom of the crypt[148,149]. This downward migration is proposed to be driven by repulsive forces between EphB3 expressing Paneth cells and EphrinB1 expressing cells at higher positions of the crypt (see section 1.3.1.4 for further details on Eph/Ephrin signaling)[177].

Goblet cells

Goblet cells are the most abundant population of the secretory lineage. They secrete mucus to create a protective and lubricating layer over the epithelium[162]. They are also involved in antigen presentation to dendritic cells to create antigen tolerance[178]. As opposed to Paneth cells, Goblet cell differentiation is induced by both Wnt and Notch inactivation[144,179]. The number of goblet cells increase along the rostro-caudal axis of the intestine[180–183].

Enteroendocrine cells

Enteroendocrine cells specialize in the secretion of hormones. Attending to the type of hormone that they secrete they are classified in different subtypes[184]. Besides their primary secretory function, they can serve as a reserve source of Notch signaling for stem cells upon Paneth cell depletion[185].

Tuft cells

Tuft cells are a very rare epithelial cell type. Although they derive from DLL+ secretory progenitors, their differentiation does not depend on ATOH1 or other transcription factors of the secretory lineage[144,186]. Tuft cells are chemosensory cells and they play a crucial role in immune response to infection. Upon helminth infection, tuft cells release Interleukin-25, which activates tissue-resident group 2 innate lymphoid cells (ILC2s). ICL2s then release Interleukin-13 at the bottom of the crypt, activating receptors of the ISCs and secretory progenitors and biasing the differentiation towards Tuft and goblet cells. This tuft and goblet cell metaplasia later facilitates helminth expulsion[162,187–189]. Moreover, similar to Enteroendocrine cells, Tuft cells provide Notch signals to stem cells upon Paneth cell depletion[185].

Enterocytes

Enterocytes are the most abundant intestinal epithelial cell type and are specialized in the absorption of nutrients. They are characterized by the presence of a very pronounced brush border formed by cilia. These cilia increase the surface area of the epithelium, thus increasing absorption efficiency[190].

Enterocyte differentiation requires Wnt inactivation and Notch activation[144]. Of note, enterocytes are not a homogeneous population, but rather show spatial zonation along the villus axis. At the bottom of the villus, enterocytes express an antimicrobial genetic program. In the central region of the villus, they express carbohydrate, peptide and fat absorption machineries. At the villus tip, they express enzymes involved in anti-inflammatory pathways[191].

M cells

M cells are a specific cell type found at the intestinal epithelium located over Peyer patches, that are lymphoid follicles containing immune cells. M cells regulate immune responses by transporting antigens and bacteria to the antigen presenting cells in the Peyer patch[150,192]. M cell differentiation requires the activation of nuclear factor-kB (RANK) by RANK ligands (RANKL) expressed by subepithelial stromal cells covering the Peyer Patch[193].

1.2.3 Intestinal organoids

Despite the inherent physiological relevance of *in vivo* and *ex vivo* models of the intestinal epithelium, they are experimentally challenging and their applicability to mechanistic questions poses some technical limitations. On the other hand, *in vitro* models based on immortalized cells lines show limited resemblance to the native tissue. To fill this gap, intestinal organoids have emerged as gold standard *in vitro* models that recapitulate more closely intestinal epithelium physiology.

Closed-lumen organoids

In their original set up, intestinal organoids are 3D cell structures with an enclosed lumen (closed-lumen organoids) that are embedded in Matrigel or other Extracellular matrix (ECM) gels[194]. They are formed by the proliferation, self-assembly and differentiation of ISCs (Figure 14A). They can be generated from intestinal crypts[194], single ISCs[194,195] or through differentiation of induced pluripotent stem cells[196,197]. Importantly, intestinal organoids maintain key physiological features of the native tissue. For instance, they are compartmentalized into crypt-like and villus like domains. In closed-lumen organoids, crypt-like domains appear as protrusive buds containing proliferative cells, ISCs and Paneth cells. The villus-like domains are interbud regions containing differentiated cells (Figure 14B, C). Much like in the *in vivo* tissue, proliferation occurs at the crypt-like domain while dead cells are shed to the organoid lumen at the villus-like regions.

Despite being powerful *in vitro* models, closed-lumen organoids present some technical limitations for specific applications. For instance, in closed-lumen organoids, the apical surface of the cells faces the lumen, and thus, it is hardly accessible for experimental manipulation. This hinders their applicability to experiments such as bacterial infection or drug treatments, which physiologically would happen through the lumen of the intestine. Moreover, as closed-lumen organoids grow, dead cells unphysiologically accumulate in the enclosed lumen. For this reason, organoids must be broken down into small pieces and reseeded regularly. This can lead to the question of whether closed-lumen organoids model intestinal homeostasis or conversely, they better model intestinal regeneration[195].

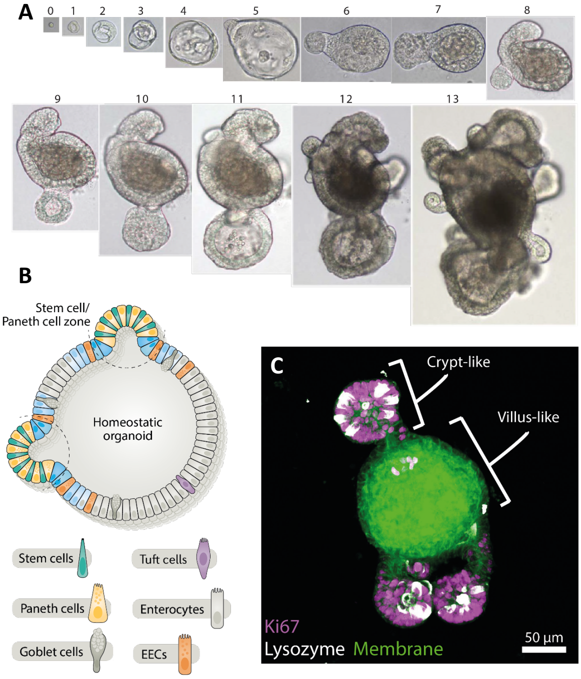
A
0
1
2
3
4
5
6
7
8
9
10
11
12
13
B
Stem cell/
Paneth cell zone
Homeostatic
organoid
Stem cells
Tuft cells
Paneth cells
Enterocytes
Goblet cells
EECs
C
Crypt-like
Villus-like
Ki67
Lysozyme
Membrane
50 µm

Figure 14. Closed-lumen intestinal organoids. **A)** Phase contrast time course of a closed-lumen intestinal organoid grown from a single intestinal stem cell. The days of culture are indicated on top of the respective images. Adapted from reference[194], with permission from Springer Nature. **B)** Scheme of the intestinal organoid with the different cell types. The budding regions are crypt-like domains containing Stem cells, Paneth cells and Proliferative cells. The interbud regions are villus-like regions containing differentiated cells. Adapted from reference[144], with permission from Springer Nature. **C)** Immunostaining of a closed-lumen intestinal organoids. Note the presence of Paneth cells (Lysozyme^{+}) and proliferative cells (Ki67^{+}) at the crypt-like regions. Scale bar, 50 µm. Image by Gerardo Ceada.

Open-lumen organoids

Recently, open-lumen organoids have emerged as new *in vitro* models of the intestinal epithelium. In open-lumen organoids, ISCs or crypts (from the *in vivo* tissue or from closed-lumen organoids) are seeded over a substrate (and not embedded in it). The substrate can be for instance an ECM gel, a synthetic hydrogel coated with ECM, or a silicone gel coated with ECM.

In the simplest form, open-lumen organoids are grown over flat substrates. Under these conditions, they self-organize into crypt- and villus-like regions (Figure 15-top)[198–201]. By using this model, Thorne et al.[199] showed for example that epithelial-intrinsic Wnt and BMP signals precisely control the proliferation and patterning of the crypt-like region. A limitation of this flat open lumen organoid format is that the location of the crypt-like and villus-like structures is not controlled and depends on the self-organization of the tissue. Different strategies have been recently followed to localize the crypt-like domains in flat open-lumen organoids. One of these strategies is the use of transwell inserts with a membrane having holes with the typical diameter of a crypt. A medium rich in factors supporting stem cell fate is added at the basal compartment of the transwell, while a medium containing low amount of factors is added at the apical compartment. As the tissue grows, stem cells localize at the holes (as they have access to the basal factors) while the rest of the tissue differentiates[201–203]. Alternatively, microprinting of circular islands of Wnt3a proteins over a Matrigel substrate has been also used to pattern crypt-like regions in open-lumen organoids[204].

Open-lumen intestinal organoids can be also generated over scaffolded substrates with the shape of the crypt/villus (Figure 15-bottom). In these scaffolds, proliferative regions containing ISCs and Paneth cells become restricted to the concave regions (crypt-like) whereas differentiation and cell death localize at the convex regions (villus-like)[205–208]. Different types of substrates have been used as scaffolds, including ECM hydrogels[206,207], polyethylene glycol diacrylate (PEGDA)-based hydrogels[209] or Polydimethylsiloxane (PDMS) silicone gels[208]. Of note, ECM hydrogels have a low strength and are susceptible to protease degradation by the cells[205]. Thus, in order to generate scaffolds that sustain epithelial coverage, ECM proteins are typically cross-linked[205,207]. Besides the crypt-villus topology, other physiological parameters have been replicated in scaffolded organoids. For instance, the application of shear stress - mimicking the flow of fluids through the intestinal tube – stabilizes the epithelial layer for longer culture periods[207]. Some scaffolded open-lumen organoids also include the formation of gradients of ISC-stimulating factors[205,209] , which help establishing the *in vivo*-like compartmentalization of the proliferative and differentiated cells along the crypt-villus axis[205,209]. Stromal cells can be embedded in the ECM-based scaffolds, further mimicking the *in vivo* scenario[206,207].

Flat open-lumen organoids

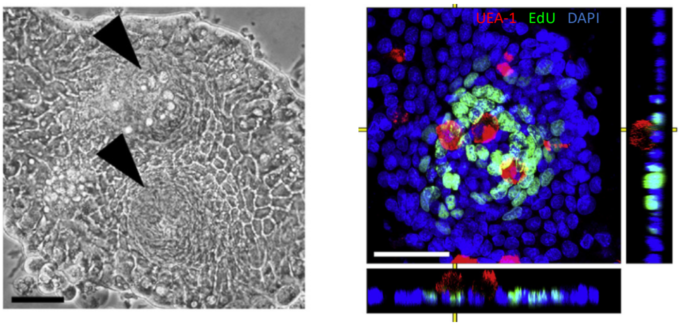

Scaffolded open-lumen organoids

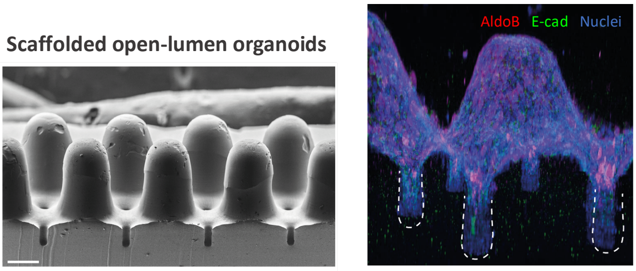

Figure 15. Open-lumen organoids. **Top:** Intestinal organoids grown over a flat substrate (Matrigel). In these flat conditions they are able to self-organize into crypt-like regions (dense circular regions indicated with arrowheads in the left phase contrast image) and villus-like regions (the surrounding tissue, composed by differentiated cells). Note the presence of proliferative cells (Edu^{+}) and Paneth cells (UEA-1^{+}) in the crypt-like regions (right panel). Adapted from reference[199], with permission from Elsevier. **Bottom:** Intestinal organoids grown over PDMS scaffolds with the shape of villus and crypts (left image). Note the presence of differentiated cells (AldoB^{+}) at the villus-like regions (right image). Scalebar, 200 µm. Adapted from reference[208], with permission from AAAS.

Importantly, the apical side of the cells is easily accessible in open-lumen intestinal organoids, which renders them ideal for infection and host-microbe interaction studies. For example, all the different phases of the infection by the parasite *Cryptosporidium parvum* could be modeled in open-lumen organoids[206]. These experiments are otherwise much more challenging on closed-lumen organoids, where the pathogen should be microinjected in the lumen of a single organoid[210,211]. Another advantage of open-lumen organoids is that dead cells can be easily flushed out by medium change. Moreover, open-lumen organoids can be maintained for longer periods of time, better mimicking intestinal homeostasis[206,208].

1.3 Mechanobiology of the intestinal epithelium

Biochemical gradients produced by epithelial cells and the sub-epithelial stroma ensure proper morphogenesis and sustain proper functioning of the intestinal epithelium throughout life. As previously explained, higher Wnt, EGF and Notch at the bottom of the crypt induces and maintaining stem cell fate. Conversely, the increase in BMP signals along the crypt-villus axis guides differentiation[143–145].

Besides the very important role of different biochemical signals in intestinal physiology, mechanical forces exerted or withstood by the intestinal epithelium also have a pivotal contribution during intestinal epithelium development and homeostasis. In this section, the role of mechanical forces in morphogenetic and homeostatic processes of the intestinal epithelium is highlighted.

1.3.1 Intestinal morphogenesis

1.3.1.1 Early steps

Once the primitive gut is formed, the midgut starts looping in a very coordinated manner to finally form the small intestine and proximal colon (the distal colon originates from the hindgut). Initially, the faster growth of the midgut compared to the surrounding tissue generates a first rotation of the tube when it no longer fits the body cavity (Figure 16A). This rotation happens anticlockwise (leftward) due to asymmetries in the architecture and mechanical properties along the right-left axis of the mesentery (a peritoneal layer that attached the gut tube to the abdominal wall). Cell-cell adhesion forces increase at the left side of the mesentery, compacting the tissue, while the ECM stiffness likely increases at the right side due to swelling[212,213]. This mechanical imbalance ultimately tilts the intestinal tube towards the left (Figure 16A).

However, as the embryo further develops, this first rotation is insufficient to fit the whole intestine in the body cavity, so the gut tube continues looping. Interestingly, further looping of the gut tube is controlled by compressive forces (mechanical buckling). These compressive forces emerge from the higher growth rate of the intestinal tube compared to its supportive mesentery. Consequently, the mesentery gets stretched and pulls on the intestine, deforming it into regular loops (Figure 16B)[214,215].

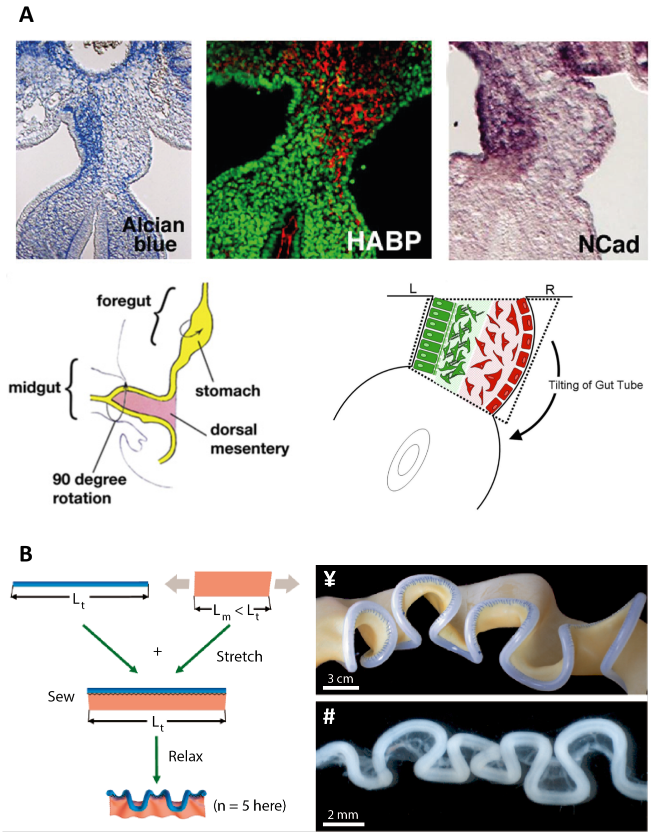
A
Alcian blue
HABP
NCad
foregut
midgut
stomach
dorsal mesentery
90 degree rotation
L
R
Tilting of Gut Tube
B
L_t
$L_m < L_t$
+
Stretch
Sew
L_t
Relax
(n = 5 here)
¥
3 cm
#
2 mm

Figure 16. Intestinal looping during early morphogenesis. **A) Top:** Alcian Blue (labeling acidic glucosaminoglycans) and HABP (in red, labeling hyaluronic acid) stainings in a developing chicken embryo indicating differences in the ECM composition of the left and right side of the midgut dorsal mesentery during the first rotation. As hyaluronic acid tends to attract water, swelling of the ECM at the right side could increase the stiffness. The high N-cadherin staining at the left side of the dorsal mesentery indicates a stronger cell-cell adhesion force, favoring compaction of the mesentery. **Bottom:** scheme of the process. The differences in cell compaction and ECM composition of the dorsal mesentery bias the rotation of the developing gut towards the left side. Adapted from reference[212], Copyright (2008) National Academy of Sciences and reference[213], with permission from Elsevier. **B)** Buckling instabilities due to differences in growth between the epithelial layer and the mesentery

generate further looping of the intestinal tube. The differential growth could be modeled with a physical model (schematized at the left panel). In this model, a thin latex sheet mimicking the mesentery (in orange) is stretched and then bound to a silicone rubber tube mimicking the gut tube (in blue). Upon relaxation, the model is able to generate loops (panel ¥) similar to those observed in the developing gut tube of a chicken embryo (panel #). Adapted from reference[214], with permission from Springer Nature.

1.3.1.2 Villification

The next morphogenetic event is the emergence of villi (villification). In the chick embryo, formation of the different muscular layers confines the growth of the pseudostratified intestinal epithelium and induces its folding via mechanical buckling. First, the inner circumferential muscular layer forms, generating a radial physical boundary to the epithelium and generating compressive forces as the epithelium keeps expanding. This compression leads to the formation of epithelial folds that expand longitudinally along the anterior-posterior axis (Figure 17). Then, the emergence of the outer longitudinal muscular layer further compresses the epithelium in the longitudinal direction, deforming the epithelial folds into a zig-zag pattern (Figure 17). Finally, the inner longitudinal muscular layer (muscularis mucosae) that emerges between the circumferential muscular layer and the epithelium instruct the formation of villi (Figure 17)[109,110,216].

In the mammalian intestine, villi do not form from ridges that later zig-zag, but from single domes that emerge in the flat epithelium[217,218]. Initially, villification in the mouse was showed to follow the same muscle-induced epithelial buckling of the chick embryo[109,110]. However, later works argue that this is not the case[102,103,219]. Instead, mouse villification seems to be induced by mesenchymal clusters that form beneath the epithelium (Figure 18)[102–104]. Mesenchymal clusters induce a change in the shape of the epithelial cells above, which become shorter along the apico-basal axis and expand laterally. This generates compressive stresses on the proliferative cells that lie in between mesenchymal clusters. The compressive stresses ultimately lead to apical invaginations of the tissue at mitotic rounding sites, setting the boundaries between emerging villi (Figure 18B,E)[220]. At the same time, these mesenchymal clusters likely pull on the ECM to deform the epithelium into a dome, that will further develop into a mature villus[101].

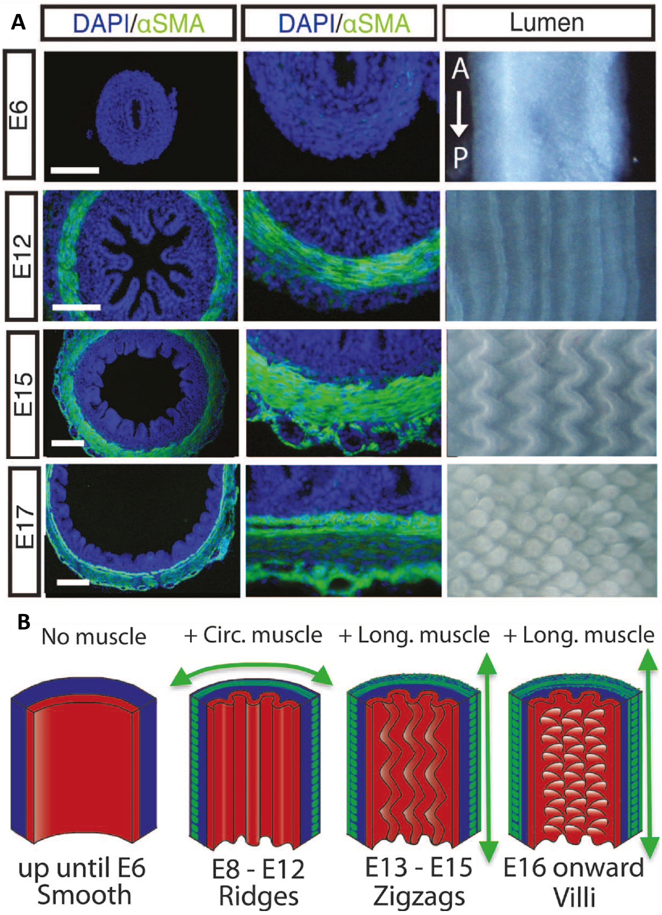
A
DAPI/αSMA
DAPI/αSMA
Lumen
E6
E12
E15
E17
A
P
B
No muscle
+ Circ. muscle
+ Long. muscle
+ Long. muscle
up until E6
Smooth
E8 - E12
Ridges
E13 - E15
Zigzags
E16 onward
Villi

Figure 17. Chick villification. **A)** Gut tubes of chicken embryos at different developmental stages (E6-E17, E = Embryonic day). **Left column:** Immunostaining of nuclei (DAPI) and muscle cells (αSMA) in transversal cuts. **Middle column:** close-ups of the left column. **Right column:** longitudinal views of the gut lumen. The anterior (A) to posterior (P) axis is indicated. Scale bars, 100 μm. **B)** Scheme of the villification process in the chicken. At E6, no muscle layer is present, and the epithelium is flat. By E12, the circumferential muscle layer is formed, and epithelial folds along the anterior-posterior axis appear. By E15, the emergence of the longitudinal muscle layer deforms the folds into zig-zags. Finally, by E17, villi emerge with the formation of the inner longitudinal muscle layer. Adapted from reference[110], with permission from AAAS.

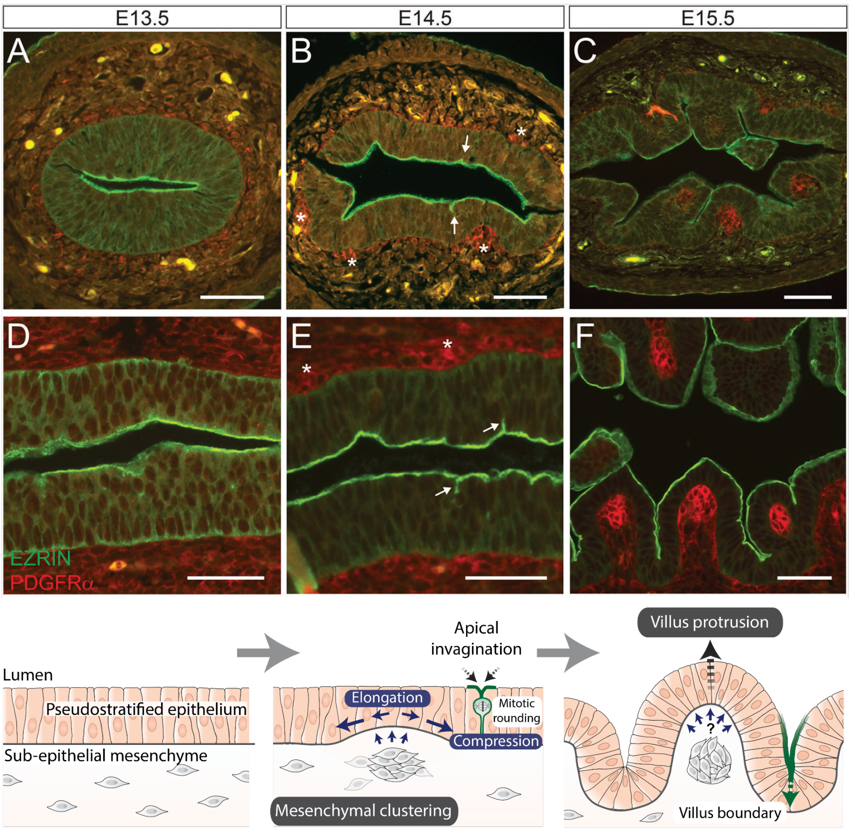
E13.5
E14.5
E15.5
A
B
C
D
E
F
EZRIN
PDGFRα
Lumen
Pseudostratified epithelium
Sub-epithelial mesenchyme
Apical invagination
Elongation
Mitotic rounding
Compression
Mesenchymal clustering
Villus protrusion
?
Villus boundary

Figure 18. Mouse villification. **Top:** Immunostainings of EZRIN (green, apical marker) and PGFRα (red, mesenchymal cells) in mouse gut tubes at different developmental stages (E13.5 -E15.5, E = Embryonic day). A-C are transversal cuts and D-F are longitudinal cuts. Note in panels B and E the formation of mesenchymal clusters beneath the epithelium (asterisks) and apical invaginations of the epithelium (arrows) at the positions where the villi and intervillus regions will emerge, respectively. Scale bars, 50 μm. Adapted from reference[220], with permission from Oxford University Press. **Bottom:** Scheme of the villification process in the mouse. Mesenchymal clusters emerge beneath the pseudostratified epithelium and induce a change in the epithelial cells, which expand laterally. This generates a compressive stress in the neighbors and apical invaginations at mitotic rounding sites. Villi and intervillus regions then emerge at the cluster and apical invagination sites, respectively. Adapted from reference[221], with permission from Elsevier.

Emergence and shaping of the villus thus seem to greatly depend on the mesenchyme. This is further supported by the fact that intestinal organoids (where the mesenchyme is absent) show villus-like regions that are not folded (Figure 14, Figure 15). However, intestinal epithelial cells can generate villus-like folds if subjected to shear stress[222] or cyclic stretch[223], further supporting the notion that the intestinal epithelium can be sculpted by mechanical forces into villi structures.

1.3.1.3 Crypt morphogenesis

As villi form, Hedgehog (Hh) protein secreted by epithelial cells locally accumulates beneath the developing villi, inducing the secretion of BMP signals by mesenchymal cells. BMP signals, in turn, impose differentiation of epithelial villus cells and cell proliferation gets restricted to the intervillous regions, where crypts will later emerge[102,103,109].

In the mouse, crypts emerge after birth[224] while in humans they form during gestation[225]. A recent work shows that Myosin II-driven apical constriction of intervillous progenitor cells induce crypt invagination[226] (Figure 19). The bending forces that induce crypt folding *in vivo* are thus very likely generated by the epithelial cells. However, the contribution of the supporting mesenchyme has not been directly assessed and remains an open question.

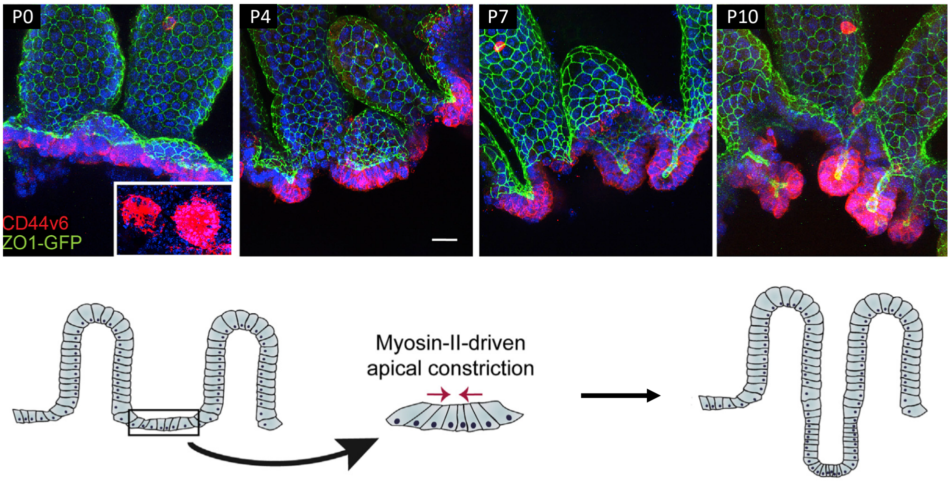

Figure 19. Crypt morphogenesis. **Top:** Whole-mount immunostainings of the mouse intestinal epithelium at different developmental stages (P0-P10; P = Postanal day). Nuclei are shown in blue, progenitor cells (CD44v6) in red and the apical membrane (ZO1) in green. Scale bar, 20 µm. Bottom: Scheme of crypt morphogenesis. Cells at intervillus regions apically constrict to induce invagination of the crypt. Adapted from reference [226], with permission from Elsevier.

Of note, the fact that intestinal organoids are able to fold into crypts in the absence of a supporting mesenchyme, highlights the sufficient contribution of epithelial forces to crypt morphogenesis. Apical constriction has been proposed as necessary for crypt budding in intestinal organoids[227]. However, a quantitative measurement of the epithelial forces that allow for tissue bending and crypt invagination is still missing.

1.3.1.4 Crypt-villus compartmentalization

Once crypts have invaginated, a dynamic boundary between the crypt and villus emerges. At this boundary, cells are basally constricted and expand apically, forming a "hinge" (Figure 20). Hinge cells display Rac1 activation, which suppresses hemidesmosome formation and allows for the cell shape remodeling required for basal constriction (Figure 20)[226].

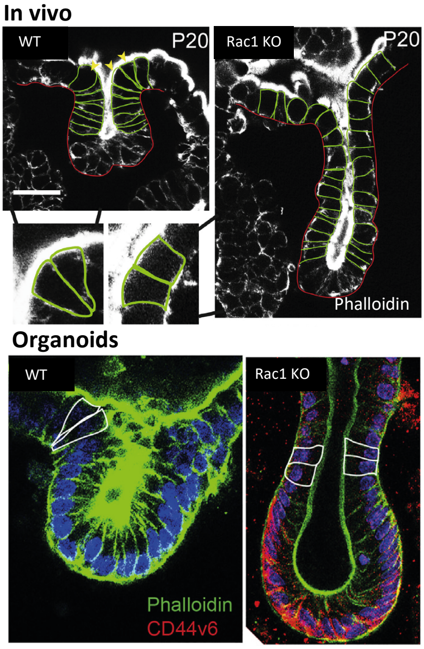

Figure 20. Hinge formation at the crypt-villus boundary. F-actin (phalloidin) immunostainings of mouse intestinal epithelium *in vivo* (top) and in organoids (bottom) for wildtype and Rac1 KO conditions. In organoids, only Rac1 KO condition was stained for progenitor cells (CD44v6). Note the

basal constriction of the WT cells at the crypt-villus boundary both *in vivo* (arrowheads, and green outlined cells in zoomed insets) and in organoids (white outlined cells). In Rac1 KO condition, cells at the crypt-villus boundary are not basally constricted neither *in vivo* nor in organoids. Scale bar *In vivo*, 20 µm. Adapted from reference[226], with permission from Elsevier.

The force-generating mechanism that leads to basal constriction in hinge cells and how proper crypt-villus compartmentalization is mechanically sustained at long-term remains, however, unknown.

To ensure proper functioning of the intestinal epithelium, the different cell types must then remain correctly positioned at their specific compartment. In this context, the Eph/Ephrin signaling pathway plays a crucial role. Eph/Ephrin signaling involves a receptor (Eph) and a ligand (Ephrin) expressed at the cell membrane. There are two families of both receptors and ligands. In general, EphA receptors bind EphrinA ligands and EphB receptors bind EphrinB ligands, although there is some level of cross-reactivity[228]. EphA and B receptors share the same structure (Figure 21): i) an extracellular region, where they bind Ephrin ligands, that is composed of a ligand binding domain followed by a cysteine rich domain and two fibronectin-type III domains, ii) a transmembrane domain and iii) an intracellular region, where a phosphorylation cascade initiates upon ligand binding, that is composed of a Tyrosine kinase domain followed by a sterile alpha motif (SAM) and a PDZ binding domain. EphrinA and B ligands, however, do not share the same structure. Ephrin B ligands are composed of an extracellular receptor binding domain, a transmembrane domain and an intracellular region containing a PDZ binding domain. Ephrin A ligands have an extracellular receptor binding domain, but they are anchored to the cell membrane via a Glycosylphosphatidylinositol (GPI)-linker (Figure 21)[228,229].

In vertebrates, 16 Eph receptors (EphA1-EphA10 / EphB1-EphB6) and 9 Ephrin ligands (EphrinA1-EphrinA6 / EphrinB1-EphrinB3) have been reported[230].

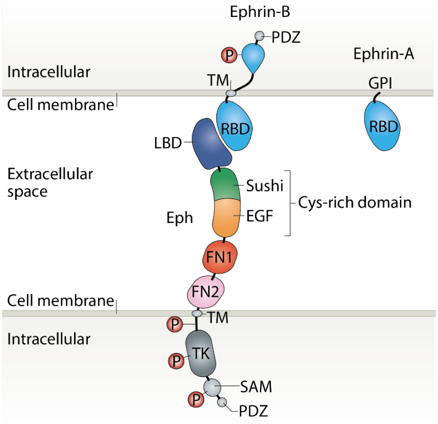
Ephrin-B
PDZ
P
Ephrin-A
Intracellular
TM
GPI
Cell membrane
RBD
RBD
LBD
Extracellular space
Sushi
Cys-rich domain
Eph
EGF
FN1
FN2
Cell membrane
TM
P
Intracellular
TK
P
SAM
P
PDZ

Figure 21. Structure of Eph receptors and Ephrin ligands. Adapted from reference [228], with permission from Springer Nature.

When cells expressing the Eph receptor encounter cells expressing the Ephrin ligand, both cells transduce a signal (bidirectional signaling). This signal can lead to repulsion, cell segregation or boundary formation, among other responses[228].

In the intestinal epithelium, Eph and Ephrin proteins are expressed in counter-gradients along the crypt-villus axis. EphB2, 4 and 3 receptors have maximum expression at the crypt and their expression decreases towards the villus. EphB3 expression is more restricted to the bottom of the crypt. EphrinB1 and 2 ligands, on the contrary, show minimal expression at the crypt and their expression increases towards the villus (Figure 22)[177,231,232]. Genetic perturbation of EphB receptors or EphrinB ligands leads to defects in cell positioning and crypt-villus compartmentalization. In EphB3 Knock out (KO) , EphB2/3 double KO or EphrinB1 KO mouse, Paneth cells are no longer restricted to the bottom of the crypts (Figure 22)[177,233–235]. Of note, EphA receptors and EphrinA ligands are also expressed differentially along the intestinal epithelium, although their function remains yet to be determined[236].

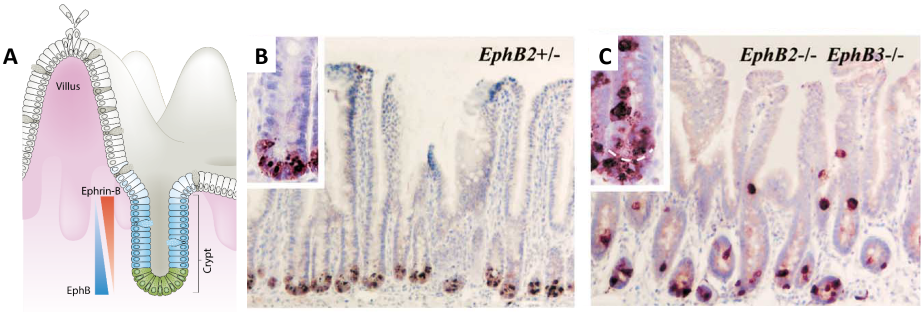

Figure 22. Eph-Ephrin signaling in the intestinal epithelium. **A)** Scheme depicting the expression pattern of EphB receptors and EphrinB ligands in the intestinal epithelium. Note that EphB3 expression is more restricted to the bottom of the crypt[177] (not indicated for simplicity). Adapted from reference[228], with permission from Springer Nature. **B-C)** Paneth cells (purple), typically restricted to the bottom of the crypts (**B**), are mispositioned along the crypt-villus axis in mouse KO for EphB receptors (**C**). Adapted from reference[177], with permission from Elsevier.

Differential adhesion between progenitor cells and differentiated cells downstream of EphB/EphrinB signaling is proposed to maintain crypt-villus compartmentalization[237]. *In vitro* experiments in MDCK and Co115 cells showed that $EphB^+$ cells activate the metalloproteinase ADAM10 at the contact with $EphrinB^+$ cells. ADAM10 activation triggers E-Cadherin sheeding, decreasing the adhesion between EphB and EphrinB expressing cells and leading to the sorting of the two cell populations[237]. Of note, a dominant negative ADAM10 expressed in Paneth cells recapitulates the mispositioning phenotype observed in EphB2/3 KO mice, further supporting this differential adhesion mechanism[237].

In the intestinal epithelium, however, cells at the crypt-villus boundary express both the EphB receptors and EphrinB ligands. Thus, additional mechanisms to differential adhesion are expected to play a role in crypt-villus compartmentalization.

Interestingly, actomyosin-driven cell constriction is observed at the boundary between EphB and EphrinB expressing cells (Figure 23)[29,238,239]. Increase in cortical tension via actomyosin contractility is crucial for cell sorting of Eph and Ephrin expressing cell populations[28,240,241]. Furthermore, much like basal constriction of hinge cells at the crypt-villus boundary, Eph/Ephrin-mediated cell sorting requires active Rac1[242,243]. An appealing hypothesis is that Eph/Ephrin signaling could induce actomyosin-driven basal constriction of hinge cells at the crypt-villus boundary. However, this hypothesis has not been experimentally addressed to date.

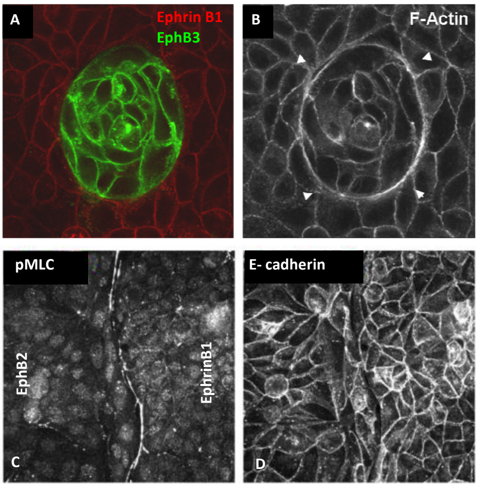

Figure 23. Actin cable formation at the boundary of EphB and EphrinB cells. **A)** MDCK cells expressing either the EphrinB1 ligand (red) or the EphB3 receptor (green) sort out when mixed. **B)** An actin cable forms at the boundary between EphB and EphrinB sorted populations. A and B are adapted from reference[239]. **C-D)** Similar results are found at the collision site of two expanding MDCK monolayers expressing either EphB2 or EphrinB1. Note the accumulation of phospho-myosin light chain (pMLC) at the boundary between the two cell populations (**C**). Adapted from reference[29], with permission from Springer Nature.

1.3.2 Proliferation and cell fate

In the adult intestinal epithelium, mitosis is restricted to ISCs and transit amplifying cells and it takes place at the apical surface of the monolayer. After mitosis, daughter cells reintegrate in the epithelium either as neighbors or far away from each other. As previously mentioned, gradients in biochemical factors regulating cell fate are established along the crypt villus axis. Consequently, the distance of the reintegration site to the bottom of the crypt influences the exposure level of daughter cells to specific biochemical factors, affecting their fate.

Interestingly, some of these signaling pathways can be activated by mechanical cues. For instance, Wnt signaling is enhanced by tissue compression. Tissue compression imposes intracellular molecular crowding, favoring the sequestration of the β-catenin destruction complex to the plasma membrane and thus increasing the translocation of β-catenin to the nucleus[244]. Additionally, β-catenin bound to E-cadherin also respond to compressive stress. Upon compression, β-catenin gets phosphorylated and is released from E-Cadherin adherens junctions, to then translocate to the nucleus[245]. By contrast, Notch signaling respond to pulling forces. In this case, pulling forces induce a conformational change of the Notch receptor, triggering its intracellular cleavage and downstream signaling[246].

YAP driven mechanosensing also regulates intestinal proliferation and cell identity. In intestinal organoids, transient and heterogeneus YAP inactivation regulates crypt budding. Buds develop from an initial cyst composed of cells all displaying nuclear YAP. As the cyst grows, some cells experience cytoplasmic translocation of YAP (presumably due to the increase in cell density and compression) and a symmetry breaking event takes place. The cells that retain nuclear YAP start expressing Notch ligands and differentiate into Paneth cells, defining the localization of the nascent crypt (Figure 24A)[195] . This is mainly due to the secretion of Wnt signals from Paneth cells that support the formation of the stem cell niche[208]. Substrate stiffness also affects YAP signaling in the intestinal epithelium. When intestinal organoids are grown on matrices of 1.3kPa, nuclear YAP translocation favor cyst formation. However, crypt budding and intestinal stem cell differentiation requires matrix softening[247].

Whether YAP enhances or abrogates intestinal stem cell fate is still quite controversial[248–254]. The conflicting results often found in the literature might be explained by the context-dependent role of YAP in regeneration and homeostasis, as well as in the redundancy of the mechanical and biochemical cues regulating this pathway.

Tissue curvature constitutes another physical cue that can instruct intestinal cell fate. In open lumen organoids grown over scaffolded substrates, ISCs localize at the bottom of concave regions, while differentiated cells localize at the convex regions[205,206,208]. Concave curvature generates a region of increased local density that elicits crypt specification via the same YAP-Notch driven symmetry breaking commented before (Figure 24B)[208]. Although tissue geometry can help guiding intestinal cell fate, curvature is not necessary for proper crypt-villus specification, as open-lumen organoids grown over flat surfaces self-organize into crypt- and villus-like structures with correct cell specification[198–200].

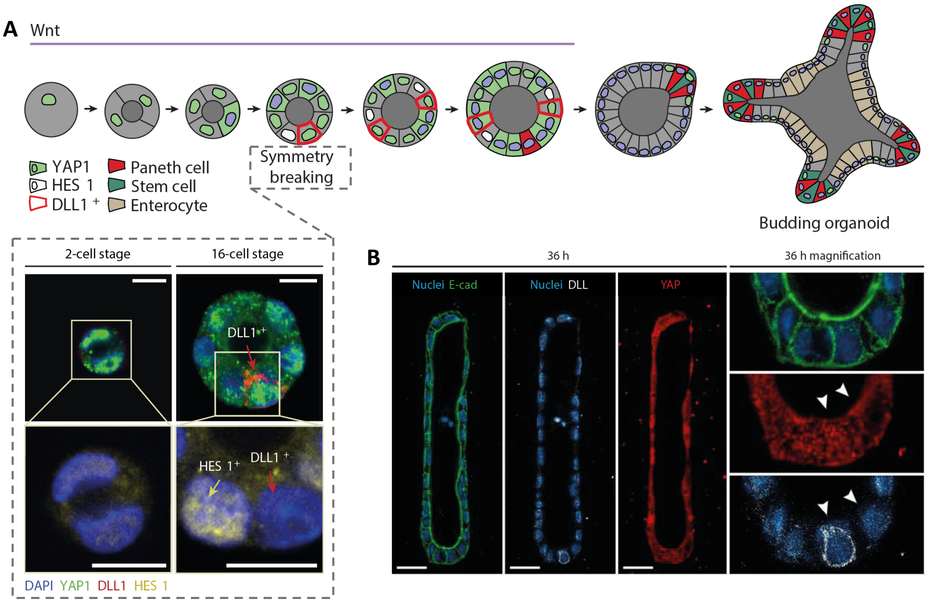

Figure 24. YAP-mediated symmetry breaking and crypt initiation of intestinal organoids. **A)** Scheme of the steps of intestinal organoid formation from a single cell. The first step is the formation of a cyst, where cells display nuclear translocation of YAP. As the cyst grows, YAP nuclear translocation becomes heterogeneous and the cyst breaks its symmetry. Some of the cells retain nuclear YAP and start expressing the Notch ligand DLL1. These cells later differentiate into Paneth cells and stop expressing YAP. The YAP-Notch symmetry breaking event is highlighted in the dashed box immunostainings. Note the expression of the Notch target gene (HES 1) in the neighbors of DLL1+ cells that display nuclear YAP. Scale bars, 10 µm. Adapted from reference[195], with permission from Springer Nature. **B)** Local increase in cell density at regions of concave curvature induce the same YAP-Notch symmetry breaking mechanism depicted in panel A. In this case, organoid cells are seeded on ellipsoidal microcavities in the ECM. At the edges of the microcavities, cell density increases, leading to heterogeneous activation of YAP and the YAP-Notch symmetry breaking event. Cells displaying nuclear YAP become DLL1+ and differentiate into Paneth cells. Arrowheads denote adjacent pairs of cells displaying nuclear/non-nuclear YAP. Adapted from reference[208], with permission from AAAS.

1.3.3 Migration along the crypt-villus axis

During intestinal homeostasis, the movement of new cells from the bottom of the crypt to the tip of the villus allows for a constant renovation of the epithelium. For a very long time, mitotic pressure has been thought to drive passive cell migration from the crypt to the tip of the villus. In this model, the reintegration of new cells into the tissue after division generates a compressive force on their neighbors, displacing the whole cell monolayer towards the villus tip [152,255,256].

However, this model is inconsistent with evidence in the literature showing that inhibition of proliferation does not affect epithelial migration in the intestine[257–260]. Recent *in vivo* and *ex vivo* experiments by Krndija et al. corroborate these results, showing that inhibition of proliferation at the crypt do not affect migration at the villus (Figure 25A)[261].

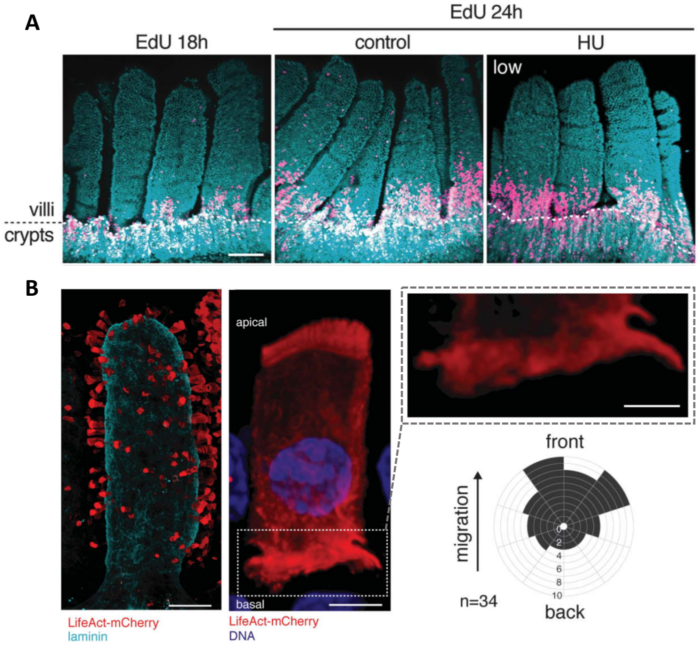

Figure 25. Active migration in the intestinal epithelium. **A)** Inhibition of proliferation do not prevent migration along the villus. 18h post Edu injection (EdU 18h panel) mice were treated with Hydroxyurea to stop proliferation. 6h after treatment, (EdU 24h panel), the migrated distance of the Edu+ cells along the villus is similar in both control and treated animals. Scale bar, 50 µm. **B) Left:** A mosaic

intestinal epithelium showing lifeact-mcherry expression (labelling actin, showed in red) in sparse individual cells. Scale bar, 50 µm. **Middle:** Super-resolution image of a villus cell extending cryptic lamellipodia in the direction of migration. Scale bar, 4 µm. The basal side of the cell is zoomed in the dashed panel, where the lamellipodia is visible at the right side of the image. Scale bar, 2 µm. **Bottom right:** Rose plot showing the normalized basal protrusion length at different angles along the front-back axis of the migrating cells. Note that protrusions extend in the direction of movement (front). **A**) and **B**) Adapted from reference[261], with permission from AAAS.

Krndija et al. also show that the villus epithelium is under tension, not compression as expected by the mitotic pressure scenario. Furthermore, differentiated cells establish a front-rear polarity and extend cryptic lamellipodia at their front to actively migrate towards the villus tip (Figure 25B)[261]. Thus, migration along the intestinal villus is not a passive process downstream of mitotic pressure. Instead, it is an active phenomenon where cells exert propelling forces on the underlying substrate.

Active migration in the intestinal epithelium has been thoroughly tested within the villus region. However, whether active cell migration also governs the movement of cells along the crypt[262] and their transition towards the villus requires further investigation.

1.3.4 Cell extrusion

After exiting the crypt and actively migrating along the villus, differentiated cells reach the top of the villus and are extruded to the lumen[146]. Although most of the extrusion happens at the villus tip[146,263], extruding events have been also observed below the tip[263,264]. This has been associated to a fixed lifespan of intestinal epithelial cells, so that migratory cells that exhaust their lifespan before reaching the villus tip undergo extrusion[256,264].

During the extrusion process, extruding cells lose their contacts with the ECM and redistribute the cell-cell junctions with the neighbors, in such a way that the epithelium is sealed during and after the extrusion[265,266]. Defects in the extrusion process are associated with intestinal diseases including bacterial infection, inflammation and cancer[267–271].

In epithelial monolayers, cells can be extruded alive or once apoptosis has been initiated. In both cases, extruding cells release Sphingolipid 1 phosphate (S1P), which activates its receptor ($S1P_2$) on the neighbor cells and induces the formation of an actomyosin ring. The actomyosin ring contracts and squeezes the extruding cell, expelling it apically from the monolayer (Figure 26A)[67,272,273].

Interestingly, live cell extrusion can be induced by compression[67,274]. Compressive stresses due to overcrowding activate the mechanosensitive channel Piezo1 in the extruding cell, triggering the release of S1P and consequent extrusion cascade (Figure 26A).

Whether cells in the intestinal epithelium extrude alive or dead is still a matter of debate. Indeed, both types of extrusion are observed in the intestinal epithelium (Figure 26B)[67,208]. At the villus tip, where cells are overcrowded[261], compressive stresses are proposed to induce live cell extrusion following activation of Piezo1[67]. Moreover, contrarily to previous results, compression could also induce apoptotic cell extrusion via caspase activation[274]. Thus, both apoptotic and non-apoptotic extrusion could be triggered by the same mechanical input (compression) at the villus tip, redundantly ensuring the expelling of cells. Topological defects (local singularities in the orientational order of the cells)[275] induce local compressive stresses and cell extrusion in epithelial monolayers[276]. In the case of the intestinal villus, converging flows of migrating cells at the villus tip could possibly induce the formation of topological defects and instruct cell extrusion. However, whether topological defects are present at the intestinal villus tip and their implication in live or dead cell extrusion remains largely unexplored. Moreover, whether there is compression at the villus tip has not yet been formally tested.

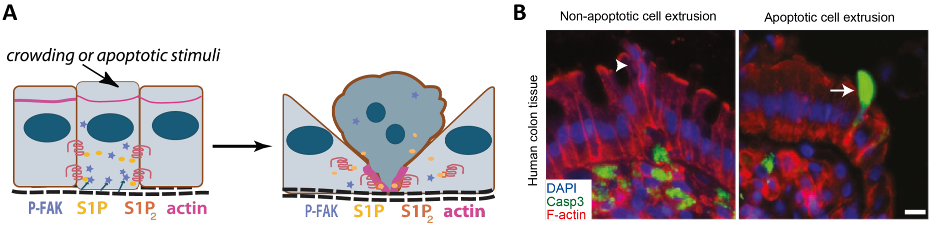
A
crowding or apoptotic stimuli
P-FAK
S1P
S1P2
actin
P-FAK
S1P
S1P2
actin
B
Non-apoptotic cell extrusion
Apoptotic cell extrusion
Human colon tissue
DAPI
Casp3
F-actin

Figure 26. Cell extrusion. **A)** Scheme depicting the process of epithelial cell extrusion. Both apoptotic and crowing signals induce the release of S1P by the extruding cells. S1P activate its receptors on the neighbor cells, triggering the formation of an actomyosin ring that expels the extruding cell out of the monolayer. Adapted from reference[268]. **B)** Immunostainings of Human colon tissue showing different modes of extrusion - non-apoptotic (activate caspase 3 negative, left) and apoptotic (active caspase 3 positive, right). Scale bar, 10 µm. Adapted from reference[67], with permission from Springer Nature.

2 Aims

2.1 General aim

The general aim of this thesis is to provide a quantitative understanding of the mechanical principles that govern crypt folding, crypt-villus compartmentalization and collective cell migration in mouse intestinal organoids.

2.2 Specific aims

To achieve the general aim above, the specific aims are:

1. To optimize an open-lumen intestinal organoid system compatible with accurate force measurements at high spatio-temporal resolution.
    - 1.1. To culture intestinal organoids over mechanically tunable polyacrylamide gels.
    - 1.2. To evaluate the physiological features of the optimized open-lumen intestinal organoids.

2. To study the mechanics of crypt folding and crypt-villus compartmentalization in open-lumen organoids.
    - 2.1. To measure 3D cell-ECM forces on the intestinal organoids via traction force microscopy.
    - 2.2. To unveil the force-generating mechanism driving crypt folding and crypt-villus compartmentalization.
    - 2.3. To assess the mechanical role of Eph/Ephrin signaling in crypt-villus compartmentalization.

3. To investigate the role of active Cell-Cell and Cell-ECM forces on collective cell migration from crypt to villus in open-lumen organoids.
    - 3.1. To quantitatively map cell velocities, cell-cell and cell-ECM forces during collective cell migration.

3 Materials and methods

3.1 Mice

mTmG[277], LifeAct–enhanced Green Fluorescent Protein (eGFP)[278] and myosin IIA–eGFP[279] mice were maintained at the laboratory of Danijela Matic Vignjevic (Institut Curie, France). Lgr5–eGFP-IRES-CreERT2[153] mice were maintained at the laboratory of Dr. Eduard Batlle (IRB Barcelona, Spain). EphB2$^{+/+}$ EphB3$^{+/+}$ mTmG (EphB2/3 WT) and EphB2$^{-/-}$ EphB3$^{-/-}$ mTmG (EphB2/3 dKO) mice were obtained through genetic crosses by mating EphB2$^{-/-}$ [280], EphB3$^{-/-}$ [281] and mTmG[277] mouse strains at the laboratory of Dr. Eduard Batlle (IRB Barcelona, Spain). Animal experimentation was approved by the Animal care and Use Committee of Barcelona Science Park (CEEA-PCB) and the Animal Welfare Body, Research Centre, Institut Curie. All procedures were carried out in compliance with the European Regulation for the Protection of Vertebrate Animals used for Experimental and other Scientific Purposes (Directive 2010/63).

3.2 Intestinal organoid culture

Organoid culture media composition

ENR medium was composed of DMEM/F-12 medium (Gibco, cat. no. 21331020) supplemented with 2% antibiotic-antimycotic (Gibco, cat. no. 15240062), 2.5% GlutaMAX (Gibco, cat. no. 35050038), 20 ng/ml mouse EGF (Peprotech, cat. no. 315-09), 100 ng/ml Noggin (Peprotech, cat. no. 250-38, or hNoggin), 500 ng/ml R-spondin1 (R&D Systems, cat. no. 3474-RS, or hR-spondin1), 10 ng/ml mouse FGF (Peprotech, cat. no. 450-33), 1×B-27 (Gibco, cat. no. 12587010) and 1×N-2 (Gibco, cat. no. 17502048).

ENRCV medium was prepared by supplementing ENR medium with 3 μM CHIR99021 (SelleckChem, cat. no. S2924) and 1 mM of Valproic acid (Sigma, cat. no. P4543).

Intestinal crypt isolation and organoid culture

Intestinal crypts from mTmG[277], LifeAct–eGFP[278] and myosin IIA–eGFP[279] mice were isolated as described elsewhere[207]. Briefly, the small intestine was isolated from 3 to 6 month-old mice and cleared of its inner materials with cleaning solution (2% (v/v) antibiotic–antimycotic (Gibco), 1% (v/v) gentamicin (Gibco) in cold sterile PBS). The intestine was cut longitudinally, divided into 3 cm-long pieces and incubated in the cleaning solution with constant shaking at 4 °C twice for 15 min. The clean tissue was chopped and incubated in 2 mM EDTA diluted in PBS for 30 min at 4 °C. The EDTA supernatant was then replaced by a cleaning solution and pipetted ten times with a 10 mL pipette to mechanically dissociate the intestinal tissue. This step was repeated four times, and each time the supernatant was replaced by a fresh cleaning solution. The last 2 supernatants were combined and centrifuged at 200×g for 3 min at 4°C. The pellet was resuspended in a resuspension solution (DMEM/F-12 medium (Gibco, cat. no. 21331020) supplemented with 2% antibiotic-antimycotic (Gibco, cat. no. 15240062), filtered through a 70 µm filter and centrifuged at 400×g for 6 min at 4°C. The pellet was suspended in Matrigel (Corning) half diluted in resuspension solution and plated in drops of 50 µL in 24 well plates. The Matrigel was allowed to polymerize for 30 min at 37 °C. After polymerization, the Matrigel drops were covered with 350 µL of ENR medium.

Intestinal crypts from Lgr5–eGFP-IRES-CreERT2[153], EphB2$^{+/+}$ EphB3$^{+/+}$ mTmG (EphB2/3 WT) and EphB2$^{-/-}$ EphB3$^{-/-}$ mTmG (EphB2/3 dKO) mice were isolated as follows:

The duodenum of mice from 2-4 months old was isolated, washed in PBS and cut longitudinally. Villi were mechanically removed with a scalpel. The tissue was then incubated in HBSS solution (Lonza, cat. no. BE10-547F) containing 8 mM EDTA (Invitrogen, cat. no. 15575020) for 5 min at room temperature (RT). After vigorous shaking, the liquid (mainly containing villi) was discarded and the tissue was reincubated with HBSS 8mM EDTA for 15 min on ice. After vigorous shaking, the solution was filtered through a 100-µm-pore cell strainer (Falcon, cat. no. 352360), obtaining the first crypt fraction. HBSS was added to the crypt fraction to dilute the EDTA and the solution was kept on ice. The tissue was incubated a second time with HBSS 8mM EDTA for 15 min on ice, vigorously shaken and filtered through a 100-µm-pore cell strainer to obtain a second crypt fraction. The first and second crypt fractions were mixed. The final solution containing the isolated crypts was centrifuged at 306×g for 5 min at 4ºC, and the pellet containing crypts was resuspended in Matrigel (diluted at 6mg/mL in ENR) and plated in drops of 50 µl in 24-well plates. After incubation for 30 min at 37 °C, the drops were covered with ENRCV medium (ENR for Lgr5–eGFP-

IRES-CreERT2[153]) supplemented with 10 µM Y-27632 (Tocris, cat. no. 1254). After the first splitting, organoids were grown without Y-27632.

For splitting, the organoid culture medium was aspirated and PBS supplemented with calcium and magnesium (Sigma-Aldrich, cat. no. D8662) and 2% antibiotic-antimycotic (Gibco, cat. no. 15240062) was added on top of the Matrigel domes. The domes were scratched with a serological pipette and transferred to a falcon tube. The organoid-containing solution was mechanically disaggregated by pipetting through a serological 10mL pipette with a 200 and 10 µL pipette tips plugged at the end. The solution was then centrifuged at 100g at RT for 3.5 min. The pellet was resuspended in Matrigel diluted in ENR and plated in 50 µL drops in 24 well plates. After polymerization of the drops for 30 minutes at 37°C, 350 µL of organoid culture medium* was added on top of the domes. Note: Throughout the process, to avoid organoid attachment to the plastic surfaces, all the plastic material (tubes, pipettes) were prewetted with PBS (Sigma-Aldrich, cat. no. D8662) containing 1% fetal bovine serum (FBS, Gibco, cat. no. 10270106).

*For mTmG[277], LifeAct–eGFP[278], myosin IIA–eGFP[279] and Lgr5–eGFP-IRES-CreERT2[153] the organoid medium was ENR and they were splitted every 3-4 days. For EphB2$^{+/+}$ EphB3$^{+/+}$ mTmG (EphB2/3 WT) and EphB2$^{-/-}$ EphB3$^{-/-}$ mTmG (EphB2/3 dKO) the organoid culture medium was ENRCV and they were splitted once a week (with a refreshment of the medium every 4-5days).

Organoid cryopreservation

Before cryopreservation, organoids were cultured for at least 4 days in ENRCV medium (with a media replacement every 2-3 days). The Matrigel domes were mechanically disaggregated in PBS (with calcium and magnesium) as explained above. In this case, however, the organoids were disaggregated into bigger pieces than for splitting, by only using pipette tips of 200µL (and not 10µL). The solution was then centrifuged at 100×g at RT for 3.5 min. The pellet was resuspended in Cryostor CS10 (STEMCELL technologies, cat. no. 7930) and aliquoted in cryotubes. The vials were frozen overnight at -80°C in an isopropanol bath (Mr. Frosty). The next day, the cryotubes were placed in liquid nitrogen for long term storage.

3.3 Polyacrylamide gel fabrication

Glass-bottom dishes (MatTek, cat. nos. P35G-0-20-C, P06G-0-20-F) were incubated for 10 min at RT with Bind-silane (Sigma-Aldrich, cat. no. M6514) diluted in absolute ethanol (PanReac, cat. no. 131086.1214) and acetic acid (Sigma-Aldrich, cat. no. 27225) at volume proportions of 1:12:1. After two washes with absolute ethanol, 22.5 µl of the PAA mix (see Table 1) were added on top of the glass and covered with an 18-mm coverslip (Paul Marienfeld, cat. no. 0111580). For the traction measurements, we used FluoSpheres with a diameter of 0.2 µm (Invitrogen, cat. no. F8807). For immunostainings where all fluorescent channels were needed, we used non-fluorescent CML latex beads with a diameter of 0.2 µm (Invitrogen, cat. no. C37480). After 1 h polymerization at RT, PBS was added, and the coverslips were removed with a scalpel.

Stiffness (kPa)	Acrylamyde %	Bis-acrylamide %	Beads % solids	APS %	TEMED %
0.2	3	0.03	0.04	0.05	0.05
0.7	4	0.03	0.04	0.05	0.05
1.5	5	0.04	0.04	0.05	0.2
5	7.46	0.044	0.04	0.05	0.05
15	7.5	0.16	0.04	0.05	0.05

Table 1. Polyacrylamide gel composition. A 500uL solution in PBS with the specified proportion of the different components was prepared. The reagents used were Acrylamyde (BioRad cat.no. 1610140), Bis-acrylamyde (BioRad, cat. no. 1610142), beads 0.2 µm (fluorescent or non-fluorescent, specified before), Ammonium persulfate (APS, Sigma, cat. no. A3678, stock prepared at 10% in MiliQ H_2O) and Tetramethylethylenediamine (TEMED; Sigma cat. no. T9281).

3.4 Polyacrylamide gel functionalization and ECM micropatterning

Organoid monolayers were confined in large circular ECM micropatterns (>900 µm). For this, the PAA gels were functionalized with 2 mg/ml Sulpho-SANPAH (Invitrogen, cat. no. 22589) irradiated for 7.5 min with ultraviolet light (365 nm) (Black Ray XX-15L UV bench lamp). The gels were then washed twice with 10 mM HEPES (Gibco, cat. no. H0887). For ECM micropatterning, polydimethylsiloxane (PDMS) stencils with circular openings were used[282]. The PDMS stencils were incubated with 2% pluronic acid F127 (Sigma-Aldrich, cat. no. P2443) in PBS for 1 h. They were then washed twice with PBS and allowed to dry at RT for 20 min. The stencils were carefully placed on top of the functionalized PAA gels. A solution of 250 µg/ml rat-tail type I Collagen (First Link UK, cat. no. 60-30-810) and 100 µg/ml Laminin 1 (Sigma-Aldrich, cat. no. L2020) dissolved in PBS was added on top of the PDMS stencils and incubated overnight at 4 °C. Finally, the ECM solution was aspirated, the gels were washed twice with PBS and the PDMS stencils were carefully removed.

3.5 Organoid seeding on PAA substrates

The 3D intestinal organoids were mechanically disaggregated by pipetting in PBS supplemented with calcium and magnesium (Sigma-Aldrich) and 2% antibiotic-antimycotic (Gibco). For one PAA gel, we seeded the number of organoids contained in one Matrigel drop of the 24-well plate. After disaggregation, the organoids were centrifuged at 100g for 3.5 min at RT and the pellet was resuspended in ENR medium. The organoids were seeded in a small volume (50 µl) on top of the ECM-coated PAA gels and incubated at 37ºC for 1h. After incubation, 550 µl ENR medium was added on top of the previous 50 µl. All experiments were performed 2–4 d after seeding.

For the seeding of EphB2$^{+/+}$ EphB3$^{+/+}$ (EphB2/3 WT) and EphB2$^{-/-}$ EphB3$^{-/-}$ (EphB2/3 dKO) organoids in polyacrylamide gels (Figure 48, Figure 49), the ENRCV medium was aspirated and 400 µL of TrypLE Express (Gibco, cat. no. 12604-013) supplemented with 10 µM Y-27632 (Tocris, cat. no. 1254) was added to each dome. The domes were broken by pipetting 5 times with a P1000 manual pipette. After 5 min incubation at 37ºC, the pipetting process was repeated. 400 µL of PBS with calcium and magnesium supplemented with 10 µM Y-27632 was then added to each well. The volume of all the wells was mixed in a falcon tube and the alive cell concentration was estimated via hemocytometer counting. 750000 alive cells per PAA gel were centrifuged at 200×g for 5 min at RT, resuspended in ENRCYV medium and seeded in a drop of 50 µL on top of the patterned area of the gel. After 2h incubation at 37ºC, 500 µL of wash medium (DMEM/F-12 supplemented with 2% antibiotic-antimycotic and 2.5% of GlutaMAX) was added on top of the drop, the dish was gently shacked, and the medium was aspirated. Finally, 500 µL of ENRCYV was added. One day after seeding, the medium was aspirated, the sample was washed with wash media and 500 µL of ENR was added. The next day, crypt-like regions were already visible.

3.6 Immunostaining

Open-lumen organoids immunostaining

The organoid monolayers were fixed in 4% paraformaldehyde (PFA; Electron Microscopy Sciences, cat. no. 15710-S) for 10 min at RT and washed three times with PBS. The samples were permeabilized with 0.1% Triton X-100 (Sigma-Aldrich, cat. no. T8787) in PBS for 10 min at RT. After three washes of 5 min at RT with PBS, the samples were blocked with PBS containing 10% FBS (Gibco, cat. no. 10270106) for 1 h at RT. Primary antibodies diluted blocking solution were added and incubated overnight at 4 °C. After five washes in PBS for 5 min at RT, secondary antibodies and phalloidin diluted in blocking buffer were added for 1 h at RT. Finally, the samples were washed five times for 5 min at RT with PBS and imaged in PBS.

For the immunostainings of EphB2$^{+/+}$ EphB3$^{+/+}$ mTmG (EphB2/3 WT) and EphB2$^{-/-}$ EphB3$^{-/-}$ mTmG (EphB2/3 dKO) organoid monolayers, the samples were fixed in 4% PFA (Electron Microscopy Sciences) in PBS for 10 min at RT and washed with PBS three times for 5 min at RT under mild rocking. The samples were then permeabilized with 1% Triton X-100 in PBS for 1h at RT and washed 3 times for 5 min at RT with 1X EnVision FLEX Wash Buffer (Agilent, cat. no. K800721-2). Next, the samples were blocked for 1h at RT with blocking buffer containing 10% Donkey serum (Jackson ImmunoResearch, cat. no. 017-000-121) and 0.5% Triton X-100 in PBS filtered with a 0.2µm-pore filter. Primary antibodies diluted in EnVision FLEX Antibody Diluent (Agilent, cat. no. K800621-2) were added and incubated for 24h at 4^{o}C. After 5 washes for 5 min at RT with 1X EnVision FLEX Wash Buffer, secondary antibodies diluted in EnVision FLEX Antibody Diluent were added and incubated for 24h at 4^{o}C. Finally, the samples were washed 5 times for 5 min at RT with 1X EnVision FLEX Wash Buffer and mounted in 40 µL of mounting media (Vectashield cat. no. H-1000). All steps from permeabilization were performed under mild rocking in a humidified chamber. Samples were stored at 4^{o}C until imaging.

Closed-lumen organoid immunostaining

For the image in Figure 14C, EphB2/3 WT organoids grown in ENR were fixed and immunostained following the protocol by O'Rourke et al. [283]. Briefly, the organoidss were fixed in 4% PFA-PME (50mM PIPES (Sigma-Aldrich, cat. no. P1851), 2.5 mM

MgCl2 (Sigma-Aldrich, cat. no. M8266), 5mM EDTA (Invitrogen, cat. no.15575-038)) for 20 minutes at RT. They were then washed once with IF Buffer (PBS, 0.2% Triton X-100 (Sigma-Aldrich, cat. no. T8787), 0.05% Tween 20 (Sigma, cat. no. P7949)), permeabilized in 0.5% Triton X-100 in PBS for 20 minutes at RT, washed once with IF Buffer and blocked in IF Buffer containing 1% BSA for 30 min at RT. The organoids were then incubated with primary antibodies diluted in blocking solution overnight at 4°C, washed 3 times (5 min each) with IF buffer at RT and incubated with the secondary antibodies diluted 1/400 in blocking solution. Finally, they were washed 3 times (5 min each) with IF buffer at RT and mounted in Vectashield H-1000.

In vivo tissue immunostaining

For the immunostaining of tissue slices, adult (3–6 months old) mT/mG[277] or myosin IIA–GFP[279] mice were euthanized to isolate the small intestine (jejunum). After gently flushing the gut lumen with PBS, the tissue was hand cut into fragments that were 0.5–1 cm in length with a scalpel and fixed in 4% PFA (Electron Microscopy Sciences) for 1 h at RT. The tissue was then rinsed with PBS and either hand cut with a scalpel into approximately 1-mm-thick slices or embedded in 4% wt/vol low-melting point agarose (Ultrapure, Thermo Fisher) and transversally sectioned on a vibratome (Leica VT1000) to obtain gut slices that were approximately 350 µm thick. The slices were permeabilized with 1% Triton X-100 (Sigma-Aldrich) in PBS for 1 h at RT. All antibody solutions and wash steps were performed using 0.2% Triton X-100 in PBS on a shaker, with mild rocking. Incubations with primary antibodies were performed overnight at RT and were followed by three washes of 1 h each. Secondary antibodies and DAPI were added with or without phalloidin—all of which were diluted 1:200 in 0.2% Triton X-100 in PBS—and incubated overnight at 4 °C. After the washes (as described above), the samples were mounted on slides using mounting agent (aqua-poly/mount; Polysciences) and left to cure overnight at RT in the dark.

For the whole-mount immunostaining in Figure 50, a portion of the proximal small intestine of EphB2$^{+/+}$ EphB3$^{+/+}$ mTmG (EphB2/3 WT) and EphB2$^{-/-}$ EphB3$^{-/-}$ mTmG (EphB2/3 dKO) mice was fixed in Formalin 10% (Sigma-Aldrich, cat. no. HT501128) overnight at 4ºC. Next, the tissue was washed 3 times in PBS for 2h at RT (each wash) and incubated in Ethanol 70% for 1h at RT. The Ethanol 70% was refreshed, and the tissue was stored at 4ºC in Ethanol 70%. Longitudinal slices of ~1mm were cut by hand with a scalpel from the samples stored in Ethanol 70%. The slices were rehydrated by sequential incubations in Ethanol 50%, 25% and PBS for 30 min each at RT. After that, the slices were permeabilized with 1% Triton X-100 (Sigma-Aldrich, cat. no. T8787) in PBS for 1 h at RT and blocked for 1h at RT with 3% Donkey serum (Jackson ImmunoResearch) 1% BSA (Sigma, cat. no. A9418) in PBS. Primary antibody was diluted 1/200 in 0.2% Triton X-100/PBS and incubated overnight at 4ºC. After 3 washes with 0.2% Triton X-100/PBS for 1h at RT (each wash), secondary antibodies diluted 1/200 in 0.2% Triton X-100/PBS were added and incubated overnight at 4ºC. Finally, the slices were washed 3 times with 0.2% Triton X-100/PBS for 1h at RT (each wash) and mounted in Fluorescent mounting medium (Agilent, cat. no. S302380-2). Samples were stored at 4ºC until imaging.

3.7 Antibodies

The primary antibodies used and their respective dilutions were: rabbit anti-Olfm4, 1/200 (Cell Signaling Technology, cat. no. 39141); mouse anti-CK20, 1/50 (Dako, cat. no. M7019); mouse anti-Ki67, 1/100 (BD Biosciences, cat. no. 550609); rabbit anti-lysozyme, 1/200 (*in vivo* and closed lumen organoids) and 1/1000 – 1/2000 (open-lumen organoids) (Dako, cat. no. A0099); rabbit anti-ZO-1, 1/200 (Thermo Fisher Scientific, cat. no. 40-2200); goat anti-EpHB2, 1/200 (R&D systems, cat. no. AF467) and mouse anti-GFP, 1/400 (Abcam, cat. no. ab1218).

The secondary antibodies used were: goat anti-mouse Alexa Fluor 488 (Thermo Fisher Scientific, cat. no. A-11029); donkey anti-rabbit Alexa Fluor 488 (Thermo Fisher Scientific, cat. no. A-21206), goat anti-rabbit Alexa Fluor 555 (Thermo Fisher Scientific, cat. no. A-21429), goat anti-mouse Alexa Fluor 405 (Abcam, cat. no. ab175660), donkey anti-mouse Alexa Fluor 647 (Thermo Fisher Scientific, cat. no. A31571). All the secondary antibodies were used at a dilution of 1/400 unless otherwise stated. To label F-actin, phalloidin Atto 488 (Sigma-Aldrich cat. no. 49409) or phalloidin-TRITC (Sigma-Aldrich, cat. no. P1951) was used at 1/500 and phalloidin Alexa Fluor-647 (Thermo Fisher Scientific, cat. no. A22287) at 1/400.

For the immunostaining of tissue slices, rat anti-E-cadherin (ECCD-2; Thermo Fisher Scientific, cat. no. 13-1900) was used at 1:100, DAPI (Sigma-Aldrich, cat. no. D9542) was used at 5 µg ml−1 and rhodamine–phalloidin (Thermo Fisher Scientific, cat. no. R415) was used at 1:200.

3.8 Image acquisition

For laser ablation, images were acquired using a laser-scanning confocal microscope (LSM880, Carl Zeiss) at a resolution of 512 × 512 pixels (pixel size = 0.2595 µm) with a bidirectional scan. A Plan-Apochromat ×40 objective (NA, 1.3; oil; DIC M27) was used. The microscope was equipped with temperature control (37 °C), and CO_2 and humidity control. The Zeiss ZEN software was used to carry out the acquisitions.

For immunostainings of tissue slices (Figure 45, Figure 46), images were acquired using a laser-scanning confocal microscope (LSM880, Carl Zeiss) at a resolution of 1,024 × 1,024 pixels (pixel size = 0.2076 µm) with a bidirectional scan and a Plan-Apochromat ×40 objective (NA, 1.3; oil; DIC M27) in Airyscan mode. Imaging and Airyscan processing were performed using the Zeiss ZEN software.

Images in Figure 14C Figure 48, Figure 49 and Figure 50 were acquired with a Nikon TiE inverted microscope with a spinning disk confocal unit (Dragonfly 200, Andor) and a sCMOS camera (Sona-4BV6U, Andor) using the commercial Fusion software (Andor). The microscope was equipped with a temperature box maintaining 37^{o}C in the microscope (Life Imaging Services). A ×20 objective (Nikon, S Plan Fluor NA 0.45 ELWD Ph1 ADM WD 8.2-6.9 dry) was used. A grid of z-stack tiles overlapping by 10% (Figure 50) or 20% (Figure 48, Figure 49) was acquired and stitched in the Fusion software.

For the timelapse in Figure 27B images were acquired with a ×20 objective (Nikon, S Plan Fluor NA 0.45 ELWD Ph1 ADM WD 8.2-6.9) in a Nikon TiE inverted microscope with an ORCA-Flash4.0-C11440-22CU CMOS camera, using MetaMorph (Universal Imaging) software. The microscope was equipped with a temperature box maintaining 37^{o}C in the microscope (Life Imaging Services) and a chamber maintaining CO_2 and humidity (Life Imaging services) was used.

The rest of the images were acquired using a Nikon TiE inverted microscope with a spinning disk confocal unit (CSU-WD, Yokogawa) and a Zyla-4.2-CL10 sCMOS camera (Andor). The microscope was equipped with a temperature box maintaining 37°C in the microscope (Life Imaging Services). For Figure 29A, a ×40 objective (Nikon, Plan fluor NA 0.75 OFN25 DIC M/N2 WD 0.66) was used. For Figure 42, (first row of images) a 2 × 2 stitching grid was acquired with a ×20 objective (Nikon, Plan Apo NA 0.75 Ph2 DM WD 1 dry). For the remaining images, a ×60 objective (Nikon, Plan Apo VC NA 1.2w WD 0.31-0.28 water immersion) was used. For the live imaging experiments, a chamber maintaining CO_2 and humidity (Life Imaging services) was used. The open-source Micromanager[284] was used to carry out multidimensional acquisitions with a custom-made script.

To image the monolayers on the 0.7 kPa gels (Figure 34, Figure 38, Figure 39), the gels were mounted upside down to improve the image quality. Briefly, the samples were fixed in 4% PFA for 10 min at RT. They were then mounted in PBS and sealed with nail polish before being flipped and imaged from the apical side.

3.9 Three-dimensional traction microscopy

The 3D tractions were computed as previously described[11]. Briefly, confocal stacks of the top layer of the fluorescent beads embedded in the PAA gels were imaged with a z-step of 0.2 μm both in the deformed (by the cells) and relaxed (trypsinized) states. From the stacks, the 3D deformations of the gel were computed with a homemade iterative 3D PIV software[11]. A window size of 64 × 64 pixels and an overlap of 0.75 was used. 3D tractions were then computed from the 3D deformations of the gel by solving the elastostatic equation in the Fourier space[11,285]. In the experiments involving a soft substrate condition, a Finite Element Method solution was implemented in ABAQUS to compute the 3D tractions from the 3D deformations of the gel for all the conditions[11].

3.10 Cell velocities

To characterize the cell kinematics in Figure 51, the velocity of the monolayer was computed by performing 3D PIV analysis on consecutive time-lapse images of organoid monolayers expressing membrane-targeted tdTomato (custom-made software; window size, 64 × 64 pixels; overlap, 0.75).

3.11 Radial averaging and kymographs

The boundary between the stem cell compartment and the transit amplifying zone was drawn by connecting the points where the normal traction component changed sign from negative to positive. If tractions were not available (as in immunostainings), the boundary was defined by the change in cell morphology (from columnar to elongated). For averaging (traction, velocity or image intensity), every pixel in the image was assigned the value of the distance to the closest point of the contour of the stem cell compartment. Spatio–temporal diagrams (kymographs) of a given variable were obtained by binning the values of that variable as a function of the (signed) distance from the boundary of the stem cell compartment and then computing the mean for each bin. For vectors, the normal to the contour was determined by fitting a parametric parabola to the nine pixels surrounding each pixel of the contour. To attribute a normal vector to each pixel of the image, we followed the approach of Trepat and colleagues[35]. Briefly, for each pixel of the image, we first assigned the normal vector of the closest pixel of the contour of the stem cell compartment. We then smoothed the curvature and normal vector components using a moving average filter whose characteristic length increased with the distance from the contour. To build spatio-temporal kymographs, the process of masking and radial averaging was repeated for every time point. Additional crypts in the field of view were excluded from the analysis.

In Figure 34H, the normal traction of the stem cell compartment was computed as the mean of the normal traction at the crypt center. The normal traction of the transit amplifying zone was computed as the peak in positive normal traction within the first 20 μm outside the stem cell compartment.

3.12 Averaging of crypt radial profiles

Crypts are variable in size within a certain range. As a consequence, directly averaging profiles of tractions, velocity or any other parameter of the study generates artefacts arising from the misalignment of compartments between different crypts. To avoid this, individual crypt profiles were linearly resized to the average crypt radius of the experimental group. The resized profiles were then averaged.

3.13 Blebbistatin treatment

For the blebbistatin dosage experiments (Figure 34A-C), organoid monolayers on 5 kPa gels were treated with DMSO (Sigma-Aldrich, cat. no. D8418) or (-)-blebbistatin (Sigma-Aldrich, cat. no. B0560) at 0.5, 1.5, 5 or 15 µM in ENR medium. The monolayers were imaged 3 h after the treatment.

In Figure 34F-H, Organoid monolayers on 5 kPa gels were imaged for 90 min in normal ENR medium (baseline). ENR medium containing blebbistatin was then added to a final concentration of 15 µM and the monolayers were imaged for 3 h. The medium was then aspirated, the sample was washed with ENR, and the monolayers were imaged for additional 11 h in normal ENR.

Monolayers on 0.7 kPa (Figure 34D, E and Figure 39B) or 15 kPa (Figure 40) gels were treated with 15 µM blebbistatin or DMSO in ENR medium for 3 h. They were then fixed in 4% PFA for 10 min at RT. Finally, they were washed twice with PBS and imaged as indicated earlier. The monolayers of Figure 40 were imaged without fixation. Crypt indentation (Figure 34E) was quantified in Fiji by tracing a vertical line from the bottom of the crypt to the bottom of the cells of the transit amplifying zone in a lateral view of the monolayer.

3.14 F-actin and myosin quantification

Given the heterogeneity in the height of the different compartments of the organoid monolayer, we developed the following algorithm to define the cell apical, medial and basal coordinates for every x-y position of the substrate. For the F-actin staining (phalloidin), each plane of the imaged z-stack was first binned (8 × 8 pixels). For each x-y position of the binned image along the substrate, the apical and basal coordinates were then defined as the coordinates of the apical-most and basal-most peaks in fluorescence intensity (phalloidin). The medial position was defined as the z coordinate equidistant to the apical and basal coordinate for each x-y pixel. We then extracted the fluorescence intensity of the apical, medial and basal positions. A similar approach was used to quantify myosin IIA, but the Volume Manager plugin (by R. Haase, MPI-CBG) was used to segment the monolayer. This last approach was also used for F-actin quantification on 0.7 kPa PAA gels (Figure 35B), as the high indentation of the crypts on these soft substrates prevented accurate automatic segmentation of the apical and basal surfaces. The radial distribution of the apical and basal F-actin signal from the crypt center was measured as explained in "Radial averaging and kymographs". For each crypt, apical and basal radial profiles were normalized by dividing both profiles by the mean apical F-actin signal in the first 5µm from the crypt center. Each profile was then linearly resized to the average crypt radius. The resized profiles were finally averaged.

To quantify the myosin intensity of the crypt and villus in the tissue immunostainings, small rectangular regions of interest (ROIs) of about 10 pixels in width were manually drawn around the apical and basal surfaces on the F-actin channel. The myosin IIA intensity was then averaged in the longitudinal axis of each ROI to quantify the intensity of the peak. Two ROIs were quantified and averaged per position. To correct for changes in absolute intensity at different tissue depths, the values for each crypt–villus image were normalized by dividing all values by the apical intensity of the crypt bottom. Measurements were performed only in the crypt–villus regions that fitted in approximately three image planes (1 µm step) to avoid differences in intensity due to light penetration through the tissue.

3.15 EphB2 receptor quantification

3D mean intensity projections of EphB2 immunostainings were generated and the radial distribution of the signal from the crypt center was measured as explained in "Radial averaging and kymographs". For each crypt, the radial profile of EphB2 signal was normalized by dividing for the maximum value of the profile and then linearly resized to the same average crypt radius of the basal actin distribution. The resized profiles were finally averaged.

3.16 Quantification of cell tilt *in vivo*

To quantify cell tilt *in vivo*, the cells were manually segmented in crypt images labelled with membrane-tdTomato or E-cadherin. An ellipse was fitted to each cell contour and cell orientation was defined as the angle of the ellipse long axis. The contour of the crypt was manually segmented and the normal direction to each pixel of the contour was calculated by fitting a parametric parabola to contour arcs of nine pixels (as described in the ‘Radial averaging and kymographs’ section). Cell tilt was defined as the angle difference between the normal to the crypt contour and the cell orientation. Tilt towards the crypt bottom was defined as positive. The tilt profiles obtained from each side of the crypt were averaged to generate one tilt profile per crypt. All crypt profiles were then rescaled to the average crypt contour length (in µm) and averaged.

3.17 De novo crypt formation

For the experiments in Figure 42, Organoids were cultured in ENR medium containing 10 µM CHIR99021 (SelleckChem, cat. no. S2924) and 10 mM nicotinamide (Sigma-Aldrich, cat. no. N0636). After 2 d, the organoids formed hyperproliferative spherical cysts devoid of crypts. For each PAA gel, we seeded the number of cysts contained in three Matrigel drops of a 24-well plate. The cysts were dissociated in TrypLE Express (Gibco, cat. no. 12604-013) at 37 °C for 5 min. Dissociation was mechanically assisted by pipetting and finally stopped by dilution in PBS supplemented with calcium and magnesium (Sigma-Aldrich). The cell suspension was then filtered through a cell strainer (40 µm diameter) to remove clumps of undissociated cells and centrifuged at 500g for 5 min at RT. The pellet was resuspended in ENR containing 10 µM CHIR99021, 10 mM nicotinamide and 10 µM Y-27632 (Merck Millipore, cat. no. 688001; ENR-CYN). The cells were seeded in a small volume (30 µl) on top of the micropatterned area of 5 kPa PAA gels. Functionalization and ECM micropatterning of the PAA gels was performed as described earlier using micropatterns of 700–900 µm in diameter. After incubation for 2 h at 37°C and 5% CO_2, the unattached cells were washed out with 200 µl ENR-CYN, and 600 µl ENR-CYN was added. The medium was changed to ENR the following day. The ENR medium was refreshed on the third day after seeding.

Monolayers were fixed in 4% PFA at different timepoints (1, 2, 3 and 4 d after seeding) and immunostained for Olfm4, CK20 and F-actin (phalloidin) as described earlier. Z-stacks of the whole circular patterns were acquired with a ×20 objective by stitching four fields of view in a 2 × 2 grid, with a 20% overlap. A maximum intensity projection of each channel was generated for each field of view. The maximum intensity projections were then fused in Fiji with the plugin ‘Grid/collection stitching’. Monolayers and Olfm4+ foci were manually segmented, and their area and intensity were measured. The density of the Olfm4+ foci was calculated as the ratio between the number of foci and the monolayer area. The CK20 intensity was measured in the segmented monolayer after excluding the Olfm4+ foci. The background for each channel was estimated at regions outside of the monolayer and subtracted. All analyses were performed in Fiji.

The apical and basal F-actin intensities were automatically extracted from z-stacks acquired with a ×60 objective following the same approach explained above. The apical and basal F-actin intensities were then averaged over a circular ROI with a radius of approximately 16 μm located at the center of the Olfm4+ area or at a random position in the Olfm4– area.

For traction measurements, stacks of the cells and beads were acquired at the four indicated time points. The 3D tractions were measured as explained earlier. Tractions normal to the substrate were averaged over a circular region with a radius of approximately 16 μm at the center of the developing crypts.

3.18 Quantification of the area of the stem cell niche, and number of stem and Paneth cells

Organoid monolayers seeded on PAA gels of varying stiffnesses were fixed and stained for F-actin (phalloidin) and Olfm4 as explained earlier.

The Olfm4+ area was manually segmented. Cells in the Olfm4+ area were manually counted in Fiji using the multipoint selection tool. Paneth cells were identified by their granular apical signal in bright-field and distinct apical actin signals. The number of stem cells was calculated by subtracting the number of Paneth cells from the total number of cells in the Olfm4+ area.

3.19 Laser cuts

Laser ablation was performed using a Ti:Sapphire laser (Mai Tai DeepSee, Spectra Physics) set at 800 nm with a laser power of 15% (500–750 mW). Circular regions for ablation were manually selected at the boundary between crypt compartments based on basal cell morphology. The cuts were performed in the medial plane of the monolayer.

To compute the recoil velocities, PIV was performed using a window size of 16 × 16 pixels and an overlap of 0.75. The velocity fields were resized to the original image size (512 × 512) using a bicubic interpolation to compute velocities relative to the ablated region. A peak in tissue velocity occurred within the first 2 s after ablation and thus recoil velocity was computed in this time frame.

The contour of the ablated region was used to compute the radial and tangential components of the recoil velocity as explained earlier. The radial velocities were averaged according to their distances to the ablated region. Crypt indentation before and after ablation was computed from the deformation of fluorescent beads embedded in the substrate as explained in the 'Three-dimensional traction microscopy' section.

3.20 Single-cell shape analysis

Image pre-processing

Spinning-disc images of intestinal organoid monolayers were pre-processed to address low signal-to-noise ratios and image scattering at the apical and basal cell surfaces—presumably due to rich apical excretion, brush microvillar border and scattering in the hydrogel underlying the organoid monolayers. To enable automatic detection of all single-cell surfaces, the signal-intensity values in dim regions of the apical and basal surfaces were computationally increased. Using Fiji[286], the monolayer apical and basal surfaces were defined in 3D, following the contour of the monolayer by manually adding sparse points in the x–z view and interpolating the surface between them, using the Volume Manager plugin (by R. Haase, MPI-CBG). Using a custom MATLAB script, image pixels lying on the capping surface with a fluorescence signal intensity higher than the 1st and lower than the 3rd quartile of the overall image intensity were set to the value of the 3rd quartile (4th quartile in the case of extremely bright lateral cell surfaces), resulting in segmentable apical and basal membrane signals in cells that displayed only clear lateral surfaces in the original images.

Cell segmentation

Pre-processed cell-membrane images were used for automatic cell segmentation in MorphographX[287]. The images were processed with Gaussian blurring (sigma, 0.3–0.5) and stack normalization (radius, 4–10; blur factor, 0.5–0.8). Segmentation was performed in whole image stacks in 3D using the Insight Toolkit watershed algorithm implemented in MorphographX (threshold, 800–1500). All segmentations required extensive manual correction for oversegmented, undersegmented and incomplete cells. Three-dimensional cell meshes were created (cube size, 2; smoothing, 1) from pixel label images for further shape analysis.

Shape analysis

Single-cell shape analysis was performed in 3D using custom-developed MATLAB tools. To account for the complex shape of the cells in the organoid monolayers, an apicobasal cell axis was constructed for each cell from the centroids of horizontal cell cross-sections in the central 70% of the cell body. The remaining 15% of the axis on each end was extrapolated as a straight line from the more stable central 70%. This 3D axis was used to calculate the 3D cell height and obtain new cross-sections normal to the cell axis. These cross-sections were analyzed for their area and various shape parameters, resulting in detailed apicobasal shape profiles for all cells. Cell tilt to the crypt center was defined as the angle of the straight end-to-end cell axis to the substrate normal (component in line with crypt center), and set as <0 if the axis was pointing away from the crypt center. Transit amplifying cells were defined as cells whose basal centroid lies within 14 µm of the manually outlined stem-cell niche border. Paneth cells were identified based on their distinct (granular) apical appearance in the corresponding bright-field images. All of the cells within the niche that were not Paneth cells were considered to be stem cells, in line with the Lgr5 and Olfm4 immunostaining results.

3.21 Quantification of the cell division rate

Maps of the spatial distribution divisions were manually obtained using Fiji multipoint selections. The coordinates of each cell division were imported to MATLAB. The mask of the stem cell compartment was used to compute the radial distance to the crypt center of each pixel of the field of view as explained earlier. The radius of the stem cell compartment was divided into three equal regions and the rest of the monolayer was divided into circular regions of 8,1 µm (75 pixels). For each region, we divided the total number of divisions by the area of the region and the time of observation to calculate the cell division rate.

3.22 Quantification of Paneth cell clustering and density

Open-lumen EphB2/3 WT or EphB2/3 dKO organoids grown on circular ECM patterns (700-900 µm diameter) were fixed 3 days after seeding and immunostained for Lysozyme. Z-stacks of the membrane-TdTomato and Lysozyme signals of the whole circular patterns were acquired with a ×20 objective by stitching multiple fields of view with a 20% overlap. The Lysozyme signal was used to segment Paneth cells in 3D with Cellpose 2.0 [288,289] in Python. The normalize99 function of Cellpose (it performs linear normalization of the signal between 0 and 1) was modified so that 0.0 is the 0.01st percentile of the signal and 1.0 is the 99.99th percentile of the signal. The parameters used in the segmentation were: gpu =false, model_type=cyto, diameter=35, channels=[0,0], net_avg=True, flow_threshold=0, cellprob_threshold=-3, stitch_threshold = 0.1, do_3D=False, min_size=-1). For each segmented Paneth cell, the XY coordinates of the 3D centroid was saved. Due to errors in the segmentation, the data was then manually corrected in Fiji[286] with the multipoint selection tool (the coordinates that did not correspond to Paneth cells were eliminated and new points at the center of non-segmented Paneth cells were added).

The area of each circular pattern was automatically detected in Fiji[286]. For that, a median filter of radius = 5 pixels was applied to a maximum intensity projection of the membrane signal and the image was then thresholded. The pattern mask was manually corrected if needed. Paneth cell density was then calculated by diving the number of detected Paneth cells (after correction) by the area of the circular pattern.

To measure the clustering level of Paneth cells, we used the Clarks and Evans (CE) index (index of aggregation of a spatial point pattern)[290]. CE of each pattern was calculated with the function clarkevans.test of the spatstat package[291] in R[292], defining the observation window as the segmented pattern contour. CE Values smaller than 1 indicate that the Paneth cells are clustered, CE values equal to 1 indicate that Paneth cells are randomly distributed within the pattern and CE values higher than 1 indicate that the cells are uniformly distributed within the pattern.

3.23 Quantification of Ki67 area

Open-lumen EphB2/3 WT or EphB2/3 dKO organoids grown on circular ECM patterns (700-900 µm diameter) were fixed 3 days after seeding and immunostained for Ki67. Z-stacks of the membrane-TdTomato and Ki67 signals of the whole circular patterns were acquired with a ×20 objective by stitching multiple fields of view with a 20% overlap.

The area of each circular pattern was automatically detected in Fiji[286]. For that, a median filter of radius = 5 pixels was applied to a maximum intensity projection of the membrane signal and the image was then thresholded. The pattern mask was manually corrected if needed. For each pattern, the area positive for Ki67 was detected by thresholding a maximum intensity projection of the Ki67 signal (same threshold value for all the patterns) in Python. Finally, the percentage of the total area of the pattern being Ki67-positive, was calculated as (area Ki67-positive / total area of the pattern) x 100.

3.24 Statistics and reproducibility

Traction maps, kymographs and laser cuts were plotted in MATLAB. The remaining plots were generated in GraphPad Prism 8. Immunostaing images and videos were processed with the open-source software Fiji and HandBrake. The data are represented as the mean ± error (s.e.m. or s.d.; as indicated in the figure captions). Normality of the data was checked and the statistical test used to compare the means was chosen accordingly, as indicated in the figure captions. No statistical method was used to predetermine the sample size, a minimum of n = 2 experiments with multiple measurements per experiment were performed. All the statistical analyses were performed in GraphPad Prism 8.

4 Results

4.1 Open-lumen intestinal organoids show functional crypt-like and villus-like domains

We seeded intestinal organoids over polyacrylamide gels (PAA) of 5kPA coated with Collagen I and laminin I (Figure 27A) Under these conditions, the organoids spread and formed confluent apico-basally polarized monolayers in few days (Figure 27B, C). These monolayers were heterogeneous in cell shape and density and showed compartmentalization of the different intestinal cell types.

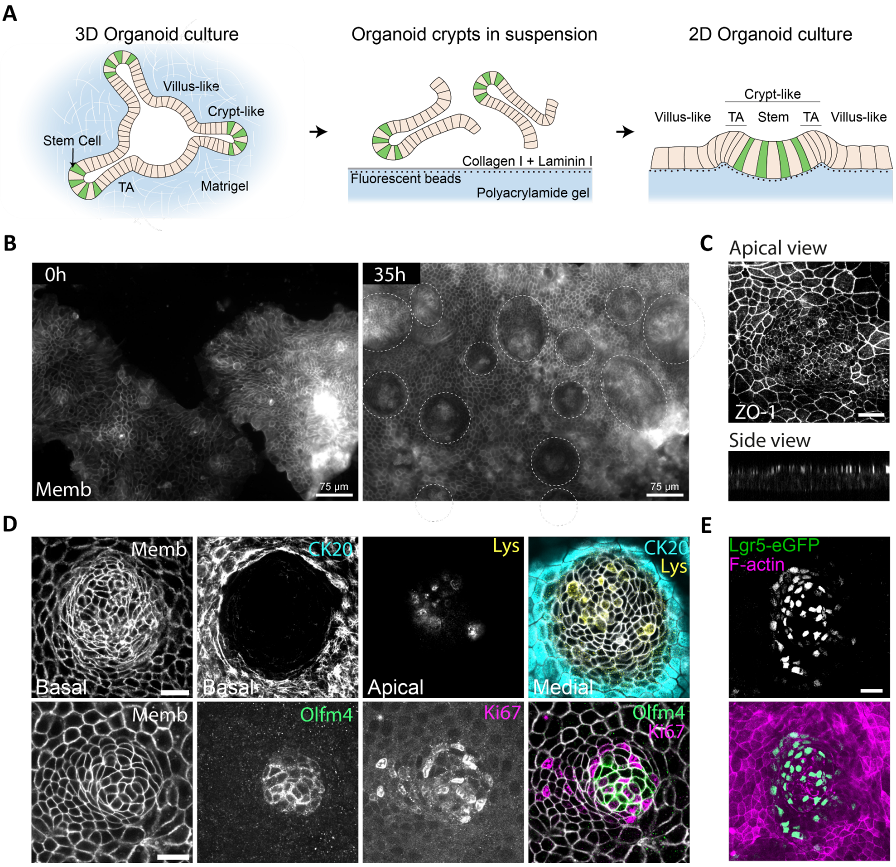
A
3D Organoid culture
Villus-like
Crypt-like
Stem Cell
TA
Matrigel
Organoid crypts in suspension
Collagen I + Laminin I
Fluorescent beads
Polyacrylamide gel
2D Organoid culture
Crypt-like
Villus-like
TA
Stem
TA
Villus-like
B
0h
Memb
75 µm
35h
75 µm
C
Apical view
ZO-1
Side view
D
Memb
Basal
CK20
Basal
Lys
Apical
CK20
Lys
Medial
Memb
Olfm4
Ki67
Olfm4
Ki67
E
Lgr5-eGFP
F-actin

Figure 27. Open-lumen intestinal organoids compartmentalize into crypt-like and villus-like domains. **A)** Scheme of the culture system. Closed-lumen organoids (3D organoids) grown in Matrigel are broken into small pieces and seeded on top of polyacrylamide gels coated with Collagen I and Laminin I, where they form open-lumen organoids (2D organoids). **B)** Live imaging of the organoid monolayers after seeding. As the monolayer gets confluent, two compartments are clearly visible: Circular dense foci (encircled with dashed line at 35h) are surrounded by regions of lower cell density

and higher cell area. Memb, membrane-targeted tdTomato. Scale bars, 75 µm. **C)** Organoids stained for the tight junction protein Zonula occludens-1 (ZO-1). Top: Average intensity projections of the 10 most basal apical planes of the monolayer. Bottom: lateral view of the monolayer. Scale bar, 20 µm. **D)** Organoids expressing membrane-targeted tdTomato (Memb, basal plane) stained for cytokeratin 20 (CK20, basal plane), lysozyme (Lys, apical plane), Olfm4 (basal plane) and Ki67 (basal plane). Scale bars, 20 µm. **E)** Organoids expressing Lgr5–eGFP-IRES-CreERT2 stained for GFP and F-actin (phalloidin). Scale bar, 20 µm. Stiffness of the PAA gel in all cases, 5 kPa.

Highly dense circular foci were composed of ISCs (positive for Olfm4 and Lgr5), Paneth cells (positive for Lysozyme) and proliferative cells (positive for Ki67), which were basally elongated at the edge of the foci (Figure 27D, E). These circular foci were surrounded by regions of lower density where cells increased their spreading area and expressed the differentiation marker Cytokeratin 20 (Figure 27D).

We next investigated whether the cells in each compartment retained their *in vivo* homeostatic functions. Time-lapse imaging showed that stem cells divided apically quite frequently (Figure 28A).

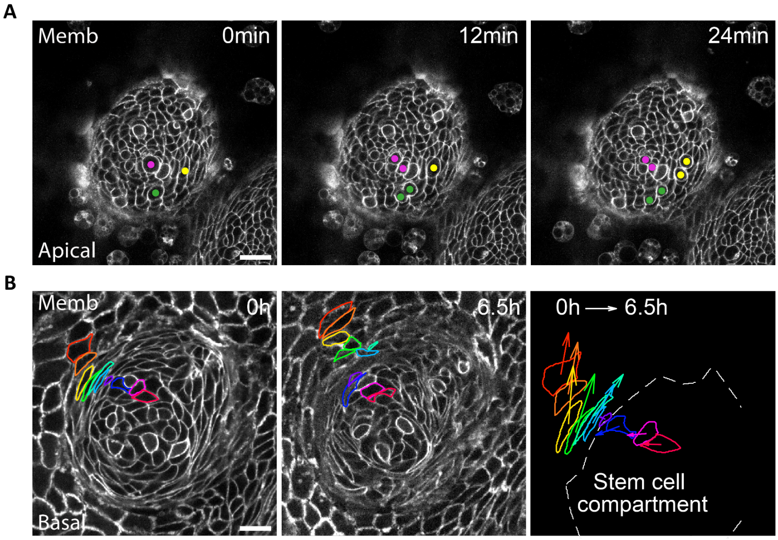

Figure 28. Live imaging of mitosis and migration in open-lumen organoids. **A)** Timelapse series of an apical plane of the organoids showing mitotic events in the circular dense foci. Three dividing cells (0 min) and its daughters after division (12, 24 min) are indicated with a dot of the same color (magenta, green or yellow). **B)** Displacement of representative cells over 6.5 h (left and middle). Each color labels

one cell. Note that one cell divided (green). Displacement vector of each cell (right). Stiffness of the PAA gels, 5kPa. Memb, membrane-targeted tdTomato. Scale bars, 20 µm.

Newly generated cells transitioned towards the differentiated region (Figure 28B), where they were extruded to the medium (Figure 29). Interestingly, following division at the boundary of the stem cell compartment, some daughter cells moved towards the center of the compartment, consistent with the idea that border cells can gain short-term self-renewal potential by changing their radial position within the niche[293,294] (Figure 30).

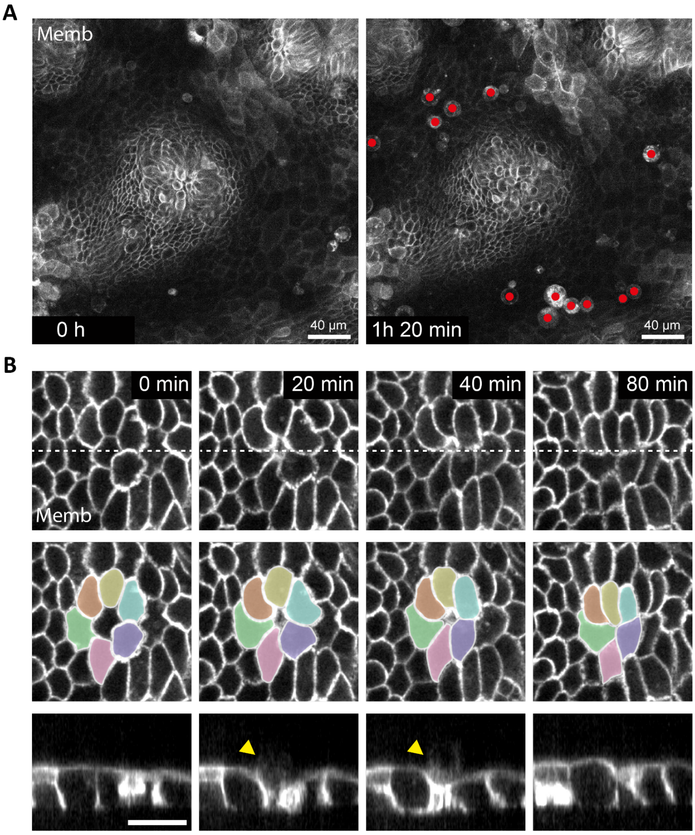

Figure 29. Live imaging of cell extrusion in open lumen organoids. **A)** Timelapse of an apical plane of the organoids showing extrusion events at the differentiated region. Extruding cells are indicated with a red dot at timepoint 1h 20 min**.** Scale bars, 40 µm. **B)** High magnification snapshots of an extrusion event happening at the differentiated region. The extruding cell is indicated with the arrowhead in the orthogonal views (bottom row). The neighbors of the extruding cell are highlighted in colors in the top

views of the monolayer (middle row). The lateral views correspond to the midplane indicated with a white dashed line at their corresponding top views (Top row). Scale bar, 20 µm**.** Memb, membrane-targeted tdTomato. Stiffness of all PAA gels, 5 kPa.

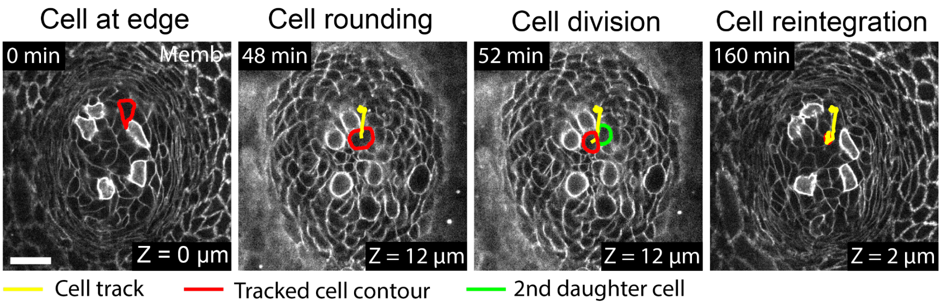
Cell at edge
Cell rounding
Cell division
Cell reintegration
0 min
Memb
48 min
52 min
160 min
Z = 0 µm
Z = 12 µm
Z = 12 µm
Z = 2 µm
Cell track
Tracked cell contour
2nd daughter cell

Figure 30. Retrograde movement of a cell toward the center of the stem cell niche. Snapshots of a cell that exhibits retrograde flow due to division. The contour of the cell of interest is delineated in red. The track of this cell is delineated in yellow. The contour of the second daughter cell that appears after the division event is delineated in green. The first and last snapshots (0 min and 160 min) correspond to basal planes of the crypt (Z = 0 µm and 2 µm, respectively). Because division occurs apically, the second and third snapshots (48 min and 52 min), correspond to an apical plane where division is better observed (Z = 12 µm). Scale bar, 20 µm**.** Memb, membrane-targeted tdTomato. Stiffness of the PAA gel, 5 kPa.

Given the analogy of the open-lumen organoid to the intestinal *in vivo* tissue, we adopted the following nomenclature: the region containing only stem and Paneth cells is called the stem cell compartment, the region containing highly proliferative elongated cells is called the transit amplifying zone and the region containing differentiated cells is called the villus-like domain.

4.2 Intestinal organoids are mechanically compartmentalized into functional domains

We used traction microscopy (Figure 31A) to map the three-dimensional (3D) traction forces that the organoids exerted on the underlying substrate (Figure 31B,C). Tractions were decomposed into a normal component (Tn, perpendicular to the substrate) and a radial component (Tr, parallel to the substrate and perpendicular to the crypt contour) (Figure 31D).

At the stem cell niche, normal tractions were negative, indicating that Stem and Paneth cells push the substrate downwards (Figure 31C, D). The magnitude of the normal forces decreased radially from the center of the crypt and became positive at the transit amplifying region (TA), indicating that cells at this region pull the substrate upwards (Figure 31C, D). After peaking at the transit amplifying zone, the normal tractions decreased in the villus-like domain, except in a few areas where the monolayer had delaminated to form pressurized domes[11] (Figure 31E).

The radial tractions were negligible at the crypt center and became increasingly negative (pointing towards the crypt center) at the crypt edge, peaking near the TA region (Figure 31D). Along the TA region, radial tractions decreased and became positive (pointing away from the crypt) at the villus-like region (Figure 31D).

These measurements reveal that the intestinal epithelium generates non-monotonic traction fields on the substrate, defining distinct mechanical compartments that colocalize with functional compartments; the stem cell compartment pushes downwards, the transit amplifying zone pulls upwards and the villus-like domain shears outwards.

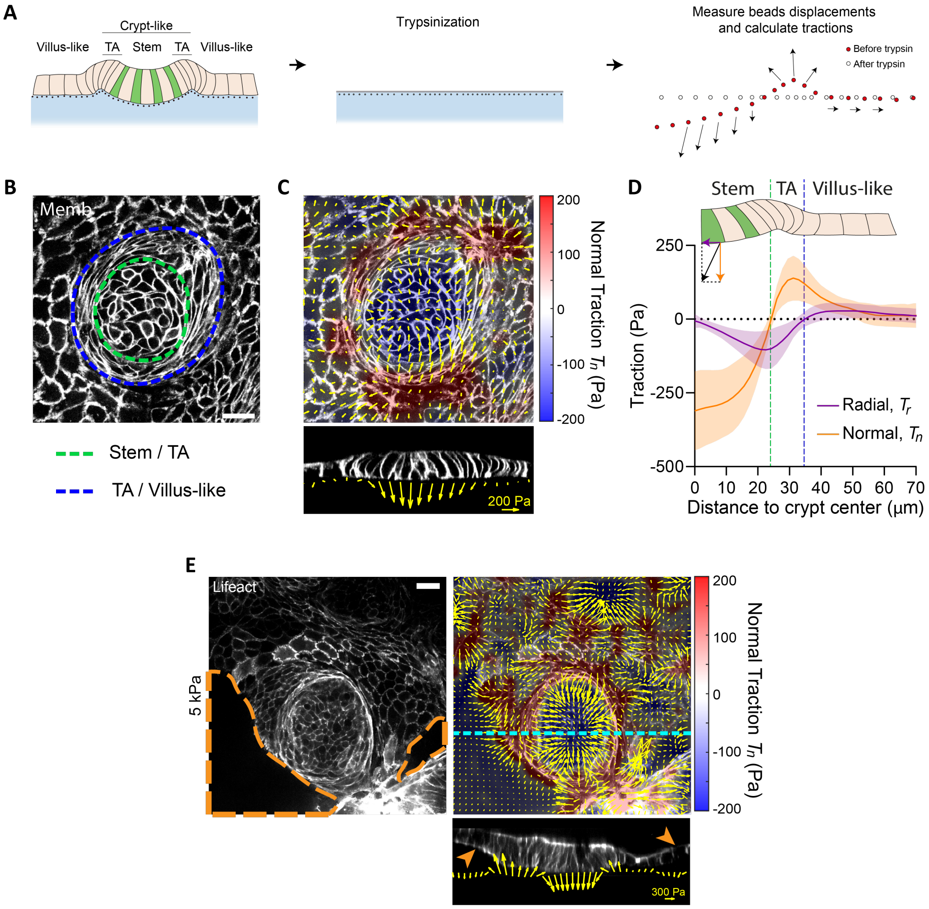

Figure 31. Open-lumen organoids are mechanically compartmentalized into functional domains. **A)** Traction Microscopy procedure (see methods). Briefly, the gel deformations caused by cell forces is calculated by measuring the displacement of fluorescent beads within the gel after trypsinizing the cells. Knowing the stiffness of the substrate, the forces needed to generate those deformations can be calculated. **B)** Illustration of the boundaries between the stem cell compartment and transit amplifying zone (green), and between the transit amplifying zone and villus-like domain (blue). **C) Top:** Three-dimensional traction map overlaid on a top view of an organoid. The yellow vectors represent components tangential to the substrate and the color map represents the component normal to the substrate. **Bottom**: Lateral view along the crypt horizontal midline. The yellow vectors represent tractions. Scale vector, 200 Pa. **D)** Circumferentially averaged normal and radial tractions as a function of the distance to the crypt center. The blue and green dashed lines indicate the radii where Tn and Tr, respectively, are zero, closely corresponding to the boundaries between the functional compartments in **d.** The Tr value at the villus is significantly different from zero (one-sample Wilcoxon test, $P < 0.0001$). Data are represented as the mean ± s.d. of n = 37 crypts from seven independent experiments. **E)** Spontaneous formation of pressurized domes in the villus-like domain. **Top left:** medial view of an organoid monolayer expressing Lifeact– eGFP. The dashed orange line defines the regions where the monolayer has delaminated to form a pressurized dome (orange arrowheads in bottom panel). **Top right:** 3D traction map of the same crypt. Yellow vectors represent components tangential to the substrate and the color map represents the component normal to the substrate. Horizontal cyan line indicates y-axis position of the lateral XZ view (bottom). **Bottom:** lateral view of the organoid monolayers. Yellow vectors represent tractions. Scale vector, 300 Pa. Scale bars, 20 µm**.** Memb, membrane-targeted tdTomato. Stiffness of all the PAA gels, 5 kPa. TA, transit amplifying zone.

4.3 Crypt size and folding depend on substrate stiffness

We next asked whether and how these mechanical forces control the shape and function of the crypt. The pattern of normal tractions (Figure 31C, D) suggests that the tissue is undergoing folding by pushing the stem cell compartment downwards. However, the monolayer remained quite flat (Figure 31C).

We reasoned that folding could be prevented because the substrate was too stiff. Thus, we tested whether a sufficiently soft substrate would enable the stem cell compartment to adopt the folded shape characteristic of 3D organoids and *in vivo* crypts. For that, we cultured intestinal organoids on substrates of varying stiffness (0.2, 0.7, 1.5, 5 and 15 kPa). On the stiffest substrates (15 kPa) the monolayer remained flat, and the crypts bulged out (Figure 32A). However, on progressively softer substrates, the crypts showed an increasingly pronounced folding (Figure 32A, B).

We then measured the cell tractions for each substrate stiffness except for the 0.2 kPa substrates, which displayed extreme deformations and hydrogel creasing instabilities that prevented an accurate calculation (Figure 32A). The radial traction component was strongly dependent on the substrate stiffness, whereas the normal component was not (Figure 32C, D). This observation prompted us to study whether the substrate stiffness influences epithelial compartmentalization. We found that the size of the stem cell compartment and the number of stem cells therein decreased as substrate stiffness increased (Figure 33A-C). By contrast, the ratio of stem to Paneth cells was insensitive to stiffness (Figure 33D). These experiments show that the mechanical microenvironment regulates intestinal homeostasis.

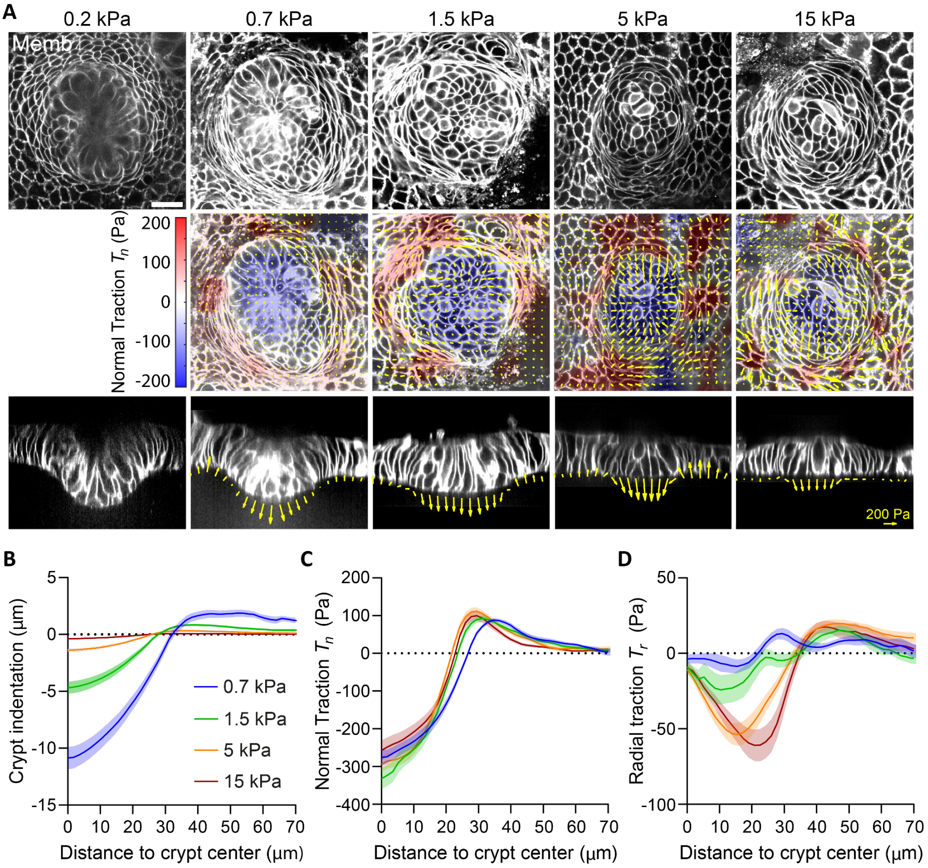

Figure 32. A stiffness-independent normal traction folds the crypt. **A)** Single confocal plane of representative crypts on substrates of increasing stiffness (top). Three-dimensional traction maps (center). The yellow vectors represent components tangential to the substrate and the color map represents the component normal to the substrate. Lateral view along the crypt midline (bottom). The yellow vectors represent tractions. Scale bar, 20 µm. Representative images of n = 14 (0.2 kPa), 23 (0.7 kPa), 23 (1.5 kPa), 37 (5 kPa) and 30 (15 kPa) crypts from 2, 3, 3, 7 and 4 independent experiments, respectively. **B-D**, Crypt indentation (**B**), normal traction (**C**) and radial traction (**D**) as a function of the distance to the crypt center for substrates of different stiffness. Data are represented as the mean ± s.e.m. of n = 23 (0.7 kPa), 23 (1.5 kPa), 37 (5 kPa) and 30 (15 kPa) for **B**, and n = 14 (0.7 kPa), 12 (1.5 kPa), 36 (5 kPa) and 30 (15 kPa) crypts for **C,D** from 3, 3, 7 and 4 independent experiments, respectively. Memb, Membrane-targeted tdTomato.

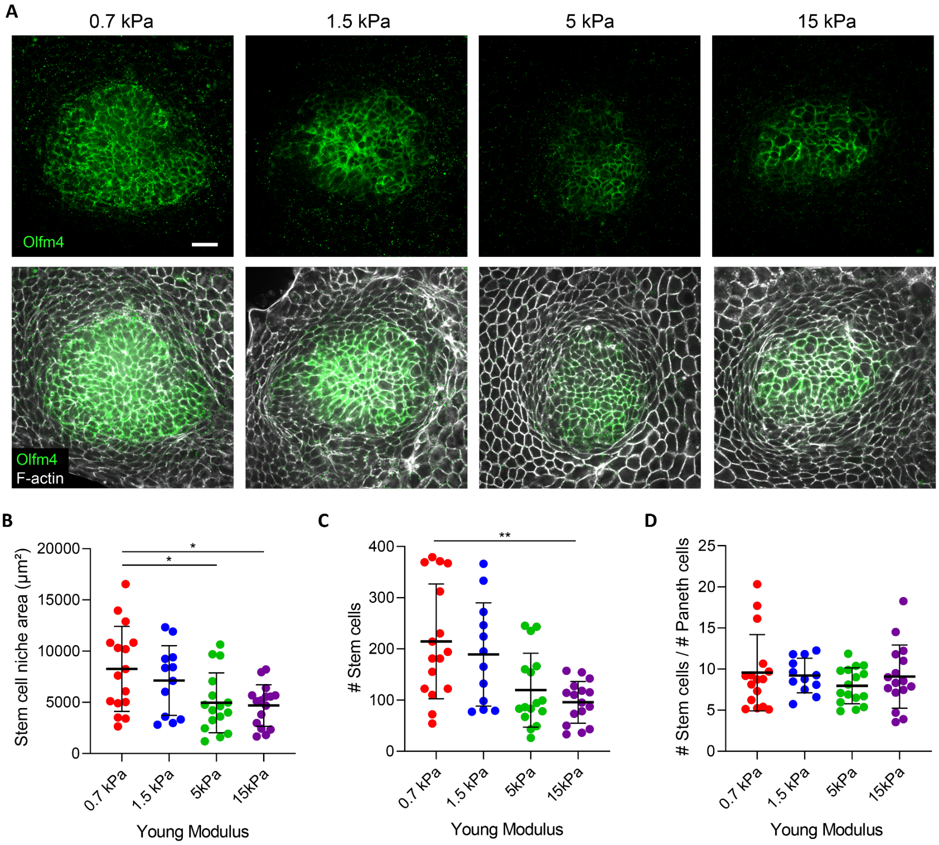

Figure 33. The size of the stem cell compartment decreases with substrate rigidity. **A)** Olfm4 and F-actin (phalloidin) immunostaining of organoids grown on substrates of increasing stiffness. Due to pronounced crypt folding, for visualization purposes, the image for 0.7 kPa is a projection along the crypt medial plane. Representative images of three independent experiments. Scale bar, 20 µm. **B-D)** Area of the stem cell compartment (**B**), number of stem cells (**C**) and ratio between the number of stem and Paneth cells (**D**) for substrates of increasing stiffness. n = 16 (0.7, 5 and 15 kPa) and 12 (1.5 kPa) crypts from three independent experiments. Statistical significance was determined using a one-way analysis of variance, followed by a Tukey's multiple-comparison test (**B**), and a Kruskal–Wallis test, followed by a Dunn's multiple-comparison test (**C,D**). Only statistically different pairwise comparisons are indicated. **B)** P = 0.0305 (0.7 versus 5 kPa) and 0.0157 (0.7 versus 15 kPa). **C)** P = 0.0071 (0.7 versus 15 kPa). *P < 0.05 and **P < 0.01.

4.4 The crypt folds through apical constriction

We reasoned that the observed traction patterns and monolayer geometry could be generated by different mechanisms. The confined proliferation at the crypt may generate a compressive force (mitotic pressure) that pushes the stem cell compartment towards the substrate, inducing buckling of the tissue. Alternatively, contractility of the epithelium via the actomyosin machinery could be responsible of crypt folding by compressive buckling of the crypt or bending through apical constriction.

To test whether the tractions and folding of the crypt were generated by buckling instabilities due to proliferation or by actomyosin contractility, we treated the organoids with blebbistatin, an inhibitor of myosin II contractility. Following the addition of increasing doses (0.5–15 μM) of blebbistatin, the traction forces were progressively impaired and the monolayer flattened gradually (Figure 34A, B, C). All traction forces vanished at a dose of 15 μM (Figure 34A, C, F) and the crypt indentation was negligible (Figure 34B, D, E). The elongated shape of the basal cell surface at the transit amplifying zone, which was unaffected by the stiffness of the gel, was largely lost by this treatment (Figure 34A, F). When blebbistatin was washed out, the traction patterns re-emerged, the elongated morphology was recovered and the monolayer refolded (Figure 34F, G, H). Remarkably, the crypt size decreased after recovering from blebbistatin, further emphasizing a mechanical control of intestinal homeostasis (Figure 34F, G). Taken together, these results show that crypt folding and tractions are not generated by a buckling instability under mitotic pressure, but from actomyosin-driven contraction of the epithelium.

To study how the actomyosin cytoskeleton drives crypt folding, we measured the distribution of actin and myosin across organoid monolayers seeded on stiff (5 kPa) and soft (0.7 kPa) substrates. Irrespective of the substrate stiffness, F-actin staining (phalloidin) and live imaging of organoids expressing myosin IIA–eGFP revealed an actomyosin accumulation at the apical surface of the stem cell compartment (Figure 35, Figure 36). In addition, they showed a basal ring of circumferential stress fibers under the elongated cells at the transit amplifying zone (Figure 35, Figure 36).

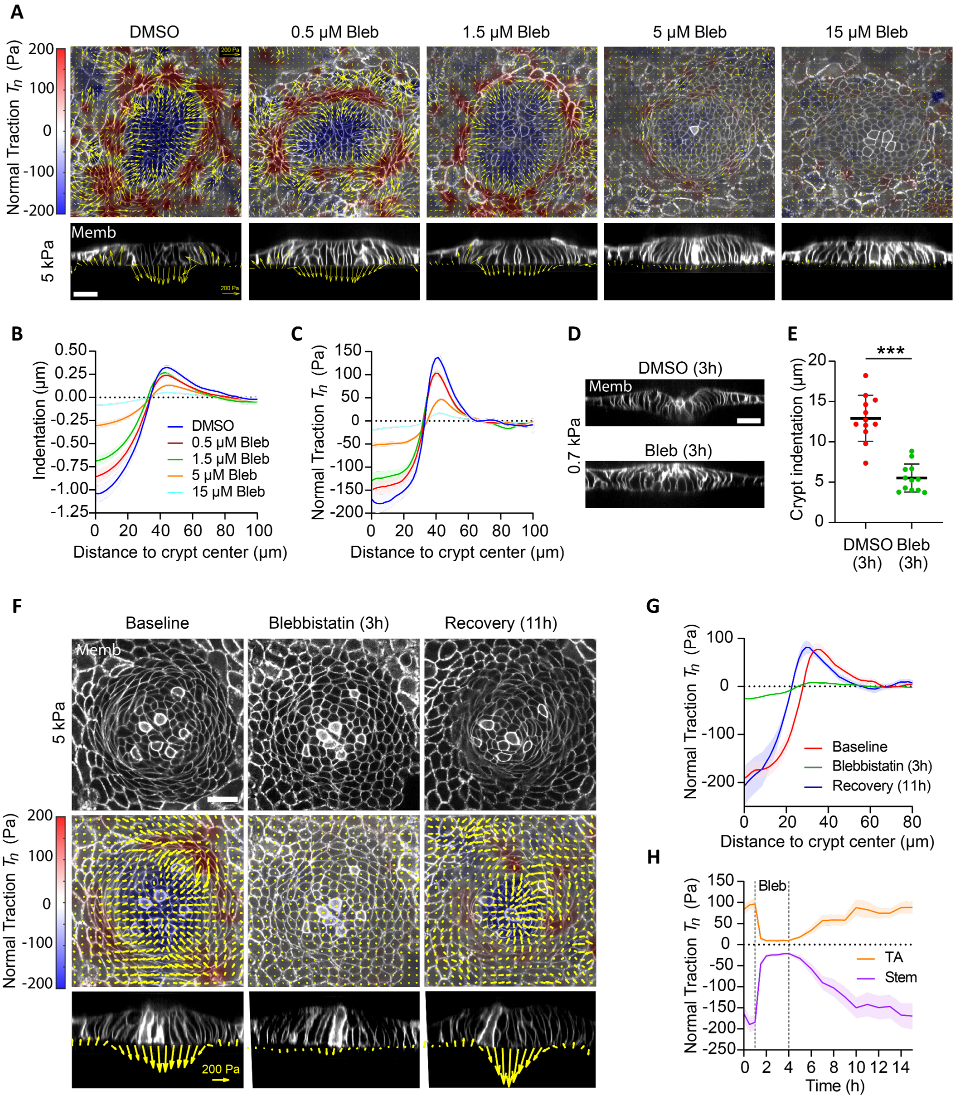

Figure 34. Crypt tractions and folding are actively generated through myosin contractility. **A) Top row**: 3D tractions of the crypts treated with the indicated concentration of blebbistatin (Bleb). Yellow vectors represent components tangential to the substrate and the color map represents the component normal to the substrate. **Bottom row**: lateral views of the organoids along the crypt midline. Yellow vectors represent tractions. Scale vector, 200Pa. **B-C**) Crypt indentation (**B**), and normal traction (**C**) as a function of the distance to the crypt center for crypts treated with the indicated concentrations of blebbistatin for 3 hours. Data are represented as mean ± s.e.m of n=18 (DMSO), 24 (0.5 µM), 19 (1.5 µM) 22 (5 µM) and 20 (15 µM) crypts from 3 independent experiments. **D)** Lateral views of crypts seeded on 0.7 kPa gels and treated with dimethylsulfoxide (top) or 15 µM

blebbistatin (bottom) for 3 h. **E)** Indentation at the center of the crypt in cells treated with dimethylsulfoxide or blebbistatin for 3 h. P < 0.0001, two-tailed unpaired Student's t-test; n = 12 crypts from two independent experiments. **F)** Traction maps under baseline conditions (left), after 3 h of blebbistatin treatment (center) and after 11 h of blebbistatin washout (right) on 5 kPa substrates. Membrane-targeted tdTomato (medial plane; top). Three-dimensional traction maps (center). The yellow vectors represent components tangential to the substrate; the color map represents the component normal to the substrate. Lateral view along the crypt midline (bottom). Representative images of three independent experiments. **G)** Normal traction as a function of the distance to the crypt center before, during and after blebbistatin treatment. **H)** Time evolution of normal traction for the stem cell compartment and transit amplifying zone (TA) before, during and after blebbistatin treatment. Scale bars, 20 µm. Memb, Membrane-targeted tdTomato; DMSO, dimethylsulfoxide; bleb, blebbistatin; a.u., arbitrary units. PAA Stiffness in A-B and F-H = 5 kPa, and D-E = 0.7kPa.***P < 0.001

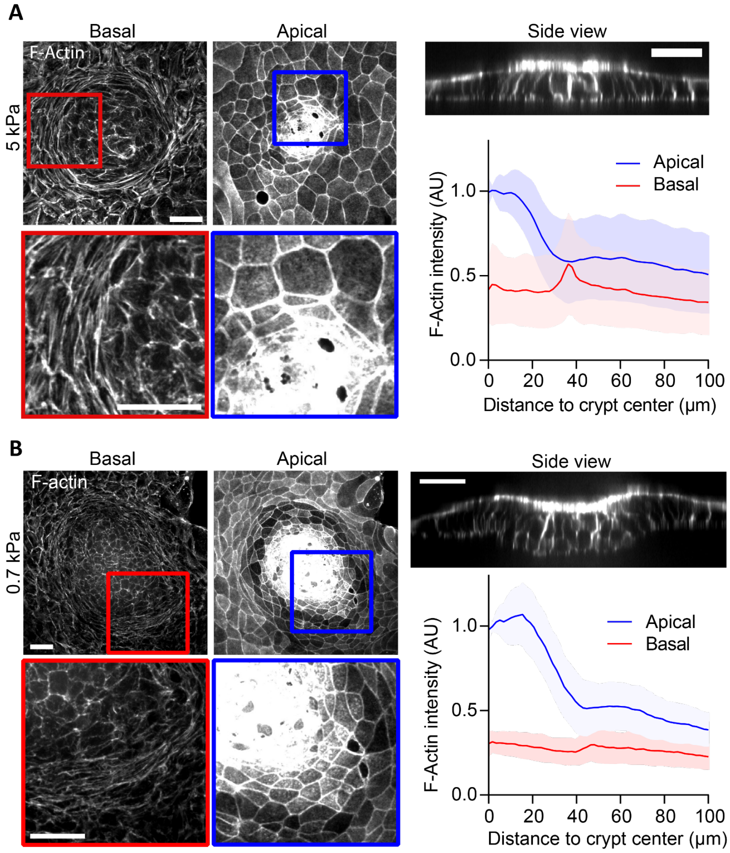
A
Basal
Apical
Side view
F-Actin
5 kPa
Apical
Basal
F-Actin intensity (AU)
1.0
0.5
0.0
0
20
40
60
80
100
Distance to crypt center (µm)
B
Basal
Apical
Side view
F-actin
0.7 kPa
Apical
Basal
F-Actin intensity (AU)
1.0
0.5
0.0
0
20
40
60
80
100
Distance to crypt center (µm)

Figure 35. F- Actin shows a similar distribution in soft and stiff gels. **A-B)** F-actin (phalloidin) staining of crypts on 5 kPa gels (**A**) and 0.7kPa gels (**B**). Projections of basal (left) and apical (center) F-actin of a representative crypt. Lateral view of the same crypt (top right). Radial distribution of the apical and basal F-actin intensity as a function of the distance to the crypt center (bottom right). n = 36 crypts

from 4 independent experiments (**A**) and n = 12 crypts from 3 independent experiments (**B**). Data are represented as mean ± s.d. All scale bars, 20 µm.

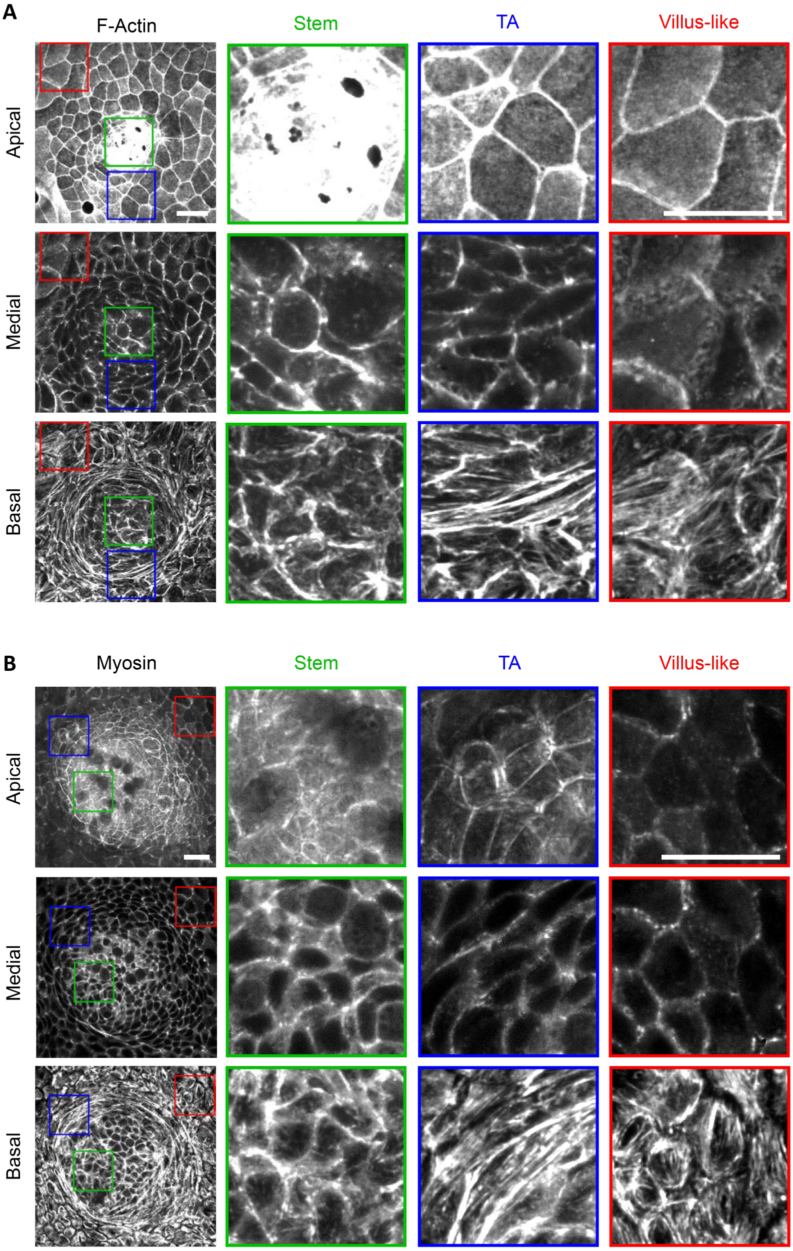
A
F-Actin
Stem
TA
Villus-like
Apical
Medial
Basal
B
Myosin
Stem
TA
Villus-like
Apical
Medial
Basal

Figure 36. Actomyosin distribution in open-lumen organoids. **A-B)**, Apical, medial and basal projections of F-Actin (Phalloidin, **A**) and myosin IIA-eGFP (**B**). The stem cell compartment (Stem), the

Transit amplifying zone (TA) and the villus-like domain (villus-like) are zoomed in the regions of the monolayer indicated with the respective colors. Scale bars, 20 µm. Stiffness of the gels, 5kPa.

This actomyosin distribution suggests two potential mechanisms that are not mutually exclusive. The first is that myosin differentials across the apicobasal cell axis drive monolayer bending through apical constriction. The second is that supracellular contraction of the transit amplifying zone compresses the stem cell compartment radially to induce its buckling. To assess the contribution of bending versus buckling, we reasoned that both mechanisms involve cell–cell stresses of opposite sign. In the bending scenario, cells in the stem cell compartment should pull on each other differentially along the apicobasal axis to indent the substrate, thereby generating an apical tensile stress. By contrast, in the buckling scenario, cells in the stem cell compartment should push on each other as a result of the compressive stress generated by the contractile ring at the transit amplifying zone.

To measure the sign of the stress field, we performed circular laser ablations along the internal and external boundaries of the transit amplifying zone. In both cases ablations induced a radial recoil on both sides of the cuts (Figure 37A-E). The recoils were asymmetrical and showed non-monotonic velocity fields, suggesting that monolayer friction and viscosity follow a complex spatial distribution that prevents a straightforward readout of the relative tensions from recoil dynamics (Figure 37B, D, E). However, the fact that monolayers recoiled on both sides of the cuts implies that the crypt is under tension. Moreover, after cutting the monolayer at the inner boundary of the transit amplifying zone, the stem cell compartment increased its indentation of the substrate (Figure 37F).

This set of experiments rules out compressive buckling driven by myosin differentials between crypt compartments or by mitotic pressure. It instead shows that the stem cell compartment bends by apical constriction.

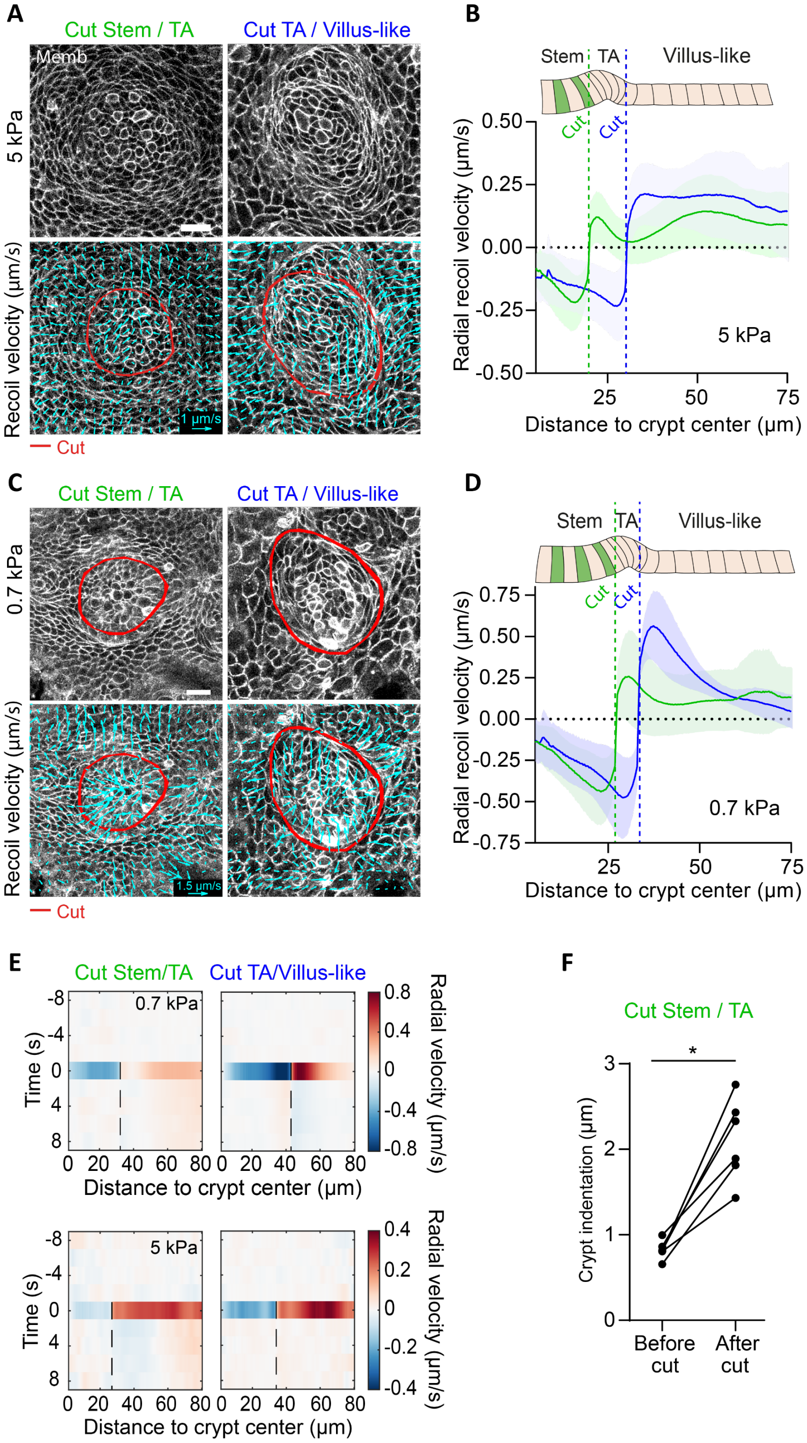
A
Cut Stem / TA
Cut TA / Villus-like
Memb
5 kPa
Recoil velocity (µm/s)
1 µm/s
Cut
B
Stem
TA
Villus-like
Cut
Cut
0.50
0.25
0.00
-0.25
-0.50
Radial recoil velocity (µm/s)
5 kPa
25
50
75
Distance to crypt center (µm)
C
Cut Stem / TA
Cut TA / Villus-like
0.7 kPa
Recoil velocity (µm/s)
1.5 µm/s
Cut
D
Stem
TA
Villus-like
Cut
Cut
0.75
0.50
0.25
0.00
-0.25
-0.50
-0.75
Radial recoil velocity (µm/s)
0.7 kPa
25
50
75
Distance to crypt center (µm)
E
Cut Stem/TA
Cut TA/Villus-like
0.7 kPa
Time (s)
-8
-4
0
4
8
0 20 40 60 80
Distance to crypt center (µm)
0.8
0.4
0
-0.4
-0.8
Radial velocity (µm/s)
5 kPa
Time (s)
-8
-4
0
4
8
0 20 40 60 80
Distance to crypt center (µm)
0.4
0.2
0
-0.2
-0.4
Radial velocity (µm/s)
F
Cut Stem / TA
*
Crypt indentation (µm)
3
2
1
0
Before cut
After cut

Figure 37. Circumferential laser cuts show that crypts are under tension. **A, C)** Recoil-velocity maps immediately after ablation along the red lines of two crypts on 5 kPa (**A**) or 0.7 kPa substrates (**B**) substrates (bottom). Cut inside the transit amplifying zone (left). Cut outside the transit amplifying zone (right). The two crypts before ablation (top). Scale vector 1 µm/s (**A**) or 1.5 µm/s (**C**). **B,D)** Radial recoil velocity as a function of the distance to the crypt center for cuts between the stem cell compartment and transit amplifying zone (green), and the transit amplifying zone and villus-like domain (blue) in 5kPa (**B**) or 0.7kPa (**D**) substrates. Data are represented as mean ± s.d. n = 14 (cut stem / TA) and 11 (cut TA / villus-like) crypts from 5 independent experiments (**B**); n= 14 (cut Stem / TA) and 10 (cut TA / Villus-like) crypts from 3 independent experiments (**D**). **E)** Representative kymographs of circumferentially averaged radial velocity as a function of the distance to the crypt center on 0.7 kPa (Top) and 5 kPa (bottom) substrates. Left: cut inside TA; right: Cut outside TA. The dashed black line indicates the time and position of the cut. Negative velocities point towards crypt center. **F)** Indentation at the center of the crypt before and after cutting between the stem cell compartment and the transit amplifying zone. P = 0.0313, two-tailed Wilcoxon paired test; n = 6 crypts from two independent experiments. All scale bars, 20 µm; Memb, Membrane-targeted tdTomato; TA, transit amplifying zone.

4.5 The actomyosin cortex determines cell shape and traction

We next investigated how cell shape evolves between compartments. To this aim, we segmented individual cell shapes in crypts grown on stiff (15 kPa) and soft (0.7 kPa) substrates (Figure 38A; Figure 39A,B). The cell shapes were heterogeneous (Figure 38A) but averages over all cells and crypts revealed consistent morphometric patterns. The apical area of the stem cells on both the stiff and soft substrates was smaller than the basal area (Figure 38B; Figure 39E,F). Paneth cells showed the opposite behavior (Figure 38D), indicating that stem, but not Paneth, cells drive apical constriction of the stem cell compartment. Both cell types were taller than differentiated cells (Figure 39G) and displayed an apicobasal tilt towards the center of the crypt, which peaked at the boundary between the stem cell compartment and the transit amplifying zone (Figure 38D; Figure 39H). On reaching this boundary, the differences between the apical and basal area vanished (Figure 39E,F) and the cells became basally elongated along the circumferential direction (Figure 38C,D ; Figure 39I). Treatment with blebbistatin for 3 h reduced the tilt at the stem cell compartment and the basal aspect ratio of every cell type at the crypt (Figure 40).

To investigate the link between tissue shape, cell shape, cell–ECM tractions and actomyosin localization, we developed a 3D vertex model[295–297] of the crypt coupled to a soft hyperelastic substrate (Appendix 1). We considered a uniform flat monolayer with a pattern of cell surface tensions as suggested by the measured distribution of cortical components (Figure 35; Figure 36). Specifically, we prescribed apical and basal surface tensions with a profile following the measured F-actin density (Figure 35 and Appendix 1). We then allowed the monolayer to equilibrate its shape while adhering to the substrate. The model was able to recapitulate all morphological features of the monolayer - both at the cell and tissue scales - including cell height, shape and monolayer folding, for both soft and stiff substrates (Figure 39C,D).

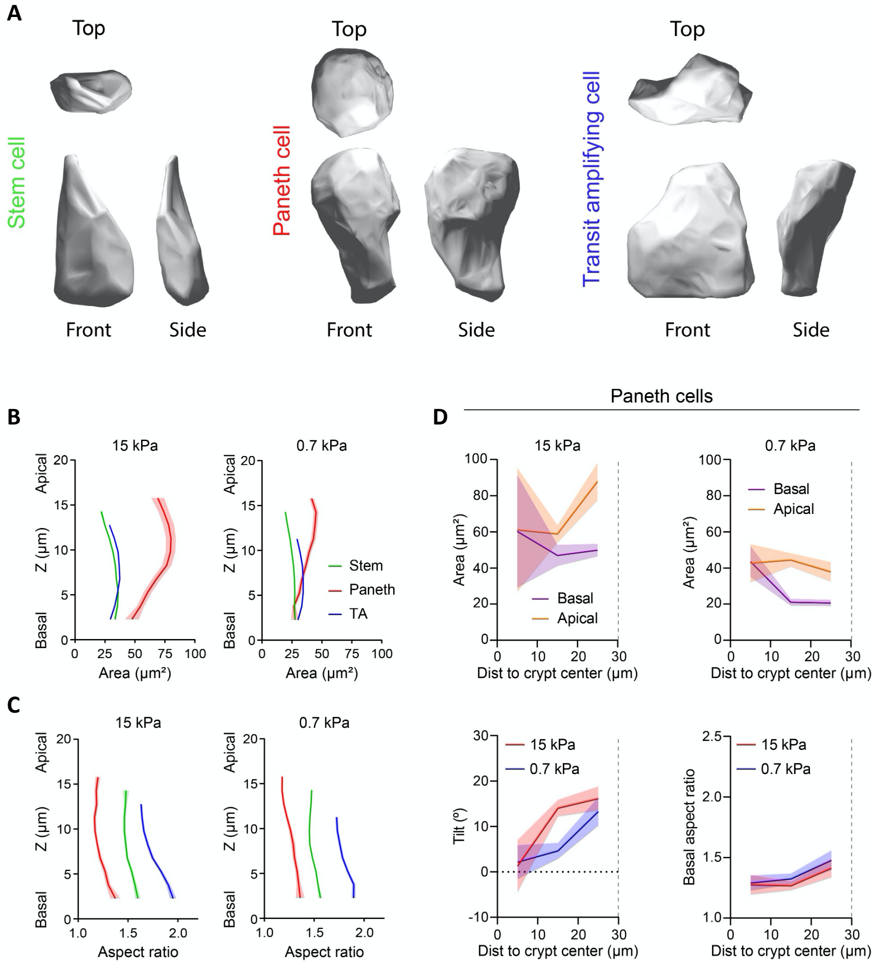

Figure 38. Morphometric analysis of the different cell types in the crypt. **A**) Top, front and side 3D renders of a segmented stem cell (left), Paneth cell (center) and transit amplifying cell (right). **B-C)** Cell area (**B**) and aspect ratio (**C**) along the apicobasal axis of stem (green), Paneth (red) and TA (blue) cells on rigid (left, 15 kPa) and soft (right, 0.7 kPa) gels. n = 190 (stem cells), n = 21 (Paneth cells); n = 218 (transit amplifying cells) for 15 kPa gels. n = 596 (stem cells); n = 52 (Paneth cells); n = 301 (transit amplifying cells) for 0.7 kPa gels. n = 3 crypts per stiffness from 2 (0.7 kPa) and 3 (15kPa) independent experiments. Data are represented as mean ± s.e.m. **D**) **Top:** Apical and basal area of Paneth cells as a function of the distance to the crypt center on stiff (left, 15 kPa) and soft (right, 0.7 kPa) substrates. The boundary between the stem cell compartment and the transit amplifying zone is indicated in all the plots with a dashed vertical line. **Bottom:** Apicobasal tilt (left) and basal aspect ratio (right) of Paneth cells as a function of the distance to the crypt center on stiff (red, 15 kPa) and soft (blue, 0.7 kPa) substrates. n = 3 crypts per stiffness from 2 (0.7 kPa) and 3 (15kPa) independent experiments. From center to edge bins, n = 3, 7 and 10 cells for 15 kPa gels and n = 11, 25 and 15 cells for 0.7 kPa gels. Data are represented as mean ± s.e.m.

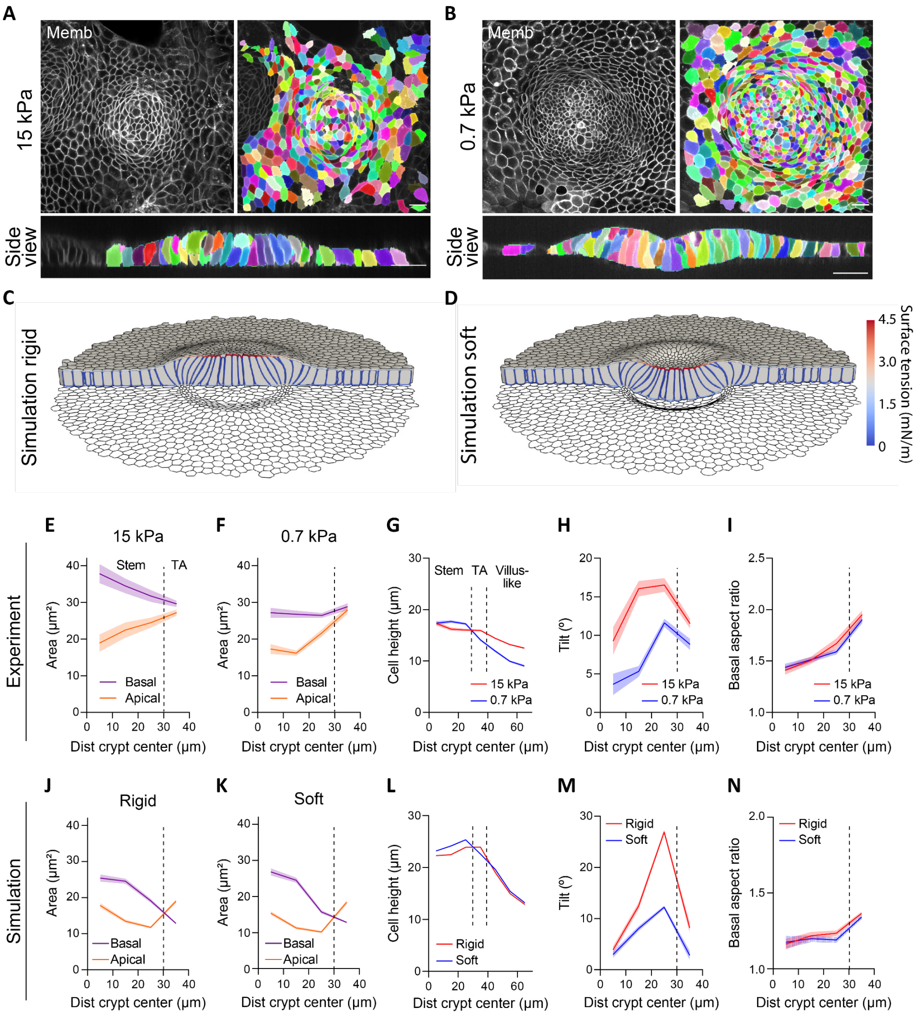

Figure 39. A vertex model recapitulates crypt folding and cell shapes. **A, B)** Three-dimensional crypt segmentation on stiff (**A**; 15 kPa) and soft (**B**; 0.7 kPa) substrates. Representative of three crypts per stiffness from two (0,7 kPa) and three (15 kPa) independent experiments. Colors indicate different cells. Scale bars, 20 µm. **C, D)** Three-dimensional vertex model of a monolayer adhered to a stiff (**C**) and soft (**D**) substrate. The colors in the cell outlines indicate the surface tension. **E, F)** Apical and basal area profiles on stiff (**E**; 15 kPa) and soft (**F**; 0.7 kPa) substrates. Paneth cells were excluded from the analysis (see Figure 38). From the center to the edge bins, n = 77, 198, 339 and 307 cells for **F**, and 32, 61, 102 and 230 for **E** from two and three independent experiments, respectively. **G-I)** Cell height (**G**), apicobasal tilt (**H**) and basal aspect ratio (**I**) as a function of the distance to the crypt center on soft and stiff substrates. Paneth cells were excluded from the analysis of the tilt and aspect ratio (see Figure

38). The vertical dashed lines indicate the boundary between the stem cell compartment and transit amplifying zone, and between the transit amplifying zone and villus-like domain (in **G**). The crypts and number of cells are the same as for **E** (15k Pa) and **F** (0.7 kPa). For the cell-height profiles: from center to edge bins, n = 77, 198, 339, 307, 242, 192 and 159 cells for the soft substrates, and n = 32, 61, 102, 230, 165, 125 and 106 cells for the stiff substrates. **J,K)** Simulated apical and basal area profiles on a rigid (**J**) and soft (**K**) substrate. From the center to the edge bins, n = 9, 26, 54 and 230 simulated cells for **K**, and n = 10, 28, 54 and 227 simulated cells for **J**. **L-N)** Simulated cell height (**L**), apicobasal tilt (**M**) and basal aspect ratio (**N**) on soft and rigid substrates. The crypts are the same as for **J,K**. Data are represented as the mean ± s.e.m. Memb, membrane; TA, transit amplifying zone; and a.u., arbitrary units.

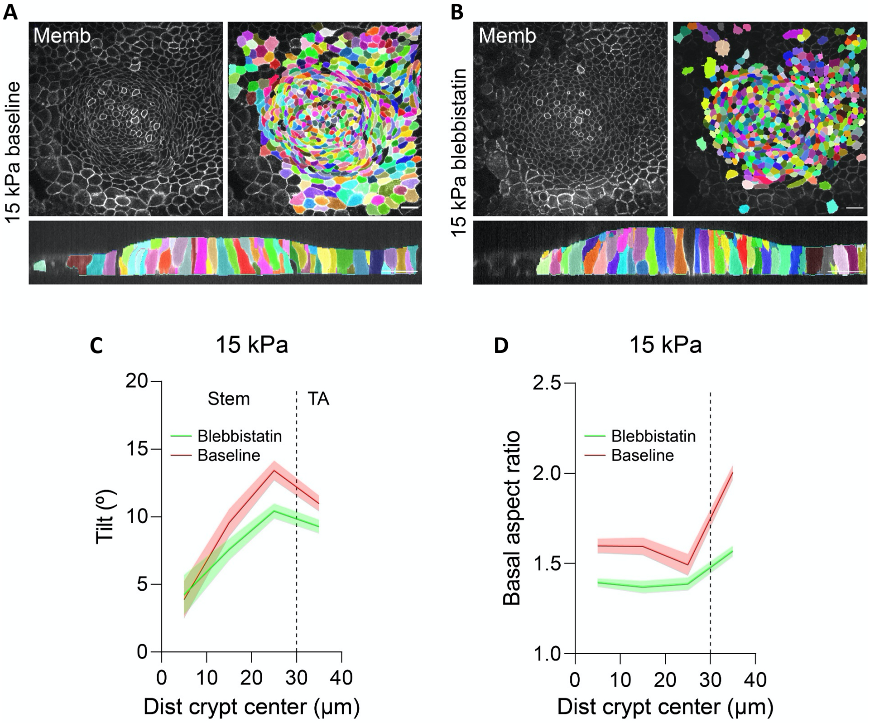

Figure 40. Effect of myosin inhibition on organoid cell shape. **A-B)** 3D segmentation of a crypt on 15 kPa gels under baseline conditions (**A**) and the same crypt after 3 h treatment with 15 µM of blebbistatin (**B**). **Top:** medial view. **Bottom:** lateral view. Representative images of 2 independent experiments. Scale bar, 20 µm. Memb, Membrane-targeted tdTomato. **C-D)** Apicobasal tilt (**C**) and basal aspect ratio (**D**) as a function of the distance to crypt center on rigid substrates (15 kPa) before and after blebbistatin. Vertical dashed line indicates the boundary between the stem cell compartment and the transit amplifying zone. From center to edge bins, n = 42, 72, 150 and 232 cells for baseline crypt and 39, 82, 131 and 209 for blebbistatin treatment. Data represented as mean ± s.e.m from 2 independent experiments.

Moreover, the model captured apical constriction (Figure 39J,K) and increased cell height (Figure 39L) at the stem cell compartment, apicobasal cell tilt (Figure 39M) and basal tangential elongation at the transit amplifying zone (Figure 39N). Besides cell and tissue morphology, the model also predicted the distribution of normal cell-substrate tractions (Figure 41A), from which we estimated a maximum apical tension of 4.6 ± 1.7 mN m−1 (mean ± s.d.). The model also captured the local recoil of the monolayer following laser cuts (Figure 41B,C). The overall agreement between the model and experiments shows that a stereotyped contractility pattern in the crypt can explain its stiffness-dependent shape and normal traction patterns.

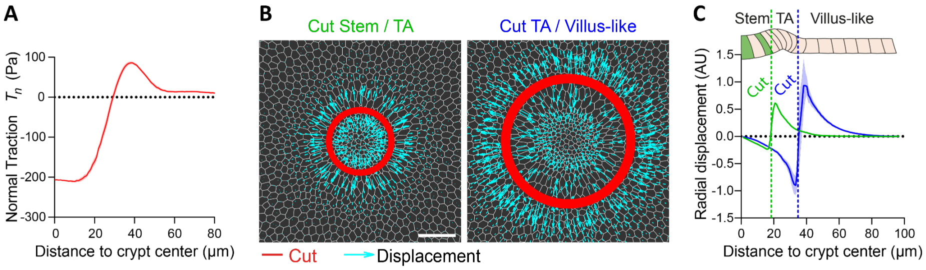

Figure 41. The 3D vertex model recapitulates the crypt tractions and tensional state. **A)** Simulated normal traction. **B)** Simulated tissue recoil after laser ablations (red) at the boundary between the stem cell compartment and transit amplifying zone (left), and the transit amplifying zone and villus-like domain (right). The cyan vectors indicate tissue displacement right after ablation, Scale bar, 20 μm. **C)** Radial displacement in the two simulated cuts. Data are represented as the mean ± s.d. The vertical dashed lines indicate cuts. Memb, membrane; TA, transit amplifying zone; and AU, arbitrary units.

4.6 Cell fate and mechanics co-evolve during crypt formation

We next studied how this mechanical picture co-evolves with cell-fate specification during crypt formation. We treated 3D organoids with ENR medium containing CHIR99021 and nicotinamide for 48 h to mimic a hyperproliferative fetal progenitor state[168,298,299]. Following this treatment, the organoids lost their buds and formed cysts. We then dissociated the cysts and seeded the resulting cells at high density on soft two-dimensional (2D) substrates. The cells adhered readily, proliferated and progressively formed a confluent monolayer. This monolayer lacked the packing geometry, apical accumulation of actomyosin, traction compartmentalization and expression pattern of Olfm4 and cytokeratin 20 characteristic of crypts and villi. One day after replacing the culture medium with regular ENR, we observed the formation of cellular foci that expressed Olfm4, exhibited apical F-actin and myosin IIA, and generated downwards traction (Figure 42A,B). The expression levels of Olfm4 inside the foci and cytokeratin 20 outside them increased steadily over the following days (Figure 42C,D). The number foci was constant in time, and their size plateaued after 24 h (Figure 42E,F). F-actin and myosin IIA increased over time at the apical and basal surfaces of both the crypt and the villus-like compartments (Figure 43A,B; Figure 44A,B). Although the apical actin and myosin densities at the stem cell compartment were the highest across the monolayer, their ratio to the basal densities decreased with time (Figure 43C; Figure 44C). However, the normal forces at the center of the stem cell compartment increased, probably because of the rise in the total amount of actomyosin (Figure 42G). These experiments show that apical constriction and pushing forces arise as early as the time at which Olfm4 foci can be detected (day 2), before crypt size and density in the monolayer are established (day 3). Forces thus co-evolve with fate specification to progressively shape a mature compartmentalized epithelium.

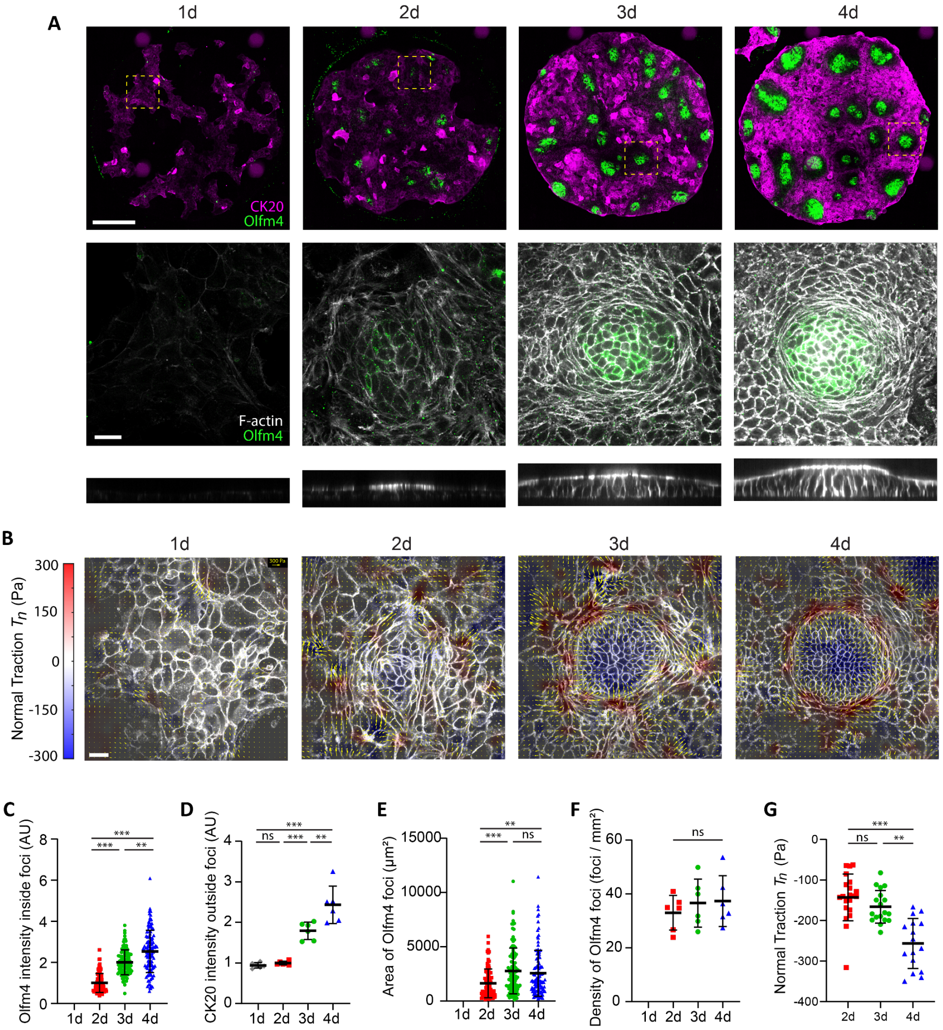

Figure 42. Co-evolution of cell fate and tissue mechanics during de novo crypt formation. **A)** Olfm4 and cytokeratin 20 immunostaining following the development of the monolayers over four consecutive days (**top**). F-actin (phalloidin) and Olfm4 immunostaining (**middle**), and lateral views of F-actin (**bottom**) at the positions indicated with a dashed square in the corresponding monolayers of the top row. Scale bars, 200 µm (top) and 20 µm (bottom). Representative images of two independent experiments. **B)** Three-dimensional tractions at the indicated time points. The yellow vectors represent components tangential to the substrate and the color map represents the component normal to the substrate. Scale bar, 20 µm. Scale vector, 300 Pa**.** Representative images of two independent experiments. **C-F)** Olfm4 intensity inside the Olfm4+ foci (**C**), cytokeratin 20 intensity in the Olfm4– regions (**D**), area of the Olfm4+ foci (**E**) and density of the Olfm4+ foci (**F**) at the indicated time points; n = 90 (2 d), 112 (3 d) and 115 (4 d) Olfm4+ foci (**C,E**), and n = 6 (1, 2, 3 and 4 d) circular patterns (**D,F**) from two independent experiments. **G)** Mean normal traction at the stem cell

compartment for the indicated time points; n = 21 (2 d), 18 (3 d) and 16 (4 d) crypts from two independent experiments. **C-G**, Data are represented as the mean ± s.d. Statistical significance was determined using a Kruskal–Wallis test, followed by a Dunn's multiple-comparison test (C,E,G), and a one-way analysis of variance, followed by a Tukey's multiple-comparison test (D,F); $*P < 0.05$; $**P < 0.01$; $***P < 0.001$; and ns, not significant ($P > 0.05$). CK20, cytokeratin 20; and AU, arbitrary units. Stiffness of all gels, 5kPa.

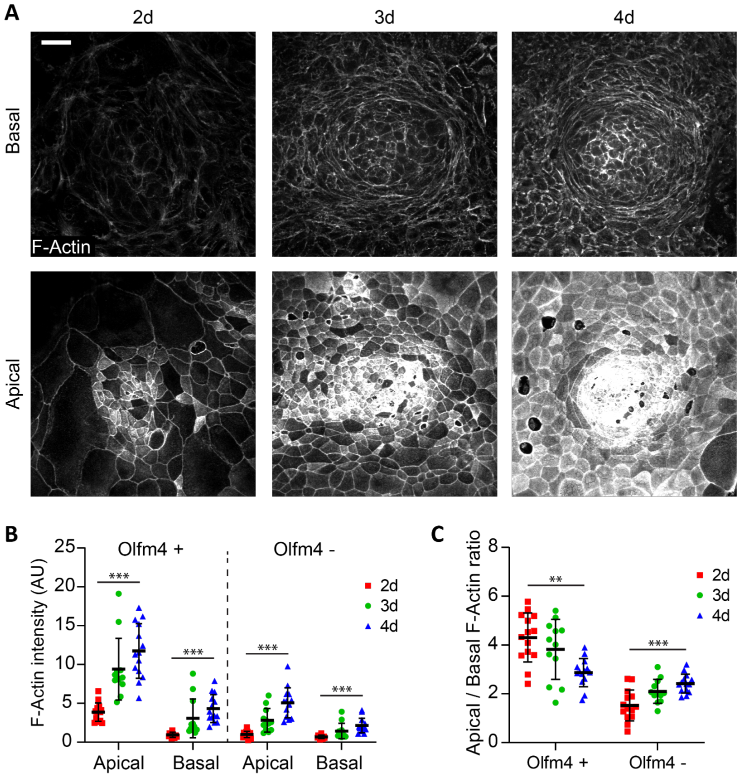
A
2d
3d
4d
Basal
Apical
F-Actin
B
Olfm4 +
Olfm4 -
F-Actin intensity (AU)
0
5
10
15
20
25
***
***
***
***
2d
3d
4d
Apical
Basal
Apical
Basal
C
Apical / Basal F-Actin ratio
0
2
4
6
8
**
***
2d
3d
4d
Olfm4 +
Olfm4 -

Figure 43. F-Actin distribution during de novo crypt formation. **A)** Apical and basal projections of F-Actin (Phalloidin, A) of crypts at the indicated timepoints (2 days, 3 days, 4 days). The crypts are the same as in Figure 42A. Representative images of 2 independent experiments. Scale bar, 20 µm. **B,C)** Quantification of apical and basal F-actin intensity (**B**) and apical/basal F-actin ratio (**C**) at the Olfm4 positive and Olfm4 negative regions for the indicated timepoints. n = 14 (2d), 12 (3d) and 14 (4d) crypts from 2 independent experiments. For all the graphs, data is represented as mean ± s.d. Stiffness of the gel, 5 kPa. * ($p < 0.05$) ***($p < 0.001$). ns, not significant ($P>0.05$); AU, arbitrary units. Statistical significance was determined using a Kruskal–Wallis test, followed by a Dunn's multiple-comparison test (**B** and **C** for Olfm4+), and a one-way analysis of variance, followed by a Tukey's multiple-comparison test (**C** for Olfm4−); $*P < 0.05$; $**P < 0.01$; $***P < 0.001$. Only the statistical comparison between 2d and 4d is shown.

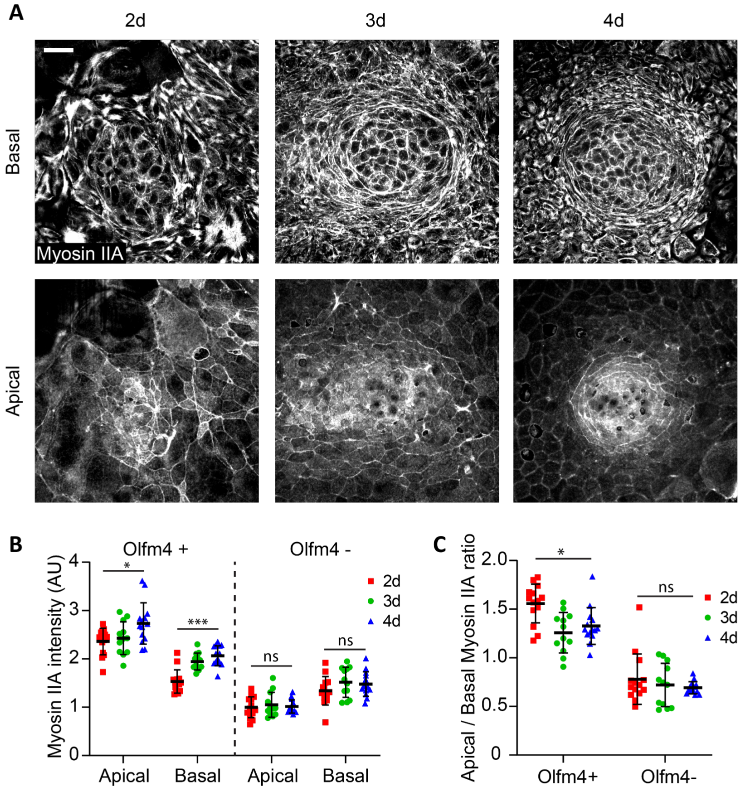
A
2d
3d
4d
Basal
Apical
Myosin IIA
B
Olfm4 +
Olfm4 -
Myosin IIA intensity (AU)
0
1
2
3
4
*
***
ns
ns
Apical
Basal
Apical
Basal
2d
3d
4d
C
Apical / Basal Myosin IIA ratio
0
0.5
1.0
1.5
2.0
*
ns
Olfm4+
Olfm4-
2d
3d
4d

Figure 44. Myosin IIA distribution during de novo crypt formation. **A)** Apical and basal projections of myosin IIA–eGFP of crypts at the indicated timepoints (2 days, 3 days, 4 days). The crypts are the same as in Figures 42A and 43. Representative images of 2 independent experiments. Scale bar, 20 µm. **B,C)** Quantification of apical and basal myosin IIA intensity (**B**) and apical/basal myosin IIA ratio (**C**) at the Olfm4 positive and Olfm4 negative regions for the indicated timepoints. n = 14 (2d), 12 (3d) and 14 (4d) crypts from 2 independent experiments. For all the graphs, data is represented as mean ± s.d. Stiffness of the gel, 5 kPa. * ($p < 0.05$) ***($p < 0.001$). ns, not significant ($P>0.05$); AU, arbitrary units. Statistical significance was determined by a Kruskal– Wallis followed by a Dunn's multiple-comparison test (**B**: basal Olfm4+ and **C**) and one-way ANOVA followed by a Tukey multiple-comparison test (**B**: apical Olfm4+, apical Olfm4- and basal Olfm4-). Only the statistical comparison between 2d and 4d is shown.

4.7 Comparison with the intestinal epithelium *in vivo*

To assess whether our organoids captured the cellular morphology and cytoskeletal organization of the *in vivo* crypt and villus, we studied whole-mount sections of the small intestine of mice. We focused on myosin IIA to avoid the confounding contribution of non-contractile F-actin at the brush border (Figure 45A). Apical myosin IIA was highest at the stem cell compartment and dropped at the villus. By contrast, basal myosin IIA increased progressively from the base of the crypt towards the villus, where the presence of stromal cells prevented further quantification (Figure 45B,C).

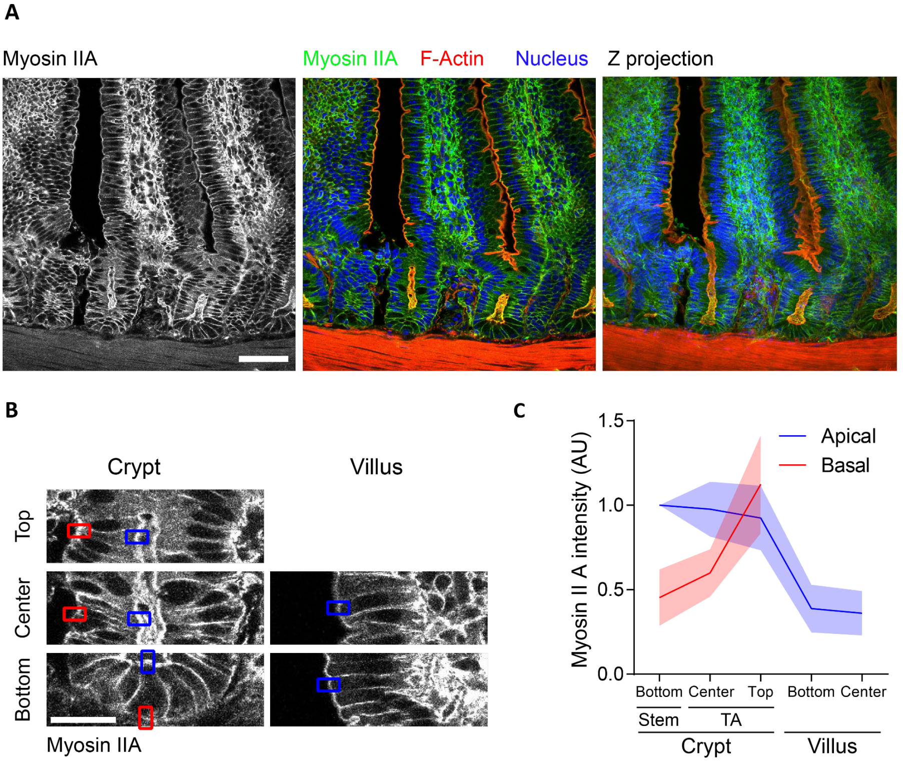
A
Myosin IIA
Myosin IIA
F-Actin
Nucleus
Z projection
B
Crypt
Villus
Top
Center
Bottom
Myosin IIA
C
Myosin II A intensity (AU)
1.5
1.0
0.5
0.0
Apical
Basal
Bottom
Center
Top
Bottom
Center
Stem
TA
Crypt
Villus

Figure 45. Cytoskeletal organization of the intestinal epithelium in vivo. **A)** Staining of F-actin (phalloidin) and nuclei (4,6-diamidino- 2-phenylindole, DAPI) of tissue sections of the small intestine of myosin IIA–eGFP mice. Myosin IIA–eGFP signal (**left**). Overlay of myosin IIA–eGFP, F-actin and nuclei (**center**). Maximum intensity z-projection of the overlayed channels to better visualize the continuity of the crypt–villus axis (**right**). Scale bar, 40 µm. **B)** Illustration of the approach used to quantify the myosin IIA intensity along the crypt–villus axis in tissue sections. The myosin intensity was measured

at the basal (red) and apical (blue) sides of cells at the indicated crypt and villus regions. Note that the high myosin IIA intensity of stromal cells prevented accurate quantification of the basal epithelial intensity at the villus. Scale bar, 20 µm. **C)** Apical and basal myosin IIA distribution along the crypt–villus axis of tissue sections. Data are represented as the mean ± s.d. of n = 13 crypt–villus units from three mice; AU, arbitrary units.

The cells at the base of the crypt were slightly tilted towards the villus. This tilt is in the opposite direction to that observed in our organoids, showing that besides active processes, tilting is influenced by curvature and spatial constrains[300]. Beyond this highly curved region, the cells were tilted towards the crypt center, in agreement with our observations in organoids (Figure 46). Together, these data reveal a substantial agreement between organoids and the intestinal epithelium.

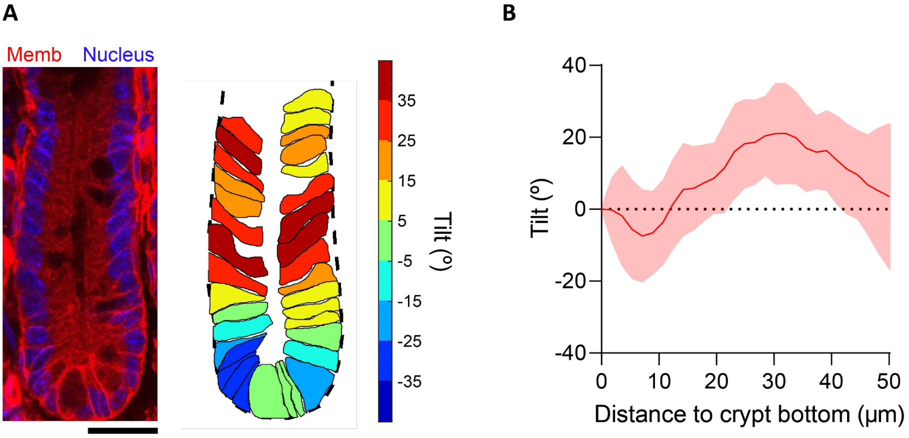

Figure 46. Cell morphology of the intestinal epithelium in vivo. **A)** Example of an intestinal crypt from membrane–tdTomato mice (**left**). The membrane signal (Memb) has been overlaid on the nuclear signal (DAPI). Representative image of 16 crypts from three mice. Cell segmentation of the same crypt (**right**). The basal contour of the crypt is delineated with a black dashed line. Individual cells are colored according to their tilting angle with respect to the normal direction to the crypt contour (positive indicates towards the crypt bottom; negative indicates away from the crypt bottom). Scale bar, 20 µm. **B)** Cell tilt along the crypt axis. Data are represented as the mean ± s.d. of n = 16 crypts from three mice.

4.8 Eph/Ephrin signaling regulates crypt-villus boundary formation in open-lumen intestinal organoids

Our data indicate that the basally constricted cells at the transit amplifying region act as a dynamic mechanical boundary between the stem cell niche and the villus-like region (Figure 31). We next studied how this mechanical boundary is established and maintained and whether it regulates cell fate specification and compartmentalization along the crypt-villus axis. We focused on the Eph/Ephrin signaling pathway, given its known pivotal role on intestinal cell positioning and tissue compartmentalization[177,233–235,238,241,301,302]. We first assessed the distribution of the EphB receptors in the organoid monolayers (Figure 47).

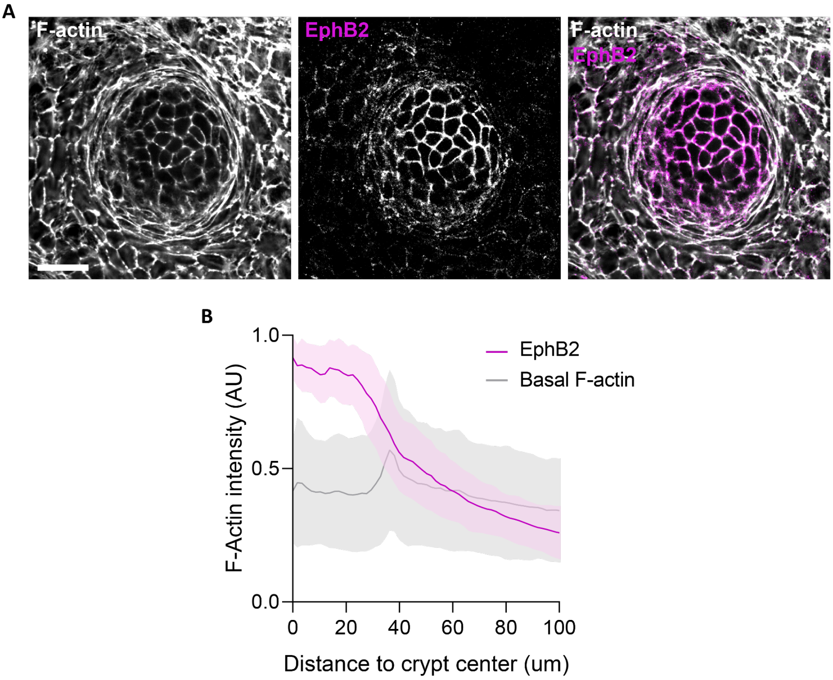

Figure 47. EphB2 receptor distribution in open-lumen organoids. **A)** Immunostainings of F-actin (phalloidin, left), EphB2 receptor (middle) and composite (right). **B)** Radial distribution of the basal F-actin intensity (gray) and EphB2 receptor intensity (magenta) as a function of the distance to the crypt center. Data is represented as the mean ± s.d. of n = 20 crypts from 3 independent experiments. Scale bar, 20 µm; Stiffness of the substrate, 5kPa.

As expected, EphB2 receptor was highly expressed at the crypt-like regions (Figure 47A)[177,198,231,303]. Interestingly, EphB2 expression sharply decreased at the crypt-villus boundary, coinciding with the formation of circumferential actin cables and basal constriction of the transit amplifying cells (Figure 47A, B). Motivated by these results, we hypothesized that Eph/Ephrin signaling may regulate crypt-villus boundary formation and tissue compartmentalization by inducing basal constriction of transit amplifying cells.

To test this hypothesis, we generated organoids from EphB2 and EphB3 double knock out mice (EphB2/3 dKO) and their wild type counterparts (EphB2/3 WT). We then grew EphB2/3 WT and EphB2/3 dKO stem cells on confined circular ECM micropatterns, where they both formed confluent compartmentalized monolayers (Figure 48A).

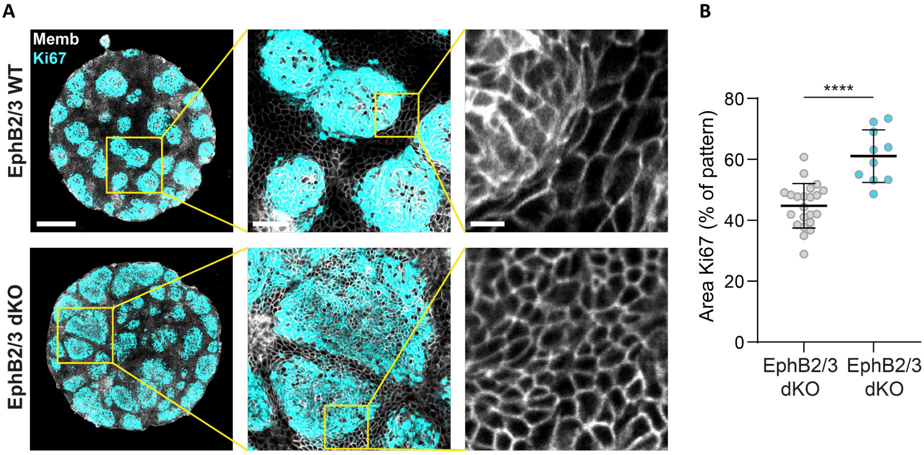

Figure 48. EphB2/3 dKO organoids compartmentalize into proliferative and non-proliferative regions of defective size. **A) Left column:** Representative immunostainings of the proliferation marker Ki67 in EphB2/3 WT and EphB2/3 dKO organoids grown on circular ECM micropatterns. Images are maximum intensity projections. Scale bar, 200 µm; Stiffness of the substrate, 5kPa; Memb, membrane-targeted tdTomato. **Center column**: zoom of a basal plane at the indicated region in the left image. Scale bar, 50 µm. **Right column:** zoom of the membrane signal at the indicated region of the center image. Scale bar, 10 µm. **B)** Quantification of the proliferative area (percentage of the pattern area that is positive for Ki67). Data is represented as mean ± s.d. of n = 22 micropatterns (EphB2/3 WT) and n = 10 micropatterns (EphB2/3 dKO) from 2 independent experiments. Statistical difference was determined by a two-tailed Mann-Whitney test. ****(P<0.0001).

The basal constriction at the crypt-villus boundary was less pronounced in EphB2/3 dKO organoids (Figure 48A, right inset), supporting a role of Eph-Ephrin signaling in basal constriction of transit amplifying cells. Nevertheless, the tissue retained the typical compartmentalization into proliferative (ki67+) and non-proliferative (ki67-) domains (Figure 48A). Strikingly, however, the proliferative domain was significantly larger in EphB2/3 dKO organoids compared to wildtype (Figure 48B).

The mechanism behind the enlargement of the proliferative region in EphB2/3 dKO organoids is under current active investigation. Interestingly, although Paneth cell density remained constant in EphB2/3 WT and dKO organoids (Figure 49A, B), their typical clustering at the center of the crypt (Figure 49A-top) was impaired in EphB2/3 dKO organoids, where they became more scattered (Figure 49A-bottom, C).

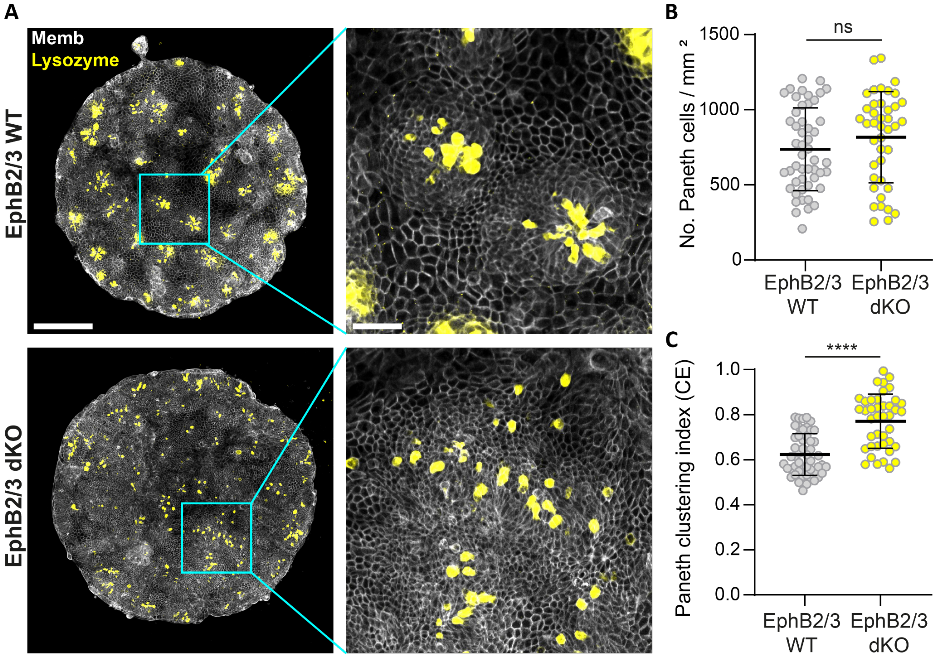

Figure 49. Paneth cells are scattered in EphB2/3 dKO open-lumen organoids. **A)** Representative immunostainings of Paneth cells (Lysozyme) in EphB2/3 WT and EphB2/3 dKO organoids grown on circular ECM micropatterns. Regions indicated in cyan are zoomed in the right images. Stiffness of the substrate, 5 kPa; left scale bar 200 µm; Scalebar of the zooms, 40 µm. **B, C)** Quantification of the Paneth cell density (**B**) and the Clark-Evans (CE) clustering index of Paneth cells (**C**) in EphB2/3 WT and

EphB2/3 dKO organoids. Data is represented as mean ± s.d. of 50 (EphB2/3 WT) and 41 (EphB2/3 dKO) organoid micropatterns from 3 independent experiments. Statistical significance was determined by a two-tailed Mann-Whitney test. Memb, membrane-targeted tdTomato; ns, not significant ($P>0.05$), **** ($P<0.0001$).

A similar scattering phenotype is observed *in vivo*[177,234,235] (Figure 50). As Paneth cells are the only source of Wnt3 in organoids, a plausible mechanism is that their mispositioning in EphB2/3 dKO organoids could result in a broader Wnt gradient and expansion of the proliferative compartment.

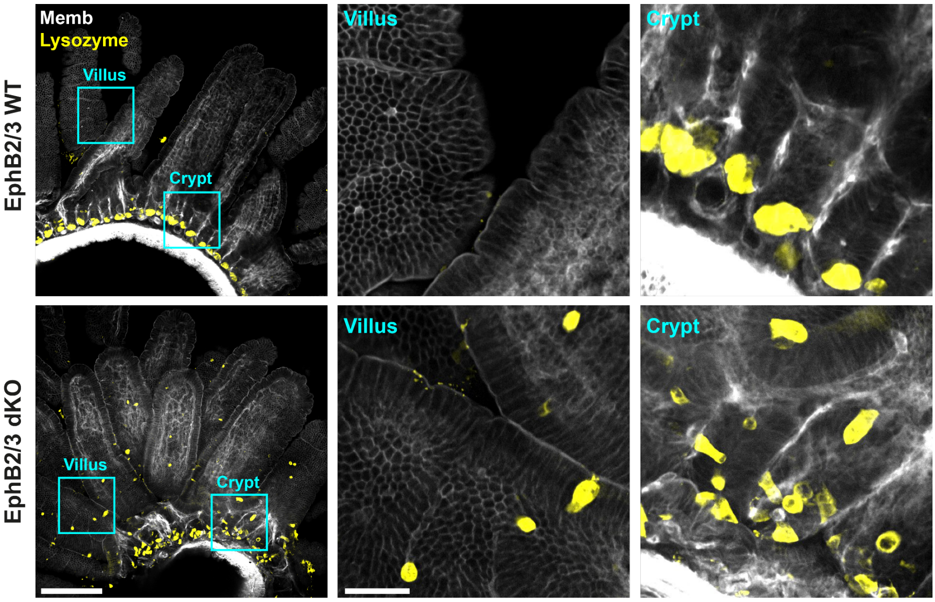

Figure 50. Paneth cell mispositioning in vivo in EphB2/3 dKO mice. Whole mount immunostainings of Paneth cells (Lysozyme) in the proximal intestine of EphB2/3 WT and EphB2/3 dKO mice. Scale bar, 200 µm. The crypt and villus regions highlighted in cyan are zoomed in the middle (villus) and right (crypt) images. Scale bar of the zooms, 40 µm. Images representative of 7 (EphB2/3 WT) and 2 (EphB2/3 dKO) mice. Memb, membrane-targeted tdTomato.

Overall, these experiments highlight the role of Eph/Ephrin signaling in establishing and maintaining the mechanical and biological compartmentalization of the intestinal epithelium. Further experiments will help disentangle the specific molecular mechanisms taking place and their functional consequences on intestinal homeostasis.

4.9 Cells are dragged out of the crypt

We next studied the dynamics of the cell monolayer. Cell movements at the villus are driven by active migration[261] but the mechanisms driving movements from the crypt to the villus remain unknown. The widely assumed mechanism for such movements, a pushing force arising from compression downstream of mitotic pressure[152,255,256], is incompatible with our observation that the transit amplifying zone is under tension. To address the mechanisms underlying cell movements, we studied maps of cell velocities and forces in the organoid monolayers (Figure 51A-J). Particle imaging velocimetry (PIV) on 5 kPa gels revealed strong spatial fluctuations in cell velocities, characterized by clusters of fast-moving cells surrounded by nearly immobile ones (Figure 51A). To average out these fluctuations and unveil systematic spatiotemporal patterns, we computed the average radial velocity as a function of the distance from the crypt center. Kymograph representation of this average showed that the radial velocity was weak in the central region of the stem cell compartment, begun to increase near the transit amplifying zone and peaked at the boundary with the villus-like domain (Figure 51C,I). The cell division rate followed an opposite profile characterized by a plateau at the stem cell compartment and a decrease thereafter.

To understand how the spatial distribution of cell velocity arises from cellular forces, we turned to kymographs of radial cell–ECM tractions and radial cell–cell monolayer tension measured using monolayer stress microscopy (Appendix 2)[36]. Similar to the velocity kymographs, the traction and tension kymographs were stationary, confirming that our open-lumen organoids are in steady state within our window of observation (Figure 51D,E). Kymographs of the radial tractions displayed the three compartments already shown in Figure 31C; in the stem cell compartment the radial tractions pointed inwards, in the transit amplifying zone they vanished, and in the villus-like domain they pointed outwards (Figure 51D, I). By contrast, kymographs of the cell–cell tension showed a minimum at the transit amplifying zone flanked by two tension gradients that built up towards the center of the crypt and towards the villus-like domain (Figure 51E,I).

We repeated this set of experiments on softer substrates (0.7 kPa; Figure 51B), which showed similar cell velocity profiles to those obtained on the 5 kPa substrates

(Figure 51F-H, J). In this compartment, the radial tractions were nearly one order of magnitude weaker than on the 5 kPa substrates. Close to the transit amplifying zone, the radial tractions changed direction and displayed a positive peak of similar magnitude but shorter length than on the 5 kPa substrates.

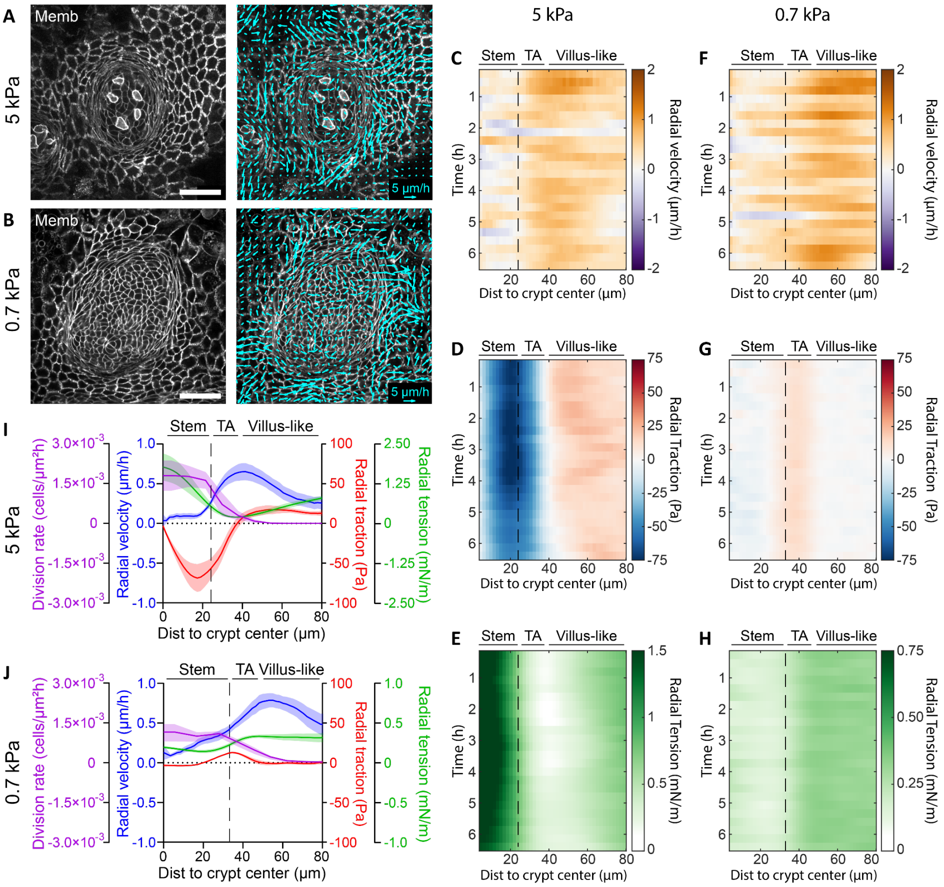

Figure 51. Dynamics of open-lumen intestinal organoids in stiff and soft substrates. **A,B)** Representative velocity maps (right) overlaid on membrane-targeted tdTomato signal (Memb; left) on 5 kPa (**A**) and 0.7 kPa (**B**) substrates. Representative images of five crypts from three independent experiments (**A**) and seven crypts from two independent experiments (**B**)**.** Memb, membrane; Scale bars, 40 µm; Scale arrow 5 µm/h. **B)** Due to pronounced crypt folding, for visualization purposes, the image for the 0.7 kPa substrate is a projection along the crypt medial plane. **C-H)** Kymographs showing the circumferentially averaged radial velocity (**C,F**), radial traction (**D,G**) and radial tension (**E,H**) on 5 kPa (**C-E**) and 0.7 kPa (**F-H**) substrates for 6.5 h. The vertical dashed line indicates the boundary between the stem cell compartment and the transit amplifying zone. **I,J)** Time-averaged radial profiles

of the traction, tension, velocity and cell division rate on 5 kPa (**I**) and 0.7 kPa (**J**) substrates. The vertical dashed line indicates the boundary between the stem cell compartment and the transit amplifying zone. Data are represented as the mean ± s.e.m. of n = 5 crypts from three independent experiments (**C-E, I**) and n = 7 crypts from two independent experiments (**F-H, J**). Note that for an unbounded monolayer, monolayer stress microscopy computes stress up to a constant (Appendix 2). As the laser cuts indicated tension everywhere in the monolayer, this constant was arbitrarily set so that the minimum tension throughout the time lapse was zero.

The pronounced negative gradient in tension observed at the stem cell compartment on the 5 kPa substrates nearly vanished on the 0.7 kPa substrates. However, we found a positive tension gradient that begins at the boundary of the stem cell compartment, persists through the transit amplifying zone, and decays thereafter. Thus, despite large quantitative differences at the stem cell compartment on soft and stiff substrates, the radial tractions on both substrates displayed a region where they changed sign and pointed away from the crypt center, resulting in a positive tension gradient.

To further substantiate this tensional landscape, we again resorted to laser ablation but this time we cut the monolayer radially. As commonly observed in laser ablation experiments, we found recoil perpendicular to the cut (Figure 52A,B). Surprisingly, however, the dominant recoil component was parallel to the cut. This radial recoil was minimum at the boundary between the crypt and the villus-like domain and increased on either side of it. Our vertex model predicts radial recoil at the stem cell compartment as a consequence of apical constriction but not at the villus-like domain (Figure 52C). Recoil in this domain is consistent with a tensile gradient associated with migratory forces that pull cells out of the crypt, which are not included in our model.

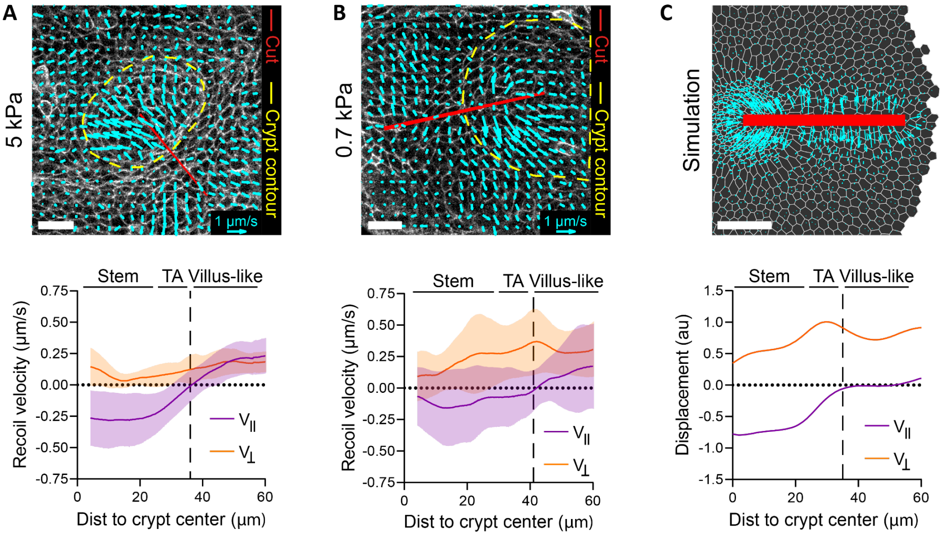

Figure 52. Radial laser cuts on open-lumen organoids on stiff and soft substrates. Recoil velocity maps (**top**), and the parallel and perpendicular velocity (**bottom**) immediately after laser ablation along the crypt–villus axis on 5 kPa (**A**) and 0.7 kPa (**B**) substrates, and simulations (**C**). The red lines indicate the ablated area. The yellow dashed lines indicate the crypt contours. Data are represented as the mean ± s.d. of n = 11 crypts from three independent experiments (**A**) and n = 13 crypts from four independent experiments (**B**). Scale bars, 20 µm.

Together, our data indicate that cells exit the crypt using a collective cell-migration mode in which cell velocity is parallel to cell-substrate traction, rather than antiparallel to it. This alignment is opposite to that observed at the leading edge of advancing monolayers[35,122]. Because cells are under tension, outward-pointing tractions cannot arise from pushing forces generated at the stem cell compartment. Our evidence instead indicates that cells at the crypt are dragged by other cells located further into the villus-like domain, much as the trailing edge of a cell cluster is dragged by the leading edge[304]. Thus, the boundary of the crypt can be understood as a multicellular trailing edge that is constantly being replenished with cells through proliferation.

5 Discussion

The apparent harmony in the structure and behavior of many biological systems is governed by the constant interplay between form, fate and function. This interplay is clearly exemplified in the intestinal epithelium. Starting from a flat sheet of epithelial cells, the intestinal epithelium is reshaped into concave (crypts) and convex (villus) structures. Reshaping of this tissue satisfies the large surface area demanded for its main function – absorbing nutrients. The folding of the intestinal epithelium imposes a clear compartmentalization of cell fate and function along the crypt-villus axis. At the villus, cells specialize in absorbing nutrients and secreting molecules, while undifferentiated cells at the crypt proliferate to constantly replenish the villus population. Importantly, the tissue forces and the mechanical environment of the epithelium have a crucial role in its form, fate and function, from the early development of the tissue to the proper functioning of the adult gut.

Over the last decade, important discoveries have been made on the mechanics of intestinal epithelium morphogenesis and homeostasis. However, significant gaps of knowledge preclude a comprehensive understanding of the intestinal epithelium dynamics. For instance, the specific role of epithelial forces during crypt folding; whether active or passive mechanisms drive migration from crypt to villus; or the forces that drive cell sorting and tissue compartmentalization into crypt and villus regions are only partially understood. In part, this is due to the limited applicability of mechanical measurement techniques on the *in vivo* set-up. In this context, the development of intestinal organoid systems about a decade ago opened a new era in the field, providing experimentally accessible systems *in vitro*.

In this thesis, by combining the intestinal organoid technology with high resolution force measurements, we aimed at deepening the current understanding of the mechanics of three fundamental processes in the intestinal epithelium - crypt folding, crypt-villus compartmentalization and crypt to villus cell migration.

We started by generating an organoid culture system over polyacrylamide gels that is compatible with cell-cell and cell-ECM force measurements. Remarkably, under these culture conditions the organoids formed monolayers that retained the tissue compartmentalization into crypt-like and villus-like structures. We use the term “open-lumen intestinal organoid” to differentiate them from the typical organoid system embedded in Matrigel developed by Sato and colleagues[194], where a pressurized enclosed lumen is formed. Of note, similar culture systems have been developed by other groups[198–201]. For instance, Thorne et al.[199], Liu et. Al[200] and Altay et.al[198] grew intestinal organoids over Matrigel substrates, where they self-organized into crypt-like and villus-like domains. Importantly, as we also found, they were able to grow open-lumen intestinal organoids both from tissue pieces and from single cells derived from close lumen organoids or *in vivo* crypts. This is a very interesting feature of the system, as it implies that the pre-existing crypt configuration before seeding does not necessarily define the final crypt-like domain in the open-lumen organoid. During the development of closed-lumen intestinal organoids or upon injury of the intestinal epithelium, a fetal-like YAP-driven regenerative program is activated, inducing undifferentiation of the stem cells (LGR5+)[195,247–250]. It is very likely that upon tissue disaggregation during seeding, the same regenerative program is activated both in single cells and organoid pieces. Thus, stem cell dedifferentiation may dilute any influence from a pre-existing crypt configuration on the final open-lumen organoid crypt, although this needs to be formally tested.

By combining open-lumen intestinal organoids with traction microscopy, we were able to quantitatively map the 3D forces that the intestinal epithelium exerts on the underlying substrate. We found that the stem cell niche pushes on the substrate while the transit amplifying cells pull on it. Broguiere et al.[305] performed 3D traction force microscopy on budding closed-lumen organoids grown in fibrin hydrogels supplemented with 10% Matrigel. Of note, and as acknowledged by the authors, their force measurements are not to be taken as quantitative measurements of the forces but rather as an estimate, due to the degradability and viscoelasticity of the matrix they use. Importantly, and supporting our results, they find a similar pattern of tractions in the budding organoids - budding structures push the substrate, while interbud regions pull on it.

A very important feature of the open-lumen organoids that we employ here is the precise control over the substrate stiffness. This allowed us to study both the mechanics of the tissue (i.e. the cell-cell and cell-ECM forces) and the impact that the mechanical environment (i.e. the stiffness of the substrate) can have on the tissue dynamics. When we seeded the organoids on sufficiently soft gels, the crypt-like regions were able to acquire the typical folded geometry of the crypts found in closed-lumen organoids and *in vivo*. We wondered whether the increased tissue curvature in soft gels could feedback to the force generation. Interestingly, however, we found that cells are somehow encoded to exert a well-defined traction pattern where the pushing force at the crypt and the pulling force at the transit amplifying region remains constant over substrate stiffness and crypt geometry. These results indicate that substrate stiffness seems to be the main parameter that opposes tissue folding and instructs the final configuration of the crypt in open-lumen intestinal organoids. Xi et al.[306] have recently reported a value of around 150 Pa for the crypt ECM, which is similar to the stiffness condition where we find a pronounced folding of the crypt.

Through myosin inhibition, circumferential laser cuts and vertex model simulations based on the measured actomyosin distribution in open-lumen organoids, we show that the tractions and folding of the crypt are generated via apical constriction of the stem cell niche. These results are in line with previous *in vivo*[226] and *in vitro*[227] data and are further supported by a recent work on closed-lumen organoids[307] . Yang et al.[307] report apical constriction of the crypt and basal constriction beyond the boundary of the niche. In their case, however, the osmotic pressure of the organoid lumen acts as an additional morphogenetic force. They report that lumen shrinkage, accompanied by an increase in the volume of enterocyte cells is necessary for crypt folding. Although we have not addressed enterocyte volume, the fact that the stem cell compartment in our open-lumen organoids folds further when separated from the rest of the epithelium (Figure 37F), indicates that the villus-like compartment is dispensable for crypt folding. We cannot, however, exclude a contribution of luminal pressure to further invagination of the tissue. This may explain why the folding levels that we obtain are less pronounced than *in vivo*. Moreover, further invagination of the tissue might be facilitated *in vivo* by matrix remodeling or other contributions from the stroma, which are not included in our model.

The concave geometry of the folded crypt is a topological cue that could instruct cell fate. Indeed, imposing substrate curvature to intestinal organoids is sufficient to guide the formation of crypt domains at concave regions[206–208]. Nevertheless, our data on flat substrates indicate that substrate curvature is not necessary for crypt emergence and folding. However, we cannot exclude a possible positive feedback between tissue curvature and stem cell fate in our organoids. Certainly, the specific traction pattern that folds the crypt co-emerge with crypt fate specification. We also find that stem cells are the main contributors to the folding of the crypt via apical constriction, as recently corroborated by a recent report[308]. Pentinmikko et al.[308] show that the cone geometry of the intestinal stem cells acquired through apical constriction increases their lateral surface to volume ratio (LSV), and propose that this enhances signaling from neighboring Paneth cells. Indeed, when organoids were grown on scaffolds with lower curvature or treated with drugs that disrupt apical constriction, the LSV of intestinal stem cells decreased and both Notch and Wnt signaling were reduced[308]. Thus, although the crypts can fold without a preexisting curvature in the substrate, the acquired concave geometry might enhance and sustain stem cell fate.

Besides creating a permissive environment for tissue folding, by using substrates of varying stiffness we also found that crypt size and the number of stem cells therein decrease on stiff gels. This may be due to differential activation of mechanotransduction pathways at different rigidities. Indeed, He et al. have recently reported a similar decrease in the size of crypt-like regions on stiff substrates, due to the nuclear translocation of the transcriptional factor YAP/TAZ[309]. Given the increase in crypt folding on soft substrates, stem cell fate might be also enhanced by the acquired curvature, as commented before[308]. Of note, the crypt-like domains in our open-lumen organoids contain ~100-300 Olfm4 positive cells (Figure 33), an order of magnitude higher than the number of stem cells reported *in vivo* (~14 stem cells)[159]. The ratio stem/Paneth that we observe in open lumen organoids is also higher than in vivo - as the number of Paneth cells per crypt *in vivo* is ~6[172,310]. This means that a Paneth cell in our organoids sustains more stem cells than a Paneth cell *in vivo*. Given that Wnt and Notch signals provided by Paneth cells require cell-cell contact[311], a Paneth cell in open lumen organoids should thus contact more stem cells than a Paneth cell *in vivo*. Given the complex shape of the crypt cells (Figure 38), Paneth cells might contact multiple and different neighbors along the apicobasal axis.

Pumping of ions across an epithelium can generate an osmotic differential between the apical and basal side of the monolayer, inducing a water flow from the hypotonic to the hypertonic compartment. If ions accumulate at the basal side of the monolayer, the water flow and the hydrostatic pressure generated can induce the delamination of the epithelium into domes[11,312]. In our open-lumen organoids, we find a similar behavior at the villus-like regions, where the epithelium sometimes delaminated into domes. The formation of the lumen in closed lumen organoids is also due to osmotic differentials downstream of ion pumping. However, in contrast to domes, the ions in closed lumen organoids are pumped from the basal to the apical side of the epithelium[313]. In the *in vivo* intestinal epithelium, and as in open-lumen organoids, the ion pumping at villus cells also generates a water influx from the apical to the basal side of the epithelium[314]. Nevertheless, to our knowledge, the epithelium remains constantly attached to the basement membrane and domes are not observed *in vivo*. Different reasons may explain why the epithelium delaminates in open-lumen organoids. One of them is the specific ECM composition of our culture system. We use a homogeneous coating of Collagen I and Laminin I, a situation that differs from the *in vivo* tissue. *In vivo*, the basement membrane contains Collagen IV and the ECM composition as well as the type of cell-ECM adhesion molecules expressed by epithelial cells vary along the crypt-villus axis[138]. Thus, the specific ECM coating used in our system may be less optimal for differentiated cells compared to *in vivo*, favoring delamination upon water influx. Interestingly, epithelial cells can generate some basal protrusions that cross the basement membrane *in vivo*[256,315–317] . Another possibility is that these protrusions may help anchoring the cells more strongly *in vivo*, to impede tissue delamination.

The stereotypical pattern of tractions observed in the organoids defines distinct mechanical and functional compartments – the stem cell niche, the transit amplifying region and the villus-like region. In this context, the formation of circumferential actomyosin cables and basal constriction of transit amplifying cells seems to generate a mechanical boundary that isolates the stem cell niche from the villus-like domain. We find that the actin cables and basal constriction of the transit amplifying cells correlates with the expression of molecules of the Eph/Ephrin signaling pathway. Specifically, and assuming that the villus-like region should express EphrinB ligands, basal constriction happens at the boundary between EphB/EphrinB expressing cells. Motivated by these results, we disrupted Eph/Ephrin signaling and found that indeed, the mechanical boundary gets diluted in EphB2/3 dKO organoids. During neural tube segmentation in mouse[238] and zebrafish[241], similar actomyosin cables downstream of Eph/Ephrin signaling are formed at the boundaries between rhombomeres. In the rhombomeres, the cells that divide next to the junction between two rhombomeres are not able to cross to the neighbor rhombomere[241]. Contrarily, in the intestine, the cells that divide are able to cross the crypt-villus boundary in their journey towards the villus tip. This discrepancy is most probably explained by the different expression pattern of Eph receptors and Ephrin ligands in the intestine versus the neural tube. In the neural tube, each rhombomere express either the Eph receptor or the complementary Ephrin ligand. Contrarily, in the intestine, Eph receptors and Ephrin ligands are expressed in counter gradients from the bottom of the crypt to the tip of the villus. This means that transit amplifying cells express both Eph receptors and Ephrin ligands and, thus, the boundary gets more permissive to movements across it. In mosaic monolayers of EphB and EphrinB expressing cells, the two populations do not form stable cell-cell adhesions and a physical empty space emerges at the boundary, as shown for MDCK[29], Hek293[318] or colorectal cancer cells[237]. However, and supporting the idea that the crypt-villus boundary is more permissive, no gaps in the monolayer are observed at the transit amplifying region in our organoids, indicating that cells form cell-cell adhesions.

Actin cable formation and increase in contractility at the crypt-villus boundary are probably due to Rho-Rock activation downstream of Eph/Ephrin signaling[28,239,319]. Importantly, in our organoids, this increase in contractility reshapes the basal surface of the transit amplifying cells, by pinching them and increasing their basal aspect ratio (Figure 38). For this basal reshaping to occur, the cells must probably decrease the adhesion to the substrate. In the *in vivo* epithelium, cells at the crypt-villus junction show a similar basal constriction[226]. In these cells, Rac1 activation inhibits hemidesmosomal adhesion to allow for basal reshaping of the cell surface. Interestingly, Rac1 activation has been shown to be crucial for Eph/Ephrin mediated cell sorting[242,243]. Given all this evidence, a plausible mechanism explaining crypt-villus boundary formation in intestinal organoids is that Eph/Ephrin signaling triggers both activation of RhoA - to induce actomyosin contractility - and activation of Rac1 – to reduce hemidesmosomal adhesion and allow for cell reshaping. To substantiate this hypothesis, we would need to evaluate the expression level of hemidesmosomes, Rac1 activation and RhoA activation along the crypt-villus axis and whether they are perturbed in EphB2/3 dKO organoids.

Strikingly, the proliferative compartment is larger in EphB2/3 dKO organoids. In line with these results, Eph/Ephrin downregulation correlates with an increase in crypt proliferation *in vivo*[320,321]. Other reports show, however, that Eph/Ephrin inhibition reduces proliferation[234,235]. Given these discrepancies, it will be worth re-assessing proliferation in EphB2/3 dKO tissues. Of note, we also need to assess whether the stem cell compartment, the transit amplifying region or both are enlarging. In any event, why does this enlargement occur? Different mechanisms - that are not mutually exclusive - could explain it. From one side, the observed scattering of Paneth cells in EphB2/3 dKO organoids might generate a broader Wnt gradient, providing proliferative signals to a larger area of the monolayer. In support of this idea, when Wnt3a is micropatterned on the substrate, crypt-like structures of open-lumen organoids accommodate their size to the Wnt3a area[204].

Recently, ERK waves have been shown to control the size of crypt-like domains in colon open-lumen organoids[322]. Extruding cells at the differentiated regions of open-lumen organoids generate an ERK activation wave that travels radially towards the crypt-like region[322]. The crypt like region, however, shows a reduced ERK activation, attributed to the inactivation of ERK by Wnt signaling[323,324]. Importantly, pharmacological inhibition of ERK signaling results in the enlargement of the stem cell compartment[322]. Eph/ephrin signaling induces ERK activation through the RAS pathway[319]. Thus, a decrease in ERK activity in EphB2/3 dKO organoids - either through a broader Wnt gradient or through a downregulation of the RAS pathway - might also explain the enlargement of the proliferative region that we observe.

Alternatively, or in combination, mechanotransduction pathways might be altered in EphB2/3 dKO organoids. For instance, the basal elongation of transit amplifying cells in wild type organoids might induce nuclear translocation of transcription factors such as YAP/TAZ through stretching of the nucleus and nuclear pore opening[59]. YAP/TAZ inactivation is proposed to induce an enlargement of the crypt-like regions in open-lumen organoids[309]. Conversely, YAP/TAZ activation regulates intestinal differentiation[252]. In the neural tube, the constriction of actomyosin cables at the boundary between rhombomeres downstream of Eph/Ephrin signaling induces nuclear translocation of YAP/TAZ, which then triggers cell differentiation[238]. Moreover, YAP/TAZ activation antagonizes Wnt signaling through the expression of Wnt inhibitors[325]. An appealing hypothesis is that basal relaxation at the crypt-villus boundary in EphB2/3 dKO organoids results in downregulation of YAP/TAZ signaling, which in turns causes a perturbation in cell differentiation and / or an increase in Wnt signaling and subsequent enlargement of the proliferative regions.

In the Drosophila neuroepithelium, perturbation of Eph/Ephrin signaling causes mitotic spindle misorientation and increase in proliferation[326]. Interestingly, intestinal stem cells deficient for the adenomatous polyposis coli gene (APC) – a tumor suppressor mutated in most colorectal cancers - show spindle misorientation[327,328]. Whether spindle misorientation might endow EphB2/3 dKO organoids with a malignant hyperproliferative phenotype is another exciting question to be addressed in the future.

Our circumferential laser cuts experiments revealed that the crypts are under tension. This result rules out mitotic pressure as the main mechanism driving crypt to villus migration, as crypts in that case should be under compression. High spatio-temporally resolved maps of cell velocities, cell-cell and cell-ECM forces suggested that the cells are dragged out of the crypt by a gradient of increasing tension at the villus-like region. *In vivo*, however, tension is higher at the bottom of the villus than at the top[261]. Given that the villus-like region in our organoids is shorter than the ~400 µm of the villus length *in vivo*[103,261], it is possible that the flat villus-like region of our open lumen organoids recapitulates only the bottom part of the villus. To understand this discrepancy, it would be interesting to measure 3D tractions and monolayer tension in scaffolded organoids with crypt and villus lengths similar to the *in vivo* situation. On a flat open-lumen organoid system similar to ours, intestinal subepithelial myofibroblasts (ISEMFs) have been shown to align and direct the motion of the intestinal epithelium during the closure of a gap[329]. In homeostatic conditions, ISEMFs might also have a mechanical role in the migration of cells from the crypt to the villus by aligning the migration of villus cells. In the future, to test this hypothesis, we could seed ISEMFs as a basal layer over polyacrylamide gels and grow the intestinal organoids on top.

In vivo, cells ascending from different crypts meet at the villus tip, generating a region of high cell density[261] . It has been proposed that compressive stresses due to this increase in cell density trigger cell extrusion, via mechanisms including Piezo-1 activation[67]. In our organoids, however, cells extrude at regions of low cell density and high cell spreading area, suggesting that other mechanisms than compression may be responsible for extrusion. Kocgozlu et al.[330] showed that attending to the cell density, epithelial cells experience different modes of cell extrusion. At high density, a contractile actomyosin ring squeezes the extruding cell out, while at low cell density, extrusion is mainly driven by the lamellipodial extension of neighboring cells. It may be thus possible that cells in the villus-like regions are extruding through different mechanisms depending on the local density of the tissue. Comet-shaped (+1/2) topological defects have been also shown to induce cell extrusion in epithelial monolayers[276]. We have not noticed such topological defects at the site of extrusions, although further investigation is warranted. Hence, the exact mode of extrusion followed by cells at the villus-like regions and whether this correlates with local density, cell type or apoptotic/non-apoptotic state of the cells is an exciting area for further study.

Overall, by quantitative force mapping in a physiologically relevant model of the intestinal epithelium, we uncover the paramount role of epithelial forces during crypt folding, crypt-villus compartmentalization and crypt-to-villus migration. With this experimental framework, the role of mechanics in other homeostatic and malignant processes such as differentiation, inflammation, regeneration, or cancer progression, is now accessible to experimental interrogation.

6 Conclusions

In light of the results presented and discussed throughout this thesis, we draw the following conclusions:

1. Open-lumen intestinal organoids self-organize into functional crypt-like and villus-like domains, allowing for quantitative force mapping at high spatio-temporal resolution.

2. Cell fate and tissue mechanics co-evolve in intestinal organoids to properly shape a mature epithelium.

3. Intestinal organoids exert a tightly regulated pattern of forces on the underlying substrate, defining mechanical and functional compartments.

4. The mechanical environment has a great impact on intestinal organoid architecture and cell fate. On softer substrates, crypts adopt a folded geometry, increase in size, and contain more stem cells.

5. The stem cell compartment pushes the substrate downwards and induce crypt folding through actomyosin-driven apical constriction of the stem cells.

6. The transit amplifying region pulls on the substrate by basally constricting, defining a mechanical boundary between the stem cell niche and the villus-like region.

7. Eph/Ephrin signaling regulates the basal constriction of transit amplifying cells and instructs proper cell positioning and crypt-villus compartmentalization. In EphB2/3 dKO organoids, the proliferative compartment enlarges, and Paneth cells are mispositioned.

8. Collective migration at the villus-like region drags cells out of the crypt along a gradient of increasing tension.

Contributions to the data presented in this thesis

The experiments in Figure 27, Figure 28, Figure 29, Figure 30, Figure 31, Figure 32, Figure 34, Figure 38, Figure 39, Figure 40 and Figure 51 were performed and analyzed by Gerardo Ceada and Carlos Pérez. The experiments in Figure 33, Figure 35, Figure 36, Figure 42, Figure 43, Figure 44 were performed and analyzed by Gerardo Ceada. Manuel Gómez developed codes to measure 3D Tractions (Fourier and Finite elements). Marija Matejčić performed the 3D segmentation (Figure 38, Figure 39 and Figure 40). Laser cuts experiments (Figure 37, Figure 52) and the *in vivo* measurements (Figure 45, Figure 46) were performed and analyzed by Carlos Pérez at the laboratory of Danijela Matic Vignjevic (Institut Curie, Paris). Venkata Ram Gannavarapu helped on the immunostainings in Figure 45 and Figure 46. The *in vivo* myosin data in Figure 45 was provided by Denis Krndija and Andrew G. Clark. Adrián Álvarez isolated Lgr5–eGFP-IRES-CreERT2 crypts for organoid culture at the laboratory of Eduard Batlle (IRB, Barcelona). The computational 3D vertex model and the Monolayer Stress Microscopy (Figure 39, Figure 41, Figure 51, Figure 52) were developed by Francesco Greco, Sohan Kale and Marino Arroyo at the laboratory of Marino Arroyo (UPC, Barcelona). The experiments in Figure 47 were performed and analyzed by Gerardo Ceada. EphB2/3 WT and EphB2/3 dKO mice were generated by Sergio Palomo at the laboratory of Eduard Batlle (IRB, Barcelona). Organoids from EphB2/3 WT and EphB2/3 dKO intestinal tissue were generated by Gerardo Ceada. Open-lumen EphB2/3 WT and EphB2/3 dKO organoid data (Figure 48, Figure 49) was generated by Gerardo Ceada with help from Clément Hallopeau. *In vivo* data of EphB2/3 WT and EphB2/3 dKO mice (Figure 50) was generated by Gerardo Ceada. All along the project we received experimental assistance from Natalia Castro and Anghara Menéndez.

7 Appendix

Appendix 1: Computational vertex model.

This model was developed by Francesco Greco, Sohan Kale and Marino Arroyo in Marino Arroyo's group at the UPC.

3D vertex model on a rigid substrate.

To understand the tissue mechanics leading to cell and monolayer morphology and to the mechanical coupling with the substrate, we developed a 3D computational vertex model. This model is based on a conventional effective energy or virtual work function of the form

$$\delta W = \sum_{c=1}^{N} \sum_{f=1}^{N_c} \gamma_{f,c} \delta A_{f,c}, \tag{1}$$

where N is the number of cells, N_c the number of faces of cell c, $\gamma_{f,c}$ the surface tension of face f of cell c, and $\delta A_{f,c}$ the variation of the surface area of that face. We assume that the surface tensions $\gamma_{f,c}$ remain constant during a simulation but are heterogeneous throughout the tissue. Work functionals for 3D vertex models can also account for the line tension generated by apical or basal cables. We also implemented such terms but found no essential differences for the purpose of this study, and hence we ignored them for the sake of simplicity.

To capture the cell shapes with curved junctions observed in the experiments, we discretized each cell with a triangulation as shown in Figure 53a. However, we did not account for cell rearrangements, which are easily dealt with in 2D but much more challenging in 3D. Thus, during tissue relaxation, cells maintain their prismatic topology and connectivity and can only change their shape. In the actual system, local junctional rearrangements may contribute to the tissue deformation[300].

Accounting for cell volume preservation, we can define an effective or pseudo-energy over the entire triangulation describing the tissue of the form[295–297]

$$W(\boldsymbol{x}_1,\ldots,\boldsymbol{x}_M)=\sum_{c=1}^{N}\sum_{f=1}^{N_c}\gamma_{f,c}A_{f,c}(\boldsymbol{x}_1,\ldots,\boldsymbol{x}_M)+\sum_{c=1}^{N}\frac{\kappa}{2}\left[V_c(\boldsymbol{x}_1,\ldots,\boldsymbol{x}_M)-V_{c,0}\right]^2 \qquad (2)$$

where x_i denotes the position of node i in this triangulation, V_c is the volume of cell c, and κ is an osmotic compressibility modulus that ensures that cell volumes remain fixed within 0.1% to the initial volume, $V_{c,0}$ for cell c.

We started our analysis by considering a planar tissue with cells of uniform shape and size as shown in Figure 53. To examine the mechanics of intestinal crypts, we prescribed a distribution of surface tensions that mimics the measured basal and apical F-actin distribution. It is known that cortical tension depends in a highly nontrivial way on the amount, but also the architecture, of cytoskeletal components. However, given the order of magnitude variations of F-actin accumulation in our crypts, it is reasonable to consider F-actin accumulation as a proxy for cortical tension in a first approximation. Noting that the F-actin distributions were measured on an actual deformed crypt and that we are prescribing surface tensions on an idealized undeformed tissue, we broadened the apical and basal peaks in F-actin distribution in our computer model. Regarding lateral surface tensions, we noted that the apical/basal surfaces of our monolayers were quite smooth at the intersections with lateral junctions. We reasoned that if lateral surface tensions were relatively large, then as a result of mechanical equilibrium at these intersections we should observe noticeable surface deformations at apico-lateral and baso-lateral intersections. Since these were absent, we concluded that lateral tensions should be significantly smaller than basal and apical tensions. We note in this regard that at lateral faces, adhesion tension acts as a negative surface tension that lowers the total lateral surface tension.

During our analysis, we kept fixed the distribution of surface tension over cell faces shown in Figure 53b. Given the high heterogeneity of this surface tension pattern, the initial regular cell monolayer is not in mechanical equilibrium. We then proceeded to the equilibration of the system on a rigid substrate. For this, we minimized the function in Eq. (2) using Newton's method to find the equilibrium positions of nodes in our triangulation. While our description of each cell face as a triangulated surface allows us to describe curved shapes, it also poses a numerical challenge as the distortion of our triangulations needs to be controlled during the numerical minimization. Indeed, since the function in Eq. (2) only depends on the surface area of each face and the volume of each cell, it is invariant with respect to tangential motions of internal nodes to each face that leave these geometric quantities unchanged, and thus does not provide any control of mesh distortion. To deal with this issue, we adopted the approach proposed elsewhere[331], which considers a fictitious surface hyperelastic model for each cell junction whose reference configuration is updated iteratively to the previously converged configuration. This fictitious elastic energy results in an effective viscosity of the cellular cortices and the algorithm can then be viewed as the dynamical relaxation of a viscous cell aggregate with active surface tensions and fixed cellular volumes. These dynamics control mesh distortions and upon convergence of the algorithm, the fictitious elastic energy vanishes and does not bias the final results.

In our simulations on rigid substrates, we allowed the nodes on the basal plane to slide tangentially but forced their z position to zero so that they stay on the plane of the substrate. Furthermore, we fixed the lateral edges of the tissue. Upon equilibration, we found the tissue and cellular shapes and the normal tractions, Figure 53c. As the tissue deformed, the pattern of surface tensions more closely followed the experimentally measured patterns of F-actin distribution.

3D vertex model on a deformable substrate

We then placed the equilibrated crypt in contact with a highly deformable elastic substrate. We modeled the substrate using finite deformation continuum mechanics and a NeoHookean hyperelastic model, for which the strain energy density per unit undeformed volume is given by[332]

$$\psi(\boldsymbol{C}) = \frac{\lambda}{2}(\ln J)^2 - \mu \ln J + \frac{\mu}{2}(\text{trace } \boldsymbol{C} - 3)\,, \tag{3}$$

where $\boldsymbol{C} = \boldsymbol{F}^T\boldsymbol{F}$ is the right Cauchy-Green deformation tensor, F is the deformation gradient, $J = \sqrt{detC}$ is the Jacobian determinant and λ and μ are the Lamé coefficients at infinitesimal deformations. These coefficients are related to infinitesimal Young's modulus E and Poisson's ratio ν by the relations $\lambda = E\nu / [(1 + \nu)(1 - 2\nu)]$ and $\mu = E / (1 + \nu)$. We discretized the deformable substrate with linear tetrahedral finite elements. The bulk tetrahedral mesh was generated to be conforming in its top plane to the surface triangulation of the basal plane of the tissue equilibrated on a rigid substrate. We imposed kinematical compatibility at the cell-matrix interface by identifying the basal nodes of the tissue triangulation to the corresponding nodes of the matrix mesh. We then further equilibrated the joint tissue-matrix system by minimizing the joint effective energy given by

$$W + \int_{\Omega_0} \psi(\boldsymbol{C}) \, dV, \tag{4}$$

where Ω_0 is the domain representing the substrate, with respect to the positions of the nodes of the tissue triangulation and of the bulk finite element mesh. This minimization was again performed using Newton's method with a line-search. As a result, the crypt was able to deform the substrate, Figure 53d.

Sensitivity to the pattern of active tensions

We simulated tens of computational crypts with patterns of cellular surface tensions following the measured F-actin distribution. We found a very robust agreement with the main features of the experiments in terms of tissue shape in stiff and soft substrate, of cellular shapes and of normal traction. However, the details of these observables depended on the specific pattern of surface tensions. By way of an illustration of this sensitivity, we report in Figure 54d the tissue morphology and normal tractions for two models with significantly different distribution of basal surface tensions. When basal tension is increased, we observe that the peak of positive normal tractions is smaller, and that the indentation on soft gels is smaller since tension works against the extension of the basal surface required for bending. However, both models recapitulate the essential features of the actual crypts. In Figure 54a we report the pattern of surface tensions used to produce the results in Figure 39. We also illustrate the procedure to filter the normal tractions in the simulations, Figure 54b, and the finite element mesh used to model the substrate, Figure 54c.

Estimation of the maximum apical surface tension

The length-scale of the model is fixed by the typical size of cells and height of the typical crypt. Given this length-scale, $\gamma_{\max}$, Figure 53b and Figure 54a, sets the force-scale in the model, and hence the units of the computational normal tractions. By comparing the normal tractions in the simulations and in the experiments, we can scale the force scale in our model and hence attach physical units to the surface tensions. This allows us to estimate the magnitude of the surface tensions. By focusing on the normal traction data in Figure 34G and its standard deviation, we find that $\gamma_{\max}$ ~ 4.6 mN/m with a standard deviation of 1.7 mN/m. This cellular surface tension is about two times larger than surface tensions measured in suspended cells during mitosis[333]. We note that apical actin cables could contribute to this effective apical surface tension.

Simulating laser cuts

To simulate laser cuts and starting from a previously equilibrated system, we instantaneously imposed nearly zero surface tension in the finite elements lying in the cut region. By removing the mechanical effect of the cut region, the internal force balance of the system is broken and it will move to regain a new state of equilibrium. In theoretical models of tissue recoil, the instantaneous recoil depends on pre-existing tension (irrespective of its origin, active or elastic) and on an effective viscosity. The detailed modelling of the viscosity of the different structural elements of the tissue is complex and beyond the scope of the present work. However, by taking advantage of the viscosity intrinsic to our algorithm described above[331], we could predict the recoil velocity pattern (but not the physical magnitude of these velocities) from the model displacements in the first iterations. To post-process the results in Figure 39 and Figure 52, we represented the displacements of the nodes in the apical plane after the first iteration.

Basal elongation in the transit amplifying zone

Despite introducing a peak of basal surface tension in the transit amplifying zone, consistent with our quantification of F-actin distribution, our computational model did reproduce some degree of basal elongation, but not nearly as marked as in actual crypts, Figure 39I,N. Imaging of cytoskeletal components in this region (Figure 36) clearly showed strongly aligned supra-cellular structures, which can likely influence the active force generation since active tension is expected along these aligned structures, but also bundling active forces may act perpendicular to those structures. All surface tensions being isotropic in our model, it likely misses some mechanical aspects of the basal plane in the transit amplifying region, which may explain the extreme elongation of cells.

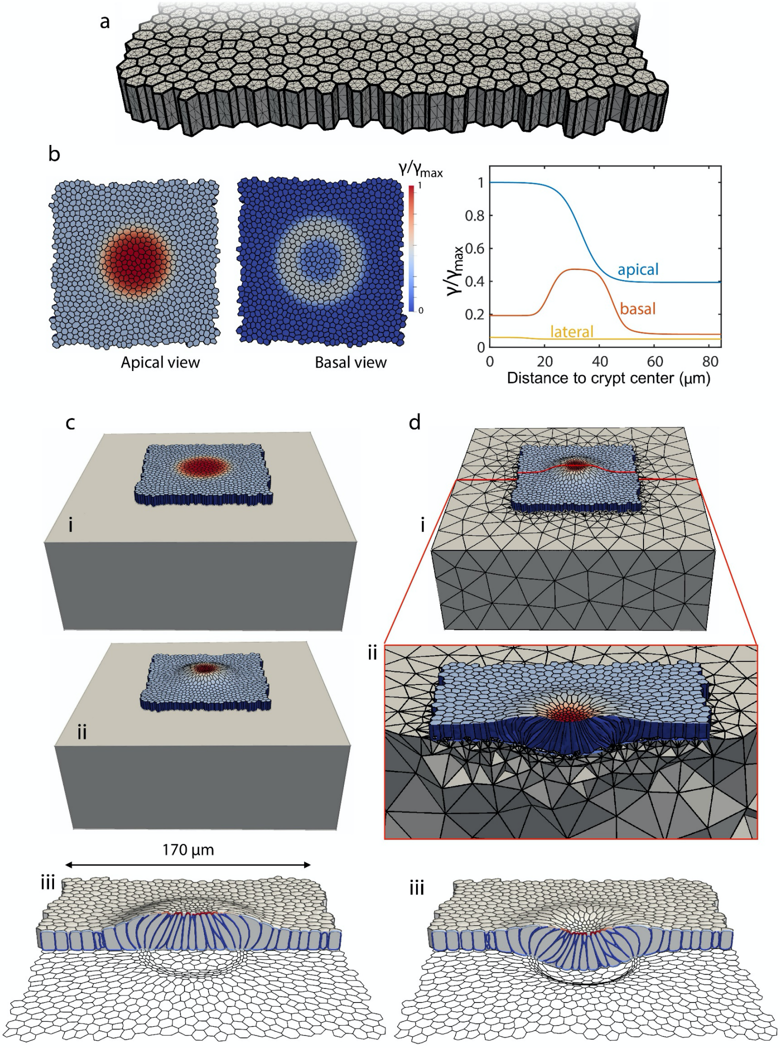
a
b
γ/γmax
1
0
Apical view
Basal view
1
0.8
0.6
0.4
0.2
0
γ/γmax
apical
basal
lateral
0
20
40
60
80
Distance to crypt center (μm)
c
d
i
ii
170 μm
iii

Figure 53. 3D computational vertex model and simulation protocol. **a**, Discretization of the tissue: the thick lines denote the intersection between cellular faces and the thin lines the triangulation of the cell surfaces. **b**, Pattern of apical, basal and lateral surface tensions prescribed in the initial regular cell monolayer. **c**, Equilibration of the initial regular monolayer with patterned surface tensions on a rigid substrate, where basal nodes are constrained to a plane but can slide horizontally. Initial state (i), equilibrated state (ii), and different view of equilibrated state with basal cell outline (iii). **d**, Coupling with a deformable substrate, modelled computationally with a tetrahedral mesh discretizing a hyperelastic block (i). The equilibrated crypt on a rigid substrate (**c**-ii) is further equilibrated on the deformable substrate (**d**-ii,iii).

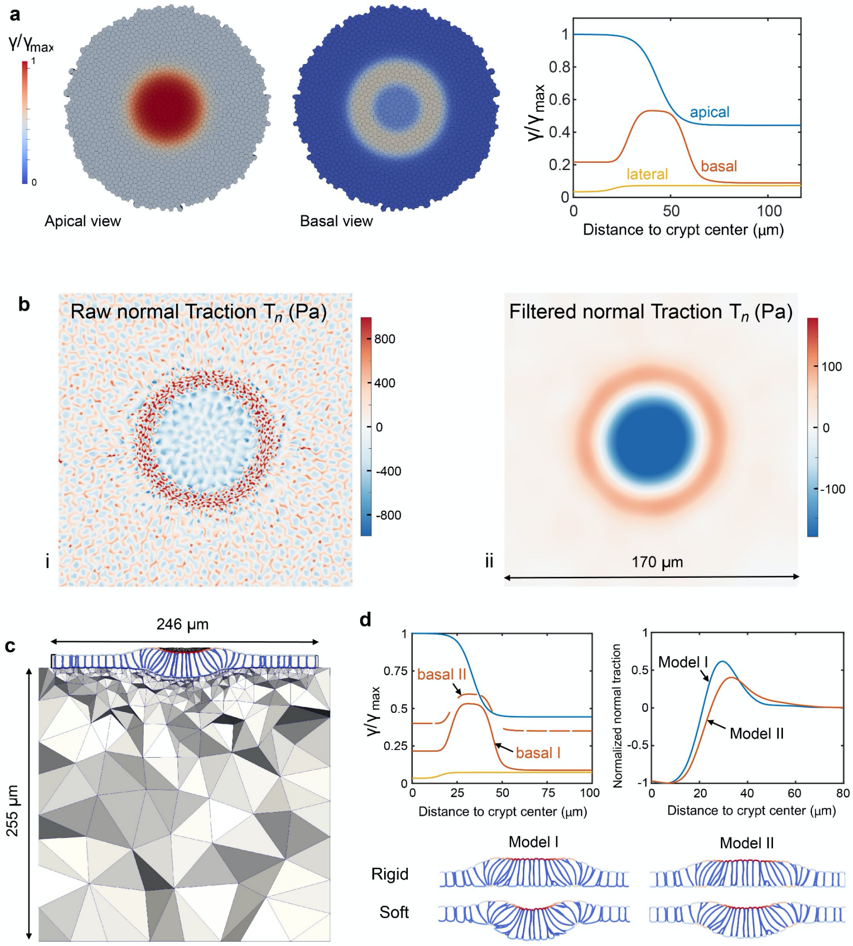

Figure 54. Simulation of crypt normal tractions. **a**, Pattern of apical, basal and lateral surface tensions prescribed in the initial regular cell monolayer. **b**, Maps of basal normal traction. (i) Raw normal tractions at the basal plane featuring sub-cellular fine-scale details. To compare with experimental averages, we filtered these tractions with a Gaussian filter with standard deviation of 6 μm, (ii). **c**, Computational model of the deformed crypt on a soft hyperelastic substrate. **d**, Crypt folding for two models with different basal tension profiles on soft and rigid substrates.

Appendix 2: Axisymmetric Monolayer Stress Microscopy

This was developed by Francesco Greco and Marino Arroyo in Marino Arroyo's group at the UPC.

We describe here a simple approach for Monolayer Stress Microscopy (MSM), that is to infer the tissue surface stress from the measured tractions, in an axisymmetric configuration pertinent to the analysis of our crypts. The starting variable is then the radially-averaged tangential traction T_r, Figure 31D.

Background

We consider polar coordinates given by $x(r,\theta) = r\cos\theta$ and $y(r,\theta) = r\sin\theta$. The natural basis is given by $x_r(r,\theta) = (\cos\theta, \sin\theta)$ and $x_\theta(r,\theta) = (-r\sin\theta, r\cos\theta)$. Hence the metric tensor is given by

$$\{g_{ab}\} = \begin{pmatrix} 1 & 0 \\ 0 & r^2 \end{pmatrix}, \qquad \{g^{ab}\} = \begin{pmatrix} 1 & 0 \\ 0 & 1/r^2 \end{pmatrix}.$$

The corresponding Christoffel symbols are

$$\{\Gamma^r_{ab}\} = \begin{pmatrix} 0 & 0 \\ 0 & -r \end{pmatrix}, \qquad \{\Gamma^\theta_{ab}\} = \begin{pmatrix} 0 & 1/r \\ 1/r & 0 \end{pmatrix}.$$

Therefore, using standard formulae in differential geometry, we can compute the covariant derivative of a radial vector field $u(r,\theta) = u(r)\, x_r(r,\theta)$ as

$$\{u^a{}_{|b}\} = \begin{pmatrix} u' & 0 \\ 0 & u/r \end{pmatrix}.$$

The symmetrized displacement gradient is the small-strain tensor, which thus takes the form

$$\{\varepsilon_{ab}\} = \begin{pmatrix} u' & 0 \\ 0 & ur \end{pmatrix}, \qquad \{\varepsilon^{ab}\} = \begin{pmatrix} u' & 0 \\ 0 & u/r^3 \end{pmatrix},$$

and its trace is

$$\text{tr}\ \boldsymbol{\varepsilon} = \varepsilon^a{}_a = u' + u/r.$$

Consider a stress tensor in axisymmetry, and thus of the form

$$\{\sigma^{ab}\} = \begin{pmatrix} \sigma^{rr}(r) & 0 \\ 0 & \sigma^{\theta\theta}(r) \end{pmatrix}.$$

The radial component of its divergence $\sigma^{ab}{}_{|b}$ can be written as

$$\sigma^{rb}{}_{|b} = \partial_r \sigma^{rr} + \frac{1}{r}\left(\sigma^{rr} - r^2\sigma^{\theta\theta}\right) = \partial_r \sigma^r{}_r + \frac{1}{r}\left(\sigma^r{}_r - \sigma^\theta{}_\theta\right) \tag{5}$$

Consider now linear elastic constitutive relation

$$\boldsymbol{\sigma} = 2\mu\boldsymbol{\varepsilon} + \lambda(\mathrm{tr}\ \boldsymbol{\varepsilon})\boldsymbol{g}.$$

Using the equations above, we find

$$\sigma^r{}_r = \sigma^{rr} = (2\mu + \lambda)u' + \lambda\frac{u}{r}, \tag{6}$$

and

$$\sigma^\theta{}_\theta = r^2\sigma^{\theta\theta} = (2\mu + \lambda)\frac{u}{r} + \lambda u', \tag{7}$$

and we obtain its radial divergence as

$$(\mathrm{div}\ \boldsymbol{\sigma})_r = \left[(2\mu + \lambda)u' + \lambda\frac{u}{r}\right]' + \frac{2\mu}{r}\left(u' - \frac{u}{r}\right).$$

If material properties are uniform, then we obtain

$$(\mathrm{div}\ \boldsymbol{\sigma})_r = (2\mu + \lambda)\left(u'' + \frac{u'}{r} - \frac{u}{r^2}\right).$$

Monolayer Stress Microscopy

The tissue modeled as a 2D continuous medium is initially in an axisymmetric state of mechanical equilibrium characterized by a stress $\boldsymbol{\sigma}$. The equilibrium condition can be expressed as

$$(\mathrm{div}\ \boldsymbol{\sigma})_r = \partial_r \sigma^r{}_r + \frac{1}{r}\left(\sigma^r{}_r - \sigma^\theta{}_\theta\right) = T_r, \tag{8}$$

where T_r are the measured radial tractions exerted by cells on the substrate. Thus, we have one equation for two unknowns, ${\sigma^r}_r$ and ${\sigma^\theta}_\theta$. One standard way to proceed is then to assume a constitutive relation, e.g. linear elasticity[36], leading to

$$\left[(2\mu + \lambda)u' + \lambda\frac{u}{r}\right]' + \frac{2\mu}{r}\left(u' - \frac{u}{r}\right) = T_r \tag{9}$$

or if mechanical properties are assumed to be constant to

$$(2\mu + \lambda)\left(u'' + \frac{u'}{r} - \frac{u}{r^2}\right) = T_r, \tag{10}$$

which, along with boundary conditions $u(0) = 0$ and $u(r^\infty) = U$ allow us to find the auxiliary displacement $u(r)$. The boundary condition at a far away location $u(r^\infty) = U$ only fixes the undetermined hydrostatic and uniform state of tension σ_0, and is thus arbitrary unless an independent measurement is available. Finally, recalling Eqs. (6,7) we obtain the sought-after tension as

$$\begin{aligned} {\sigma^r}_r &= \sigma_0 + (2\mu + \lambda)u' + \lambda\frac{u}{r}, && (11)\\ {\sigma^\theta}_\theta &= \sigma_0 + (2\mu + \lambda)\frac{u}{r} + \lambda u'. && (12) \end{aligned}$$

The quantity ${\sigma^r}_r$ is the radial tension reported in Figure 51, whereas ${\sigma^\theta}_\theta$ is a hoop tension.

We lack an independent measurement to determine σ_0 but our laser cuts indicate that radial tension is positive where it is minimum, at the transit amplifying zone. Therefore, in our calculations of MSM reported in Figure 51 we chose σ_0 so that the minimum radial tension is zero with the understanding that there should be a positive offset to this curve.

Given T_r, we solve Eq. (9) using 1D finite elements. For this, we multiply Eq. (9) by a test function w, integrate over the domain $(0, R_{\text{out}})$ noting that $dS = 2\pi r dr$, and integrate by parts, to obtain

$$\int_0^{R_{\text{out}}} (2\mu + \lambda)u'w'r dr + \int_0^{R_{\text{out}}} \frac{2\mu + \lambda}{r} uw dr + \int_0^{R_{\text{out}}} \lambda\left(vw' + v'w\right) dr = -\int_0^{R_{\text{out}}} T_r w r dr.$$

Approximating the unknown with finite element basis function $u(r) = \sum_{J=1}^{M} N(r) u_J$ and taking the test functions to be $w(r) = N_I(r)$, we find the following algebraic system of equations

$$\sum_{J=1}^{M} K_{IJ} u_J = F_I,$$

imposing the constraints that $u_1 = 0$ and $u_M = U$ and where

$$K_{IJ} = \int_0^{R_{\text{out}}} (2\mu + \lambda) N_I' N_J' r dr + \int_0^{R_{\text{out}}} \frac{2\mu + \lambda}{r} N_I N_J dr + \int_0^{R_{\text{out}}} \lambda \left(N_I N_J' + N_I' N_J \right) dr$$

and

$$F_I = \int_0^{R_{\text{out}}} T_r N_I r dr.$$

In the calculations reported in Figure 51, we chose $\lambda = 10\mu$. We checked that the inferred tensions were largely insensitive to the choice of material parameter provided that $\lambda \gtrsim 3\mu$. Since the crypt is bound to have very different material properties than the rest of the tissue, we tested the sensitivity of the recovered tensions to heterogeneous elastic constants. For this, we chose λ and μ to be 10 and 20 times larger in the crypt than in the rest of the tissue. The results were again insensitive.

8 References

1. Pérez-González, C. *et al.* Mechanical compartmentalization of the intestinal organoid enables crypt folding and collective cell migration. *Nat Cell Biol* **23**, 745–757 (2021).
2. Betts, J. G. *et al. Anatomy and physiology*. (Rice University, 2013).
3. Brugués, A. *et al.* Forces driving epithelial wound healing. *Nat Phys* **10**, 683–690 (2014).
4. Behrndt, M., Roensch, J., Grill, S. W. & Heisenberg, C. Forces Driving Epithelial Spreading in Zebrafish Gastrulation. *Science* **338**, 257–260 (2012).
5. What is the cytoskeleton? *National University of Singapore* https://www.mechanobio.info/cytoskeleton-dynamics/what-is-the-cytoskeleton/ (2018).
6. Pegoraro, A. F., Janmey, P. & Weitz, D. A. Mechanical properties of the cytoskeleton and cells. *Cold Spring Harb Perspect Biol* **9**, a022038 (2017).
7. Goodson, H. V & Jonasson, E. M. Microtubules and Microtubule-Associated Proteins. *Cold Spring Harb Perspect Biol* **10**, a022608 (2018).
8. Fuchs, E. & Weber, K. Intermediate filaments: Structure, dynamics, function, and disease. *Annu Rev Biochem* **63**, 345–382 (1994).
9. Dutour-Provenzano, G. & Etienne-Manneville, S. Intermediate filaments. *Current Biology* **31**, R522–R529 (2021).
10. Kreplak, L., Bär, H., Leterrier, J. F., Herrmann, H. & Aebi, U. Exploring the mechanical behavior of single intermediate filaments. *J Mol Biol* **354**, 569–577 (2005).
11. Latorre, E. *et al.* Active superelasticity in three-dimensional epithelia of controlled shape. *Nature* **563**, 203–208 (2018).
12. Kechagia, Z., Sáez, P., Gómez-gonzález, M., Zamarbide, M. & Andreu, I. The laminin-keratin link shields the nucleus from mechanical deformation and signalling. *bioRxiv* (2022) doi:10.1101/2022.03.01.482474.
13. Hu, J. *et al.* High stretchability, strength, and toughness of living cells enabled by hyperelastic vimentin intermediate filaments. *Proc Natl Acad Sci U S A* **116**, 17175–17180 (2019).
14. Vicente-Manzanares, M., Ma, X., Adelstein, R. S. & Horwitz, A. R. Non-muscle myosin II takes centre stage in cell adhesion and migration. *Nat Rev Mol Cell Biol* **10**, 778–790 (2009).
15. Svitkina, T. The actin cytoskeleton and actin-based motility. *Cold Spring Harb Perspect Biol* **10**, 1–21 (2018).
16. Murthy, K. & Wadsworth, P. Myosin-II-dependent localization and dynamics of F-actin during cytokinesis. *Current Biology* **15**, 724–731 (2005).
17. Buckley, I. K. & Porter, K. R. Cytoplasmic fibrils in living cultured cells. *Protoplasma* **64**, 349–380 (1967).
18. Burridge, K. & Wittchen, E. S. The tension mounts: Stress fibers as force-generating mechanotransducers. *Journal of Cell Biology* **200**, 9–19 (2013).
19. Hirokawa, N., Keller, T. C. S., Chasan, R. & Mooseker, M. S. Mechanism of brush border contractility studied by the quick-freeze, deep-etch method. *Journal of Cell Biology* **96**, 1325–1336 (1983).
20. Kovacs, E. M. *et al.* N-WASP regulates the epithelial junctional actin cytoskeleton through a non-canonical post-nucleation pathway. *Nat Cell Biol* **13**, 934–943 (2011).
21. Mooseker, M. S. & Tilney, L. G. Organization of an actin filament-membrane complex: Filament polarity and membrane attachment in the microvilli of intestinal epithelial cells. *Journal of Cell Biology* **67**, 725–743 (1975).
22. Albrecht-Buehler, G. Filopodia of spreading 3T3 cells: Do they have a substrate-exploring function? *Journal of Cell Biology* **69**, 275–286 (1976).

23. Nemethova, M., Auinger, S. & Small, J. V. Building the actin cytoskeleton: Filopodia contribute to the construction of contractile bundles in the lamella. *Journal of Cell Biology* **180**, 1233–1244 (2008).
24. Chugh, P. & Paluch, E. K. The actin cortex at a glance. *J Cell Sci* **131**, 1–9 (2018).
25. Abercrombie, M., Joan, E., Heaysman, M. & Pegrum, S. M. The locomotion of fibroblasts in culture. II. 'Ruffling'. *Exp Cell Res* **60**, 437–444 (1970).
26. Svitkina, T. M., Verkhovsky, A. B., McQuade, K. M. & Borisy, G. G. Analysis of the actin-myosin II system in fish epidermal keratocytes: Mechanism of cell body translocation. *Journal of Cell Biology* **139**, 397–415 (1997).
27. How are actin filaments distributed in cells and tissues? *National University of Singapore* https://www.mechanobio.info/cytoskeleton-dynamics/what-is-the-cytoskeleton/what-are-actin-filaments/how-are-actin-filaments-distributed-in-cells-and-tissues/ (2018).
28. Kindberg, A. A. *et al.* EPH/EPHRIN regulates cellular organization by actomyosin contractility effects on cell contacts. *J Cell Biol* **220**, (2021).
29. Rodriguez-Franco, P. *et al.* Long-lived force patterns and deformation waves at repulsive epithelial boundaries. *Nat Mater* **16**, 1029–1036 (2017).
30. Lambert, A. W. & Weinberg, R. A. Linking EMT programmes to normal and neoplastic epithelial stem cells. *Nat Rev Cancer* **21**, 325–338 (2021).
31. Zihni, C., Mills, C., Matter, K. & Balda, M. S. Tight junctions: From simple barriers to multifunctional molecular gates. *Nat Rev Mol Cell Biol* **17**, 564–580 (2016).
32. Rübsam, M. *et al.* Adherens junctions and desmosomes coordinate mechanics and signaling to orchestrate tissue morphogenesis and function: An evolutionary perspective. *Cold Spring Harb Perspect Biol* **10**, 1–21 (2018).
33. Gumbiner, B. M. Regulation of cadherin-mediated adhesion in morphogenesis. *Nat Rev Mol Cell Biol* **6**, 622–634 (2005).
34. Ladoux, B. & Mège, R. M. Mechanobiology of collective cell behaviours. *Nat Rev Mol Cell Biol* **18**, 743–757 (2017).
35. Trepat, X. *et al.* Physical forces during collective cell migration. *Nat Phys* **5**, 426–430 (2009).
36. Tambe, D. T. *et al.* Collective cell guidance by cooperative intercellular forces. *Nat Mater* **10**, 469–475 (2011).
37. Vasioukhin, V., Bowers, E., Bauer, C., Degenstein, L. & Fuchs, E. Desmoplakin is essential for epidermal sheet formation. *Nat Cell Biol* **3**, 1076–1085 (2001).
38. Price, A. J. *et al.* Mechanical loading of desmosomes depends on the magnitude and orientation of external stress. *Nat Commun* **9**, 5284 (2018).
39. Goodenough, D. A. & Paul, D. L. Gap Junctions. *Cold Spring Harb Perspect Biol* **1**, a002576 (2009).
40. Hynes, R. O. The evolution of metazoan extracellular matrix. *Journal of Cell Biology* **196**, 671–679 (2012).
41. Kreplak, L. & Fudge, D. Biomechanical properties of intermediate filaments: From tissues to single filaments and back. *BioEssays* **29**, 26–35 (2007).
42. Jayadev, R. & Sherwood, D. R. Basement membranes. *Current Biology* **27**, R207–R211 (2017).
43. Ohashi, K., Fujiwara, S. & Mizuno, K. Roles of the cytoskeleton, cell adhesion and rho signalling in mechanosensing and mechanotransduction. *J Biochem* **161**, 245–254 (2017).
44. Kanchanawong, P. *et al.* Nanoscale architecture of integrin-based cell adhesions. *Nature* **468**, 580–584 (2010).

45. Fontao, L., Stutzmann, J., Gendry, P. & Launay, J. F. Regulation of the type II hemidesmosomal plaque assembly in intestinal epithelial cells. *Exp Cell Res* **250**, 298–312 (1999).
46. Walko, G., Castañón, M. J. & Wiche, G. Molecular architecture and function of the hemidesmosome. *Cell Tissue Res* **360**, 529–544 (2015).
47. Herrmann, H., Bär, H., Kreplak, L., Strelkov, S. V. & Aebi, U. Intermediate filaments: From cell architecture to nanomechanics. *Nat Rev Mol Cell Biol* **8**, 562–573 (2007).
48. Yao, M. *et al.* Mechanical activation of vinculin binding to talin locks talin in an unfolded conformation. *Sci Rep* **4**, 4610 (2014).
49. Del Rio, A. *et al.* Stretching single talin rod molecules activates vinculin binding. *Science* **323**, 638–641 (2009).
50. Yao, M. *et al.* Force-dependent conformational switch of α -catenin controls vinculin binding. *Nat Commun* **5**, 4525 (2014).
51. Yonemura, S., Wada, Y., Watanabe, T., Nagafuchi, A. & Shibata, M. α-Catenin as a tension transducer that induces adherens junction development. *Nat Cell Biol* **12**, 533–542 (2010).
52. Ciobanasu, C., Faivre, B. & Le Clainche, C. Actomyosin-dependent formation of the mechanosensitive talin-vinculin complex reinforces actin anchoring. *Nat Commun* **5**, 3095 (2014).
53. Buckley, C. D. *et al.* The minimal cadherin-catenin complex binds to actin filaments under force. *Science* **346**, 1254211 (2014).
54. Hirata, H., Tatsumi, H., Lim, C. T. & Sokabe, M. Force-dependent vinculin binding to talin in live cells: A crucial step in anchoring the actin cytoskeleton to focal adhesions. *Am J Physiol Cell Physiol* **306**, C607–C620 (2014).
55. Choquet, D., Felsenfeld, D. P. & Sheetz, M. P. Extracellular matrix rigidity causes strengthening of integrin- cytoskeleton linkages. *Cell* **88**, 39–48 (1997).
56. Elosegui-Artola, A. *et al.* Mechanical regulation of a molecular clutch defines force transmission and transduction in response to matrix rigidity. *Nat Cell Biol* **18**, 540–548 (2016).
57. Dasgupta, I. & McCollum, D. Control of cellular responses to mechanical cues through YAP/TAZ regulation. *Journal of Biological Chemistry* **294**, 17693–17706 (2019).
58. Driscoll, T. P., Cosgrove, B. D., Heo, S. J., Shurden, Z. E. & Mauck, R. L. Cytoskeletal to Nuclear Strain Transfer Regulates YAP Signaling in Mesenchymal Stem Cells. *Biophys J* **108**, 2783–2793 (2015).
59. Elosegui-Artola, A. *et al.* Force Triggers YAP Nuclear Entry by Regulating Transport across Nuclear Pores. *Cell* **171**, 1397-1410.e14 (2017).
60. Si, Y. *et al.* Src Inhibits the hippo tumor suppressor pathway through tyrosine phosphorylation of Lats1. *Cancer Res* **77**, 4868–4880 (2017).
61. Hu, J. K. H. *et al.* An FAK-YAP-mTOR Signaling Axis Regulates Stem Cell-Based Tissue Renewal in Mice. *Cell Stem Cell* **21**, 91-106.e6 (2017).
62. Sabra, H. *et al.* β1 integrin–dependent Rac/group I PAK signaling mediates YAP activation of Yes-associated protein 1 (YAP1) via NF2/merlin. *Journal of Biological Chemistry* **292**, 19179–19197 (2017).
63. Ibar, C. *et al.* Tension-dependent regulation of mammalian Hippo signaling through LIMD1. *J Cell Sci* **131**, jcs214700 (2018).
64. Dutta, S. *et al.* TRIP6 inhibits Hippo signaling in response to tension at adherens junctions. *EMBO Rep* **19**, 337–350 (2018).
65. Venturini, V. *et al.* The nucleus measures shape changes for cellular proprioception to control dynamic cell behavior. *Science* **370**, eaba2644 (2020).

66. Lomakin, A. J. *et al.* The nucleus acts as a ruler tailoring cell responses to spatial constraints. *Science* **370**, eaba2894 (2020).
67. Eisenhoffer, G. T. *et al.* Crowding induces live cell extrusion to maintain homeostatic cell numbers in epithelia. *Nature* **484**, 546–549 (2012).
68. Gudipaty, S. A. & Rosenblatt, J. Epithelial cell extrusion: Pathways and pathologies. *Semin Cell Dev Biol* **67**, 132–140 (2017).
69. Gudipaty, S. A. *et al.* Mechanical stretch triggers rapid epithelial cell division through Piezo1. *Nature* **543**, 118–121 (2017).
70. Tozluoglu, M. & Mao, Y. On folding morphogenesis, a mechanical problem. *Philosophical Transactions of the Royal Society B: Biological Sciences* **375**, (2020).
71. Sawyer, J. M. *et al.* Apical constriction: A cell shape change that can drive morphogenesis. *Dev Biol* **341**, 5–19 (2010).
72. Martin, A. C. & Goldstein, B. Apical constriction: Themes and variations on a cellular mechanism driving morphogenesis. *Development (Cambridge)* **141**, 1987–1998 (2014).
73. Mason, F. M., Tworoger, M. & Martin, A. C. Apical domain polarization localizes actin-myosin activity to drive ratchet-like apical constriction. *Nat Cell Biol* **15**, 926–936 (2013).
74. Leptin, M. & Grunewald, B. Cell shape changes during gastrulation in Drosophila. *Development* **110**, 73–84 (1990).
75. Costa, M., Wilson, E. T. & Wieschaus, E. A putative cell signal encoded by the folded gastrulation gene coordinates cell shape changes during Drosophila gastrulation. *Cell* **76**, 1075–1089 (1994).
76. Sweeton, D., Parks, S., Costa, M. & Wieschaus, E. Gastrulation in Drosophila: The formation of the ventral furrow and posterior midgut invaginations. *Development* **112**, 775–789 (1991).
77. Martin, A. C. The physical mechanisms of Drosophila gastrulation: Mesoderm and endoderm invagination. *Genetics* **214**, 543–560 (2020).
78. Vijayraghavan, D. S. & Davidson, L. A. Mechanics of neurulation: From classical to current perspectives on the physical mechanics that shape, fold, and form the neural tube. *Birth Defects Res* **109**, 153–168 (2017).
79. Inoue, Y. *et al.* Mechanical roles of apical constriction, cell elongation, and cell migration during neural tube formation in Xenopus. *Biomech Model Mechanobiol* **15**, 1733–1746 (2016).
80. Haigo, S. L., Hildebrand, J. D., Harland, R. M. & Wallingford, J. B. Shroom Induces Apical Constriction and Is Required for Hingepoint Formation during Neural Tube Closure. *Current Biology* **13**, 2125–2137 (2003).
81. Christodoulou, N. & Skourides, P. A. A. Cell-Autonomous Ca2+ Flashes Elicit Pulsed Contractions of an Apical Actin Network to Drive Apical Constriction during Neural Tube Closure. *Cell Rep* **13**, 2189–2202 (2015).
82. Lang, R. A., Herman, K., Reynolds, A. B., Hildebrand, J. D. & Plageman, T. F. p120-catenin-dependent junctional recruitment of Shroom3 is required for apical constriction during lens pit morphogenesis. *Development (Cambridge)* **141**, 3177–3187 (2014).
83. Plageman, T. F. *et al.* Pax6-dependent Shroom3 expression regulates apical constriction during lens placode invagination. *Development* **137**, 405–415 (2010).
84. Plageman, T. F. *et al.* A trio-rhoA-shroom3 pathway is required for apical constriction and epithelial invagination. *Development* **138**, 5177–5188 (2011).

85. Borges, R. M., Lamers, M. L., Forti, F. L., dos Santos, M. F. & Yan, C. Y. I. Rho signaling pathway and apical constriction in the early lens placode. *Genesis* **49**, 368–379 (2011).
86. Krueger, D., Tardivo, P., Nguyen, C. & De Renzis, S. Downregulation of basal myosin- II is required for cell shape changes and tissue invagination . *EMBO J* **37**, 1–16 (2018).
87. Varner, V. D. & Nelson, C. M. Cellular and physical mechanisms of branching morphogenesis. *Development (Cambridge)* **141**, 2750–2759 (2014).
88. Monier, B. *et al.* Apico-basal forces exerted by apoptotic cells drive epithelium folding. *Nature* **518**, 245–248 (2015).
89. Manjón, C., Sánchez-Herrero, E. & Suzanne, M. Sharp boundaries of Dpp signalling trigger local cell death required for Drosophila leg morphogenesis. *Nat Cell Biol* **9**, 57–63 (2007).
90. Takeda, M., Sami, M. M. & Wang, Y. C. A homeostatic apical microtubule network shortens cells for epithelial folding via a basal polarity shift. *Nat Cell Biol* **20**, 36–45 (2018).
91. Wang, Y. C., Khan, Z., Kaschube, M. & Wieschaus, E. F. Differential positioning of adherens junctions is associated with initiation of epithelial folding. *Nature* **484**, 390–393 (2012).
92. Sidhaye, J. & Norden, C. Concerted action of neuroepithelial basal shrinkage and active epithelial migration ensures efficient optic cup morphogenesis. *Elife* **6**, 1–29 (2017).
93. Nicolás-Pérez, M. *et al.* Analysis of cellular behavior and cytoskeletal dynamics reveal a constriction mechanism driving optic cup morphogenesis. *Elife* **5**, 1–24 (2016).
94. Martinez-Morales, J. R. *et al.* Ojoplano-mediated basal constriction is essential for optic cup morphogenesis. *Development* **136**, 2165–2175 (2009).
95. Bogdanović, O. *et al.* Numb/Numbl-Opo Antagonism Controls Retinal Epithelium Morphogenesis by Regulating Integrin Endocytosis. *Dev Cell* **23**, 782–795 (2012).
96. Gutzman, J. H., Graeden, E. G., Lowery, L. A., Holley, H. S. & Sive, H. Formation of the zebrafish midbrain-hindbrain boundary constriction requires laminin-dependent basal constriction. *Mech Dev* **125**, 974–983 (2008).
97. Gutzman, J. H. *et al.* Basal constriction during midbrain–hindbrain boundary morphogenesis is mediated by Wnt5b and focal adhesion kinase. *Biol Open* **7**, (2018).
98. Chung, S., Kim, S. & Andrew, D. J. Uncoupling apical constriction from tissue invagination. *Elife* **6**, 1–25 (2017).
99. Guo, H., Swan, M. & He, B. Optogenetic inhibition of actomyosin reveals mechanical bistability of the mesoderm epithelium during Drosophila mesoderm invagination. *Elife* **11**, 1–33 (2022).
100. Kim, H. Y. *et al.* Localized Smooth Muscle Differentiation Is Essential for Epithelial Bifurcation during Branching Morphogenesis of the Mammalian Lung. *Dev Cell* **34**, 719–726 (2015).
101. Hughes, A. J. *et al.* Engineered Tissue Folding by Mechanical Compaction of the Mesenchyme. *Dev Cell* **44**, 165-178.e6 (2018).
102. Walton, K. D. *et al.* Villification in the mouse: Bmp signals control intestinal villus patterning. *Development (Cambridge)* **143**, 427–436 (2016).
103. Walton, K. D. *et al.* Hedgehog-responsive mesenchymal clusters direct patterning and emergence of intestinal villi. *Proc Natl Acad Sci U S A* **109**, 15817–15822 (2012).
104. Rao-Bhatia, A. *et al.* Hedgehog-Activated Fat4 and PCP Pathways Mediate Mesenchymal Cell Clustering and Villus Formation in Gut Development. *Dev Cell* **52**, 647-658.e6 (2020).

105. Villeneuve, C. *et al.* Mechanical forces across compartments coordinate cell shape and fate transitions to generate tissue architecture. *bioRxiv* 2022.12.12.519937 (2022).
106. Nelson, C. M. On buckling morphogenesis. *J Biomech Eng* **138**, 1–6 (2016).
107. Lemke, S. B. & Nelson, C. M. Dynamic changes in epithelial cell packing during tissue morphogenesis. *Current Biology* **31**, R1098–R1110 (2021).
108. Trushko, A. *et al.* Buckling of an Epithelium Growing under Spherical Confinement. *Dev Cell* **54**, 655-668.e6 (2020).
109. Shyer, A. E., Huycke, T. R., Lee, C., Mahadevan, L. & Tabin, C. J. Bending Gradients: How the intestinal stem cell gets its home. *Cell* **161**, 569–580 (2015).
110. Shyer, A. E. *et al.* Villification: How the gut gets its villi. *Science* **342**, 212–218 (2013).
111. Richman, D. P., Stewart, R. M., Hutchinson, J. W. & Caviness, V. S. Mechanical model of brain convolutional development. *Science* **189**, 18–21 (1975).
112. Tallinen, T., Chung, J. Y., Biggins, J. S. & Mahadevan, L. Gyrification from constrained cortical expansion. *Proc Natl Acad Sci U S A* **111**, 12667–12672 (2014).
113. Tallinen, T. *et al.* On the growth and form of cortical convolutions. *Nat Phys* **12**, 588–593 (2016).
114. Bayly, P. V., Okamoto, R. J., Xu, G., Shi, Y. & Taber, L. A. A cortical folding model incorporating stress-dependent growth explains gyral wavelengths and stress patterns in the developing brain. *Phys Biol* **10**, (2013).
115. Karzbrun, E., Kshirsagar, A., Cohen, S. R., Hanna, J. H. & Reiner, O. Human brain organoids on a chip reveal the physics of folding. *Nat Phys* **14**, 515–522 (2018).
116. Takigawa-Imamura, H., Morita, R., Iwaki, T., Tsuji, T. & Yoshikawa, K. Tooth germ invagination from cell-cell interaction: Working hypothesis on mechanical instability. *J Theor Biol* **382**, 284–291 (2015).
117. Wyatt, T. P. J. *et al.* Actomyosin controls planarity and folding of epithelia in response to compression. *Nat Mater* **19**, 109–117 (2020).
118. Reffay, M. *et al.* Interplay of RhoA and mechanical forces in collective cell migration driven by leader cells. *Nat Cell Biol* **16**, 217–223 (2014).
119. Poujade, M. *et al.* Collective migration of an epithelial monolayer in response to a model wound. *Proc Natl Acad Sci U S A* **104**, 15988–15993 (2007).
120. Omelchenko, T., Vasiliev, J. M., Gelfand, I. M., Feder, H. H. & Bonder, E. M. Rho-dependent formation of epithelial 'leader' cells during wound healing. *Proc Natl Acad Sci U S A* **100**, 10788–10793 (2003).
121. Lim, J. I., Sabouri-Ghomi, M., Machacek, M., Waterman, C. M. & Danuser, G. Protrusion and actin assembly are coupled to the organization of lamellar contractile structures. *Exp Cell Res* **316**, 2027–2041 (2010).
122. Du Roure, O. *et al.* Force mapping in epithelial cell migration. *Proc Natl Acad Sci U S A* **102**, 2390–2395 (2005).
123. Farooqui, R. & Fenteany, G. Multiple rows of cells behind an epithelial wound edge extend cryptic lamellipodia to collectively drive cell-sheet movement. *J Cell Sci* **118**, 51–63 (2005).
124. Sunyer, R. *et al.* Collective cell durotaxis emerges from long-range intercellular force transmission. *Science* **353**, 1157–1161 (2016).
125. Qin, L., Yang, D., Yi, W., Cao, H. & Xiao, G. Roles of leader and follower cells in collective cell migration. *Mol Biol Cell* **32**, 1267–1272 (2021).
126. Pallarès, M. E. *et al.* Stiffness-dependent active wetting enables optimal collective cell durotaxis. *Nat Phys* **19**, 279–289 (2022).
127. Shellard, A. & Mayor, R. Collective durotaxis along a self-generated stiffness gradient in vivo. *Nature* **600**, 690–694 (2021).

128. Shellard, A., Szabó, A., Trepat, X. & Mayor, R. Supracellular contraction at the rear of neural crest cell groups drives collective chemotaxis. *Science* **362**, 339–343 (2018).
129. Donà, E. *et al.* Directional tissue migration through a self-generated chemokine gradient. *Nature* **503**, 285–289 (2013).
130. Wurdeman, S. R. *et al.* Tumor cell-driven extracellular matrix remodeling drives haptotaxis during metastatic progression. *Cancer Discov* **6**, 516–531 (2016).
131. Versaevel, M. *et al.* Collective migration during a gap closure in a two-dimensional haptotactic model. *Sci Rep* **11**, 1–11 (2021).
132. Yamaguchi, N. *et al.* Rear traction forces drive adherent tissue migration in vivo. *Nat Cell Biol* **24**, 194–204 (2022).
133. Jain, S. *et al.* The role of single-cell mechanical behaviour and polarity in driving collective cell migration. *Nat Phys* **16**, 802–809 (2020).
134. Jain, S., Ladoux, B. & Mège, R. M. Mechanical plasticity in collective cell migration. *Curr Opin Cell Biol* **72**, 54–62 (2021).
135. Treuting, P. M., Arends, M. J. & Dintzis, S. M. Upper gastrointestinal tract. in *Comparative Anatomy and Histology* 191–211 (2018). doi:10.1016/B978-0-12-802900-8.00011-7.
136. Hewes, S. A. *et al.* In Vitro Models of the Small Intestine: Engineering Challenges and Engineering Solutions. *Tissue Eng Part B Rev* **26**, 313–326 (2020).
137. Beaulieu, J. F. *Extracellular matrix components and integrins in relationship to human intestinal epithelial cell differentiation. Progress in histochemistry and cytochemistry* vol. 31 (1997).
138. Teller, I. C. & Beaulieu, J. F. Interactions between laminin and epithelial cells in intestinal health and disease. *Expert Rev Mol Med* **3**, 1–18 (2001).
139. Mowat, A. M. & Agace, W. W. Regional specialization within the intestinal immune system. *Nat Rev Immunol* **14**, 667–685 (2014).
140. Samsa, L. A., Williamson, I. A. & Magness, S. T. Quantitative Analysis of Intestinal Stem Cell Dynamics Using Microfabricated Cell Culture Arrays Leigh. *Somatic Stem Cells: Methods and Protocols* 139–166 (2018) doi:10.1007/978-1-4939-8697-2.
141. Cheng, Z. F. & Cartwright, C. A. Rack1 maintains intestinal homeostasis by protecting the integrity of the epithelial barrier. *Am J Physiol Gastrointest Liver Physiol* **314**, G263–G274 (2018).
142. Darwich, A. S., Aslam, U., Ashcroft, D. M. & Rostami-Hodjegan, A. Meta-analysis of the turnover of intestinal epithelia in preclinical animal species and humans. *Drug Metabolism and Disposition* **42**, 2016–2022 (2014).
143. Spit, M., Koo, B. K. & Maurice, M. M. Tales from the crypt: Intestinal niche signals in tissue renewal, plasticity and cancer. *Open Biol* **8**, 180120 (2018).
144. Beumer, J. & Clevers, H. Cell fate specification and differentiation in the adult mammalian intestine. *Nat Rev Mol Cell Biol* **22**, 39–53 (2021).
145. Gehart, H. & Clevers, H. Tales from the crypt: new insights into intestinal stem cells. *Nat Rev Gastroenterol Hepatol* **16**, 19–34 (2019).
146. Leblond, C. P. & Stevens, C. E. The constant renewal of the intestinal epithelium in the albino rat. *Anat Rec* **100**, 357–377 (1948).
147. Friedman, N. B. Cellular dynamics in the intestinal mucosa: the effect of irradiation on epithelial maturation and migration. *Journal of Experimental Medicine* **81**, 553–558 (1945).
148. Bjerknes, M. & Cheng, H. The stem-cell zone of the small intestinal epithelium. I. Evidence from paneth cells in the adult mouse. *American Journal of Anatomy* **160**, 51–63 (1981).

149. Bjerknes, M. & Cheng, H. The Stem-Cell Zone of the Small Intestinal Epithelium. II. Evidence From Paneth Cells in the Newborn Mouse. *American Journal of Anatomy* **160**, 65–75 (1981).
150. Williams, I. R. & Owen, R. L. *M Cells: Specialized Antigen Sampling Cells in the Follicle-Associated Epithelium*. *Mucosal Immunology* (Elsevier, 2015). doi:10.1016/B978-0-12-415847-4.00013-6.
151. Cheng, H. & Leblond, C. Origin, differentiation and renewal of the four main epithelial cell types in the mouse small intestine. I. Columnar cell. *American Journal of Anatomy* **141**, 461–536 (1974).
152. Cheng, H. & Leblond, C. P. Origin, differentiation and renewal of the four main epithelial cell types in the mouse small intestine V. Unitarian theory of the origin of the four epithelial cell types. *American Journal of Anatomy* **141**, 521–535 (1974).
153. Barker, N. *et al.* Identification of stem cells in small intestine and colon by marker gene Lgr5. *Nature* **449**, 1003–1007 (2007).
154. van der Flier, L. G. *et al.* Transcription Factor Achaete Scute-Like 2 Controls Intestinal Stem Cell Fate. *Cell* **136**, 903–912 (2009).
155. Schuijers, J., Van Der Flier, L. G., Van Es, J. & Clevers, H. Robust cre-mediated recombination in small intestinal stem cells utilizing the Olfm4 locus. *Stem Cell Reports* **3**, 234–241 (2014).
156. van der Flier, L. G., Haegebarth, A., Stange, D. E., van de Wetering, M. & Clevers, H. OLFM4 Is a Robust Marker for Stem Cells in Human Intestine and Marks a Subset of Colorectal Cancer Cells. *Gastroenterology* **137**, 15–17 (2009).
157. Muñoz, J. *et al.* The Lgr5 intestinal stem cell signature: Robust expression of proposed quiescent ′ +4′ cell markers. *EMBO Journal* **31**, 3079–3091 (2012).
158. Guiu, J. *et al.* Tracing the origin of adult intestinal stem cells. *Nature* **570**, 107–111 (2019).
159. Snippert, H. J. *et al.* Intestinal crypt homeostasis results from neutral competition between symmetrically dividing Lgr5 stem cells. *Cell* **143**, 134–144 (2010).
160. Clevers, H. The intestinal crypt, a prototype stem cell compartment. *Cell* **154**, 274 (2013).
161. Winton, D. J. & Ponder, B. A. J. Stem-cell organization in mouse small intestine. *Proceedings of the Royal Society B: Biological Sciences* **241**, 13–18 (1990).
162. Bonis, V., Rossell, C. & Gehart, H. The Intestinal Epithelium – Fluid Fate and Rigid Structure From Crypt Bottom to Villus Tip. *Front Cell Dev Biol* **9**, 1–20 (2021).
163. Basak, O. *et al.* Mapping early fate determination in L gr5 + crypt stem cells using a novel K i67- RFP allele . *EMBO J* **33**, 2057–2068 (2014).
164. Clevers, H. C. & Bevins, C. L. Paneth cells: Maestros of the small intestinal crypts. *Annu Rev Physiol* **75**, 289–311 (2013).
165. Lueschow, S. R. & McElroy, S. J. The Paneth Cell: The Curator and Defender of the Immature Small Intestine. *Front Immunol* **11**, 1–12 (2020).
166. Cheng, H., Merzel, J. & Leblond, C. P. Renewal of Paneth cells in the small intestine of the mouse. *American Journal of Anatomy* **126**, 507–525 (1969).
167. Bjerknes, M. & Cheng, H. The stem-cell zone of the small intestinal epithelium. III. Evidence From Columnar, Enteroendocrine, and Mucous Cells in the Adult Mouse. *American Journal of Anatomy* **160**, 77–91 (1981).
168. Sato, T. *et al.* Paneth cells constitute the niche for Lgr5 stem cells in intestinal crypts. *Nature* **469**, 415–418 (2011).
169. Durand, A. *et al.* Functional intestinal stem cells after Paneth cell ablation induced by the loss of transcription factor Math1 (Atoh1). *Proc Natl Acad Sci U S A* **109**, 8965–8970 (2012).

170. Kim, T. H., Escudero, S. & Shivdasani, R. A. Intact function of Lgr5 receptor-expressing intestinal stem cells in the absence of Paneth cells. *Proc Natl Acad Sci U S A* **109**, 3932–3937 (2012).
171. Garabedian, E. M., Roberts, L. J. J., McNevin, M. S. & Gordon, J. I. Examining the role of Paneth cells in the small intestine by lineage ablation in transgenic mice. *Journal of Biological Chemistry* **272**, 23729–23740 (1997).
172. Nakamura, K. *et al.* Expression and Localization of Paneth Cells and Their α-Defensins in the Small Intestine of Adult Mouse. *Front Immunol* **11**, 1–10 (2020).
173. Feng, Y. *et al.* Sox9 induction, ectopic paneth cells, and mitotic spindle axis defects in mouse colon adenomatous epithelium arising from conditional biallelic Apc inactivation. *American Journal of Pathology* **183**, 493–503 (2013).
174. Mallow, E. B. *et al.* Human enteric defensins: Gene structure and developmental expression. *Journal of Biological Chemistry* **271**, 4038–4045 (1996).
175. Cunliffe, R. N. *et al.* Human defensin 5 is stored in precursor form in normal Paneth cells and is expressed by some villous epithelial cells and by metaplastic Paneth cells in the colon in inflammatory bowel disease. *Gut* **48**, 176–185 (2001).
176. Sasaki, N. *et al.* Reg4+ deep crypt secretory cells function as epithelial niche for Lgr5+ stem cells in colon. *Proc Natl Acad Sci U S A* **113**, E5399–E5407 (2016).
177. Batlle, E. *et al.* β-catenin and TCF mediate cell positioning in the intestinal epithelium by controlling the expression of EphB/EphrinB. *Cell* **111**, 251–263 (2002).
178. McDole, J. R. *et al.* Goblet cells deliver luminal antigen to CD103 + dendritic cells in the small intestine. *Nature* **483**, 345–349 (2012).
179. Yin, X. *et al.* Niche-independent high-purity cultures of Lgr5 + intestinal stem cells and their progeny. *Nat Methods* **11**, 106–112 (2014).
180. Xu, Y. ming *et al.* Prolyl hydroxylase 3 controls the intestine goblet cell generation through stabilizing ATOH1. *Cell Death Differ* **27**, 2131–2142 (2020).
181. Chia, L. A. & Kuo, C. J. The intestinal stem cell. *Prog Mol Biol Transl Sci* **96**, 157–173 (2010).
182. Gebert, N. *et al.* Region-Specific Proteome Changes of the Intestinal Epithelium during Aging and Dietary Restriction. *Cell Rep* **31**, 107565 (2020).
183. Malewitz, T. D. Normal Histology of the Digestive Tract of the Mouse. *Okajimas Folia Anat Jpn* **41**, 21–47 (1965).
184. Gribble, F. M. & Reimann, F. Enteroendocrine Cells: Chemosensors in the Intestinal Epithelium. *Annu Rev Physiol* **78**, 277–299 (2016).
185. Van Es, J. H. *et al.* Enteroendocrine and tuft cells support Lgr5 stem cells on Paneth cell depletion. *Proc Natl Acad Sci U S A* **116**, 26599–26605 (2019).
186. Bjerknes, M. *et al.* Origin of the brush cell lineage in the mouse intestinal epithelium. *Dev Biol* **362**, 194–218 (2012).
187. Von Moltke, J., Ji, M., Liang, H. E. & Locksley, R. M. Tuft-cell-derived IL-25 regulates an intestinal ILC2-epithelial response circuit. *Nature* **529**, 221–225 (2016).
188. Herbert, D. R. *et al.* Intestinal epithelial cell secretion of RELM-β protects against gastrointestinal worm infection. *Journal of Experimental Medicine* **206**, 2947–2957 (2009).
189. Gerbe, F. *et al.* Intestinal epithelial tuft cells initiate type 2 mucosal immunity to helminth parasites. *Nature* **529**, 226–230 (2016).
190. Casteleyn, C., Rekecki, A., Aa, A. Van Der, Simoens, P. & Broeck, W. Van Den. Original Article Surface area assessment of the murine intestinal tract as a prerequisite for oral dose translation from mouse to man. *Lab Anim* **44**, 176–183 (2010).
191. Moor, A. E. *et al.* Spatial Reconstruction of Single Enterocytes Uncovers Broad Zonation along the Intestinal Villus Axis. *Cell* **175**, 1156-1167.e15 (2018).

192. Mabbott, N. A., Donaldson, D. S., Ohno, H., Williams, I. R. & Mahajan, A. Microfold (M) cells: Important immunosurveillance posts in the intestinal epithelium. *Mucosal Immunol* **6**, 666–677 (2013).
193. Knoop, K. A. *et al.* RANKL Is Necessary and Sufficient to Initiate Development of Antigen-Sampling M Cells in the Intestinal Epithelium. *The Journal of Immunology* **183**, 5738–5747 (2009).
194. Sato, T. *et al.* Single Lgr5 stem cells build crypt-villus structures in vitro without a mesenchymal niche. *Nature* **459**, 262–265 (2009).
195. Serra, D. *et al.* Self-organization and symmetry breaking in intestinal organoid development. *Nature* **569**, 66–72 (2019).
196. Spence, J. R. *et al.* Directed differentiation of human pluripotent stem cells into intestinal tissue in vitro. *Nature* **470**, 105–110 (2011).
197. Takahashi, Y. *et al.* A Refined Culture System for Human Induced Pluripotent Stem Cell-Derived Intestinal Epithelial Organoids. *Stem Cell Reports* **10**, 314–328 (2018).
198. Altay, G. *et al.* Self-organized intestinal epithelial monolayers in crypt and villus-like domains show effective barrier function. *Sci Rep* **9**, 1–14 (2019).
199. Thorne, C. A. *et al.* Enteroid Monolayers Reveal an Autonomous WNT and BMP Circuit Controlling Intestinal Epithelial Growth and Organization. *Dev Cell* **44**, 624-633.e4 (2018).
200. Liu, Y., Qi, Z., Li, X., Du, Y. & Chen, Y.-G. Monolayer culture of intestinal epithelium sustains Lgr5+ intestinal stem cells. *Cell Discov* **4**, 4–6 (2018).
201. Kim, R. *et al.* Formation of arrays of planar, murine, intestinal crypts possessing a stem/proliferative cell compartment and differentiated cell zone. *Lab Chip* **18**, 2202–2213 (2018).
202. Breau, K. A. *et al.* Efficient transgenesis and homology-directed gene targeting in monolayers of primary human small intestinal and colonic epithelial stem cells. *Stem Cell Reports* **17**, 1493–1506 (2022).
203. Hinman, S. S., Wang, Y., Kim, R. & Allbritton, N. L. In vitro generation of self-renewing human intestinal epithelia over planar and shaped collagen hydrogels. *Nat Protoc* **16**, 352–382 (2021).
204. Larrañaga Carricajo, E. Effects of substrate-derived cues in driving the selforganization of organoid-derived intestinal epithelia. (2021). doi:http://hdl.handle.net/10803/672277.
205. Wang, Y. *et al.* A microengineered collagen scaffold for generating a polarized crypt-villus architecture of human small intestinal epithelium. *Biomaterials* **128**, 44–55 (2017).
206. Nikolaev, M. *et al.* Homeostatic mini-intestines through scaffold-guided organoid morphogenesis. *Nature* **585**, 574–578 (2020).
207. Verhulsel, M. *et al.* Developing an advanced gut on chip model enabling the study of epithelial cell/fibroblast interactions. *Lab Chip* **21**, 365–377 (2021).
208. Gjorevski, N. *et al.* Tissue geometry drives deterministic organoid patterning. *Science* **375**, eaaw9021 (2022).
209. Altay, G. *et al.* Modeling Biochemical Gradients In Vitro to Control Cell Compartmentalization in a Microengineered 3D Model of the Intestinal Epithelium. *Adv Healthc Mater* **11**, 1–15 (2022).
210. Puschhof, J. *et al.* Intestinal organoid cocultures with microbes. *Nat Protoc* **16**, 4633–4649 (2021).
211. Pleguezuelos-Manzano, C. *et al.* Mutational signature in colorectal cancer caused by genotoxic pks + E. coli. *Nature* **580**, 269–273 (2020).

212. Kurpios, N. A. *et al.* The direction of gut looping is established by changes in the extracellular matrix and in cell: Cell adhesion. *Proc Natl Acad Sci U S A* **105**, 8499–8506 (2008).
213. Davis, N. M. *et al.* The Chirality of Gut Rotation Derives from Left-Right Asymmetric Changes in the Architecture of the Dorsal Mesentery. *Dev Cell* **15**, 134–145 (2008).
214. Savin, T. *et al.* On the growth and form of the gut. *Nature* **476**, 57–63 (2011).
215. Nerurkar, N. L., Mahadevan, L. & Tabin, C. J. BMP signaling controls buckling forces to modulate looping morphogenesis of the gut. *Proc Natl Acad Sci U S A* **114**, 2277–2282 (2017).
216. Coulombre, A. J. & Coulombre, J. L. Intestinal Development. *Development* **6**, 403–411 (1958).
217. Hilton, W. A. The morphology and development of intestinal folds and villi in vertebrates. *American Journal of Anatomy* **1**, 459–505 (1902).
218. Sbarbati, R. Morphogenesis of the intestinal villi of the mouse embryo: chance and spatial necessity. *J Anat* **135**, 477–499 (1982).
219. Walton, K. D., Mishkind, D., Riddle, M. R., Tabin, C. J. & Gumucio, D. L. Blueprint for an intestinal villus: Species-specific assembly required. *Wiley Interdiscip Rev Dev Biol* **7**, 1–19 (2018).
220. Freddo, A. M. *et al.* Coordination of signaling and tissue mechanics during morphogenesis of murine intestinal villi: A role for mitotic cell rounding. *Integrative Biology (United Kingdom)* **8**, 918–928 (2016).
221. Houtekamer, R. M., van der Net, M. C., Maurice, M. M. & Gloerich, M. Mechanical forces directing intestinal form and function. *Current Biology* **32**, R791–R805 (2022).
222. Sugimoto, S. *et al.* An organoid-based organ-repurposing approach to treat short bowel syndrome. *Nature* **592**, 99–104 (2021).
223. Kim, H. J. & Ingber, D. E. Gut-on-a-Chip microenvironment induces human intestinal cells to undergo villus differentiation. *Integrative Biology (United Kingdom)* **5**, 1130–1140 (2013).
224. Dehmer, J. J. *et al.* Expansion of intestinal epithelial stem cells during murine development. *PLoS One* **6**, 1–9 (2011).
225. Trier, J. S. & Moxey, P. C. Morphogenesis of the small intestine during fetal development. *Ciba Found Symp* **70**, 3–29 (1979).
226. Sumigray, K. D., Terwilliger, M. & Lechler, T. Morphogenesis and Compartmentalization of the Intestinal Crypt. *Dev Cell* **45**, 183-197.e5 (2018).
227. Hartl, L., Huelsz-Prince, G., van Zon, J. & Tans, S. J. Apical constriction is necessary for crypt formation in small intestinal organoids. *Dev Biol* **450**, 76–81 (2019).
228. Kania, A. & Klein, R. Mechanisms of ephrin-Eph signalling in development, physiology and disease. *Nat Rev Mol Cell Biol* **17**, 240–256 (2016).
229. Liang, L. Y., Patel, O., Janes, P. W., Murphy, J. M. & Lucet, I. S. Eph receptor signalling: from catalytic to non-catalytic functions. *Oncogene* **38**, 6567–6584 (2019).
230. Franco, M. & Carmena, A. Eph signaling in mitotic spindle orientation: what´s your angle here? *Cell Cycle* **18**, 2590–2597 (2019).
231. Islam, S., Loizides, A. M., Fialkovich, J. J., Grand, R. J. & Montgomery, R. K. Developmental expression of Eph and ephrin family genes in mammalian small intestine. *Dig Dis Sci* **55**, 2478–2488 (2010).
232. Ishii, M., Nakajima, T. & Ogawa, K. Complementary expression of EphB receptors and ephrin-B ligand in the pyloric and duodenal epithelium of adult mice. *Histochem Cell Biol* **136**, 345–356 (2011).
233. Cortina, C. *et al.* EphB-ephrin-B interactions suppress colorectal cancer progression by compartmentalizing tumor cells. *Nat Genet* **39**, 1376–1383 (2007).

234. Holmberg, J. *et al.* EphB Receptors Coordinate Migration and Proliferation in the Intestinal Stem Cell Niche. *Cell* **125**, 1151–1163 (2006).
235. Genander, M. *et al.* Dissociation of EphB2 Signaling Pathways Mediating Progenitor Cell Proliferation and Tumor Suppression. *Cell* **139**, 679–692 (2009).
236. Kosinski, C. *et al.* Gene expression patterns of human colon tops and basal crypts and BMP antagonists as intestinal stem cell niche factors. *Proc Natl Acad Sci U S A* **104**, 15418–15423 (2007).
237. Solanas, G., Cortina, C., Sevillano, M. & Batlle, E. Cleavage of E-cadherin by ADAM10 mediates epithelial cell sorting downstream of EphB signalling. *Nat Cell Biol* **13**, 1100–1107 (2011).
238. Cayuso, J., Xu, Q., Addison, M. & Wilkinson, D. G. Actomyosin regulation by eph receptor signaling couples boundary cell formation to border sharpness. *Elife* **8**, 1–23 (2019).
239. Duran, C. C. Role of EphB receptors in intestinal epithelial cell positioning and colorectal cancer progression. (2009). doi:http://hdl.handle.net/10803/35692.
240. O'Neill, A. K. *et al.* Unidirectional Eph/ephrin signaling creates a cortical actomyosin differential to drive cell segregation. *Journal of Cell Biology* **215**, 217–229 (2016).
241. Calzolari, S., Terriente, J. & Pujades, C. Cell segregation in the vertebrate hindbrain relies on actomyosin cables located at the interhombomeric boundaries. *EMBO Journal* **33**, 686–701 (2014).
242. Javaherian, S. *et al.* Modulation of cellular polarization and migration by ephrin/Eph signal-mediated boundary formation. *Integrative Biology (United Kingdom)* **9**, 934–946 (2017).
243. Jørgensen, C. *et al.* Cell-specific information processing in segregating populations of Eph receptor ephrin-expressing cells. *Science* **326**, 1502–1509 (2009).
244. Li, Y. *et al.* Volumetric Compression Induces Intracellular Crowding to Control Intestinal Organoid Growth via Wnt/β-Catenin Signaling. *Cell Stem Cell* **28**, 63-78.e7 (2021).
245. Fernandez-Sanchez, M. E. *et al.* Mechanical induction of the tumorigenic b-catenin pathway by tumour growth pressure. *Nature* **523**, 92–95 (2015).
246. Gordon, W. R. *et al.* Mechanical Allostery: Evidence for a Force Requirement in the Proteolytic Activation of Notch. *Dev Cell* **33**, 729–736 (2015).
247. Gjorevski, N. *et al.* Designer matrices for intestinal stem cell and organoid culture. *Nature* **539**, 560–564 (2016).
248. Yui, S. *et al.* YAP/TAZ-Dependent Reprogramming of Colonic Epithelium Links ECM Remodeling to Tissue Regeneration. *Cell Stem Cell* **22**, 35-49.e7 (2018).
249. Gregorieff, A., Liu, Y., Inanlou, M. R., Khomchuk, Y. & Wrana, J. L. Yap-dependent reprogramming of Lgr5+ stem cells drives intestinal regeneration and cancer. *Nature* **526**, 715–718 (2015).
250. Guillermin, O. *et al.* Wnt and Src signals converge on YAP-TEAD to drive intestinal regeneration. *EMBO J* **40**, e105770 (2021).
251. Barry, E. R. *et al.* Restriction of intestinal stem cell expansion and the regenerative response by YAP. *Nature* **493**, 106–110 (2013).
252. Imajo, M., Ebisuya, M. & Nishida, E. Dual role of YAP and TAZ in renewal of the intestinal epithelium. *Nat Cell Biol* **17**, 7–19 (2015).
253. Cheung, P. *et al.* Regenerative Reprogramming of the Intestinal Stem Cell State via Hippo Signaling Suppresses Metastatic Colorectal Cancer. *Cell Stem Cell* **27**, 590-604.e9 (2020).
254. Li, Q. *et al.* Lats1/2 Sustain Intestinal Stem Cells and Wnt Activation through TEAD-Dependent and Independent Transcription. *Cell Stem Cell* **26**, 675-692.e8 (2020).

255. Parker, A. *et al.* Cell proliferation within small intestinal crypts is the principal driving force for cell migration on villi. *FASEB Journal* **31**, 636–649 (2017).
256. Partridge, B. T. & Simpson, L. O. Duodenal epithelial cell migration and loss in NZB mice. *Micron* **11**, 63–72 (1980).
257. Kaur, P. & Potten, C. S. Cell Migration Velocities In the Crypts of the Small Intestine After Cytotoxic Insult Are Not Dependent On Mitotic Activity. *Cell Prolif* **19**, 601–610 (1986).
258. Devik, F. Intestinal cell kinetics in irradiated mice: A quantitative investigation of the acute reaction to whole body roentgen irradiation. *Acta Oncol (Madr)* **10**, 129–149 (1971).
259. Potten, C. S., Chwalinski, S., Swindell, R. & Palmer, M. The spatial organization of the hierarchical proliferative cells. *Cell Tissue Kinet* **15**, 351–370 (1982).
260. Altmann, G. G. Changes in the mucosa of the small intestine following methotrexate administration or abdominal X-irradiation. *American Journal of Anatomy* **140**, 263–279 (1974).
261. Krndija, D. *et al.* Active cell migration is critical for steady-state epithelial turnover in the gut. *Science* **365**, 705–710 (2019).
262. Kaur, P. & Potten, C. S. Effects of puromycin, cycloheximide and noradrenaline on cell migration within the crypts and on the villi of the small intestine. A model to explain cell movement in both regions. *Cell Tissue Kinet* **19**, 611–625 (1986).
263. Potten, C. S. & Allen, T. D. Ultrastructure of cell loss in intestinal mucosa. *Journal of Ultrasructure Research* **60**, 272–277 (1977).
264. Schmidt, G. H., Wilkinson, M. M. & Ponder, B. A. J. Cell migration pathway in the intestinal epithelium: An in situ marker system using mouse aggregation chimeras. *Cell* **40**, 425–429 (1985).
265. Madara, J. L. Maintenance of the macromolecular barrier at cell extrusion sites in intestinal epithelium: Physiological rearrangement of tight junctions. *J Membr Biol* **116**, 177–184 (1990).
266. Guan, Y. *et al.* Redistribution of the tight junction protein ZO-1 during physiological shedding of mouse intestinal epithelial cells. *Am J Physiol Cell Physiol* **300**, 1404–1414 (2011).
267. Marshall, T. W., Lloyd, I. E., Marie, J. & Näthke, I. The tumor suppressor adenomatous polyposis coli controls the direction in which a cell extrudes from an epithelium. *Mol Biol Cell* **22**, 3962–3970 (2011).
268. Gu, Y. *et al.* Defective apical extrusion signaling contributes to aggressive tumor hallmarks. *Elife* **4**, e04069 (2015).
269. Ritchie, J. M. *et al.* Inflammation and disintegration of intestinal villi in an experimental model for vibrio parahaemolyticus-induced diarrhea. *PLoS Pathog* **8**, e1002593 (2012).
270. Liu, J. J. *et al.* Mind the gaps: Confocal endomicroscopy showed increased density of small bowel epithelial gaps in inflammatory bowel disease. *J Clin Gastroenterol* **45**, 240–245 (2011).
271. Ngo, P. A. & Neurath, M. F. Impact of Epithelial Cell Shedding on Intestinal Homeostasis. *Int J Mol Sci* **23**, 4160 (2022).
272. Rosenblatt, J., Raff, M. C. & Cramer, L. P. An epithelial cell destined for apoptosis signals its neighbors to extrude it by an actin- and myosin-dependent mechanism. *Current Biology* **11**, 1847–1857 (2001).
273. Gu, Y., Forostyan, T., Sabbadini, R. & Rosenblatt, J. Epithelial cell extrusion requires the sphingosine-1- phosphate receptor 2 pathway. *J Cell Biol* **193**, 667–676 (2011).

274. Marinari, E. *et al.* Live-cell delamination counterbalances epithelial growth to limit tissue overcrowding. *Nature* **484**, 542–545 (2012).
275. Doostmohammadi, A. & Ladoux, B. Physics of liquid crystals in cell biology. *Trends Cell Biol* **32**, 140–150 (2022).
276. Saw, T. B. *et al.* Topological defects in epithelia govern cell death and extrusion. *Nature* **544**, 212–216 (2017).
277. Muzumdar, M. D., Tasic, B., Miyamichi, K., Li, N. & Luo, L. A global double-fluorescent cre reporter mouse. *Genesis (United States)* **45**, 593–605 (2007).
278. Riedl, J. *et al.* Lifeact mice for studying F-actin dynamics. *Nat Methods* **7**, 168–169 (2010).
279. Zhang, Y. *et al.* Mouse models of MYH9-related disease: Mutations in nonmuscle myosin II-A. *Blood* **119**, 238–250 (2012).
280. Henkemeyer, M. *et al.* Nuk controls pathfinding of commissural axons in the mammalian central nervous system. *Cell* **86**, 35–46 (1996).
281. Orioli, D., Henkemeyer, M., Lemke, G., Klein, R. & Pawson, T. Sek4 and Nuk receptors cooperate in guidance of commissural axons and in palate formation. *EMBO Journal* **15**, 6035–6049 (1996).
282. Pérez-González, C. *et al.* Active wetting of epithelial tissues. *Nat Phys* **15**, 79–88 (2019).
283. O'Rourke, K. P., Dow, L. E. & Lowe, S. W. Immunofluorescent Staining of Mouse Intestinal Stem Cells. *Bio Protoc* **6**, e1732 (2016).
284. Edelstein, A. D. *et al.* Advanced methods of microscope control using μManager software. *J Biol Methods* **1**, e10 (2014).
285. del Álamo, J. C. *et al.* Three-Dimensional Quantification of Cellular Traction Forces and Mechanosensing of Thin Substrata by Fourier Traction Force Microscopy. *PLoS One* **8**, e69850 (2013).
286. Schindelin, J. *et al.* Fiji: An open-source platform for biological-image analysis. *Nat Methods* **9**, 676–682 (2012).
287. de Reuille, P. B. *et al.* MorphoGraphX: A platform for quantifying morphogenesis in 4D. *Elife* **4**, e05864 (2015).
288. Pachitariu, M. & Stringer, C. Cellpose 2.0: how to train your own model. *Nat Methods* **19**, 1634–1641 (2022).
289. Stringer, C., Wang, T., Michaelos, M. & Pachitariu, M. Cellpose: a generalist algorithm for cellular segmentation. *Nat Methods* **18**, 100–106 (2021).
290. Clark, P. J. & Evans, F. C. Distance to Nearest Neighbor as a Measure of Spatial Relationships in Populations. *Ecology* **35**, 445–453 (1954).
291. Baddeley, A., Rubak, E. & Turner, R. *Spatial Point Patterns: Methodology and Applications with R*. (Chapman and Hall/CRC Press, 2015).
292. R Core Team. R: A Language and Environment for Statistical Computing. *R: A language and environment for statistical computing. R Foundation for Statistical Computing, Vienna, Austria.* https://www.r-project.org/ (2022).
293. Azkanaz, M. *et al.* Retrograde movements determine effective stem cell numbers in the intestine. *Nature* **607**, 548–554 (2022).
294. Ritsma, L. *et al.* Intestinal crypt homeostasis revealed at single-stem-cell level by in vivo live imaging. *Nature* **507**, 362–365 (2014).
295. Hannezo, E., Prost, J. & Joanny, J. F. Theory of epithelial sheet morphology in three dimensions. *Proc Natl Acad Sci U S A* **111**, 27–32 (2014).
296. Merkel, M. & Manning, M. L. A geometrically controlled rigidity transition in a model for confluent 3D tissues. *New J Phys* **20**, 022002 (2018).

297. Alt, S., Ganguly, P. & Salbreux, G. Vertex models: From cell mechanics to tissue morphogenesis. *Philosophical Transactions of the Royal Society B: Biological Sciences* **372**, 20150520 (2017).
298. Rodríguez-Colman, M. J. *et al.* Interplay between metabolic identities in the intestinal crypt supports stem cell function. *Nature* **543**, 424–427 (2017).
299. Van Lidth de Jeude, J. F., Vermeulen, J. L. M., Montenegro-Miranda, P. S., Van den Brink, G. R. & Heijmans, J. A Protocol for Lentiviral Transduction and Downstream Analysis of Intestinal Organoids. *Journal of Visualized Experiments* **98**, e52531 (2015).
300. Rupprecht, J. F. *et al.* Geometric constraints alter cell arrangements within curved epithelial tissues. *Mol Biol Cell* **28**, 3582–3594 (2017).
301. Cayuso, J., Xu, Q. & Wilkinson, D. G. Mechanisms of boundary formation by Eph receptor and ephrin signaling. *Dev Biol* **401**, 122–131 (2015).
302. Xu, Q., Mellitzer, G., Robinson, V. & Wilkinson, D. G. In vivo cell sorting in complementary segmental domains mediated by Eph receptors and ephrins. *Nature* **399**, 267–271 (1999).
303. Merlos-Suárez, A. *et al.* The intestinal stem cell signature identifies colorectal cancer stem cells and predicts disease relapse. *Cell Stem Cell* **8**, 511–524 (2011).
304. Theveneau, E. *et al.* Chase-and-run between adjacent cell populations promotes directional collective migration. *Nat Cell Biol* **15**, 763–772 (2013).
305. Broguiere, N. *et al.* Growth of Epithelial Organoids in a Defined Hydrogel. *Advanced Materials* **30**, 1801621 (2018).
306. Xi, W. *et al.* Modulation of designer biomimetic matrices for optimized differentiated intestinal epithelial cultures. *Biomaterials* **282**, 121380 (2022).
307. Yang, Q. *et al.* Cell fate coordinates mechano-osmotic forces in intestinal crypt formation. *Nat Cell Biol* **23**, 733–744 (2021).
308. Pentinmikko, N. *et al.* Cellular shape reinforces niche to stem cell signaling in the small intestine. *Sci Adv* **8**, eabm1847 (2022).
309. He, S. *et al.* Stiffness Restricts the Stemness of the Intestinal Stem Cells and Skews Their Differentiation Towards Goblet Cells. *Gastroenterology* **146**, 1137–1151 (2023).
310. Schoenborn, A. A. *et al.* The enteric microbiota regulates jejunal Paneth cell number and function without impacting intestinal stem cells. *Gut Microbes* **10**, 45–58 (2019).
311. Farin, H. F. *et al.* Visualization of a short-range Wnt gradient in the intestinal stem-cell niche. *Nature* **530**, 340–343 (2016).
312. Leighton, J., Brada, Z., Estes, L. W. & Justh, G. Secretory activity and oncogenicity of a cell line (MDCK) derived from canine kidney. *Science* **163**, 472–473 (1969).
313. Dekkers, J. F. *et al.* A functional CFTR assay using primary cystic fibrosis intestinal organoids. *Nat Med* **19**, 939–945 (2013).
314. Engevik, A. C. & Engevik, M. A. Exploring the impact of intestinal ion transport on the gut microbiota. *Comput Struct Biotechnol J* **19**, 134–144 (2021).
315. Komuro, T. Fenestrations of the basal lamina of intestinal villi of the rat. *Cell Tissue Res* **239**, 183–188 (1985).
316. Bohórquez, D. V. & Liddle, R. A. Axon-like basal processes in enteroendocrine cells: characteristics and potential targets. *Clin Transl Sci* **4**, 387–391 (2011).
317. Toner, P. G. & Ferguson, A. Intraepithelial cells in the human intestinal mucosa. *Journal of Ultrasructure Research* **34**, 329–344 (1971).
318. Taylor, H. B. *et al.* Cell segregation and border sharpening by Eph receptor-ephrin-mediated heterotypic repulsion. *J R Soc Interface* **14**, 20170338 (2017).
319. Riedl, J. A. *et al.* Down-regulation of Rap1 activity is involved in ephrinB1-induced cell contraction. *Biochemical Journal* **389**, 465–469 (2005).

320. Furukawa, K. *et al.* Smad3 contributes to positioning of proliferating cells in colonic crypts by inducing EphB receptor protein expression. *Biochem Biophys Res Commun* **405**, 521–526 (2011).
321. McConnell, B. B. *et al.* Krppel-like factor 5 is important for maintenance of crypt architecture and barrier function in mouse intestine. *Gastroenterology* **141**, 1302–1313 (2011).
322. Pond, K. W. *et al.* Live-cell imaging in human colonic monolayers reveals ERK waves limit the stem cell compartment to maintain epithelial homeostasis. *Elife* **11**, e78837 (2022).
323. Kabiri, Z. *et al.* Wnt signaling suppresses MAPK-driven proliferation of intestinal stem cells. *Journal of Clinical Investigation* **128**, 3806–3812 (2018).
324. Wei, G. *et al.* Erk and MAPK signaling is essential for intestinal development through Wnt pathway modulation. *Development (Cambridge)* **147**, dev185678 (2020).
325. Park, H. W. *et al.* Alternative Wnt Signaling Activates YAP/TAZ. *Cell* **162**, 780–794 (2015).
326. Franco, M. & Carmena, A. Eph signaling controls mitotic spindle orientation and cell proliferation in neuroepithelial cells. *Journal of Cell Biology* **218**, 1200–1217 (2019).
327. Quyn, A. J. *et al.* Spindle Orientation Bias in Gut Epithelial Stem Cell Compartments Is Lost in Precancerous Tissue. *Cell Stem Cell* **6**, 175–181 (2010).
328. Bellis, J. *et al.* The tumor suppressor Apc controls planar cell polarities central to gut homeostasis. *Journal of Cell Biology* **198**, 331–341 (2012).
329. Fernández-majada, V., Comelles, J., Acevedo, V. & Lázaro, A. A. Subepithelial Myofibroblasts Are Critical Regulators of Intestinal Epithelial Restoration. *bioRxiv* (2021) doi:https://doi.org/10.1101/2021.05.28.446131.
330. Kocgozlu, L. *et al.* Epithelial Cell Packing Induces Distinct Modes of Cell Extrusions. *Current Biology* **26**, 2942–2950 (2016).
331. Ma, L. & Klug, W. S. Viscous regularization and r-adaptive remeshing for finite element analysis of lipid membrane mechanics. *J Comput Phys* **227**, 5816–5835 (2008).
332. Belytschko, T., Liu, W. K., Moran, B. & Elkhodary, K. *Nonlinear Finite Elements for Continua and Structures*. (Wiley, 2014).
333. Chugh, P. *et al.* Actin cortex architecture regulates cell surface tension. *Nat Cell Biol* **19**, 689–697 (2017).